The Development of an Optofluidic Biosensing Platform for Multifunctional Biomolecular Analysis

by

Xiaotian Tan

A dissertation submitted in partial fulfillment
of the requirements for the degree of
Doctor of Philosophy
(Biomedical Engineering)
in the University of Michigan
2020

Doctoral Committee:

Professor Xudong Fan, Chair
Professor Mark L. Day
Professor Sunitha Nagrath
Professor Ariella Shikanov
Professor Nils G. Walter

Xiaotian Tan

tanxt@umich.edu

ORCID iD: 0000-0001-5529-8092

Dedication

To my strong, encouraging and gentle mother, Guo Ying (郭英). You are the most important person and the strongest backbone in my life. Without your support, I wouldn't even survive this Ph.D. study.

To my brave, humorous, warm and talented father, Tan Fubin (谭福彬), who passed away in 2012. You are my reason for coming into the field of biomedical engineering, so sad that you can't see my accomplishment today. I will try my best to become a qualified "next life" of you.

Acknowledgements

First and foremost, I would like to express the deepest appreciation to my research advisor and committee chair, Professor Xudong Fan, who is a knowledgeable scientist for the greater biosensing field and a beloved mentor for myself. His wisdom, inspirational guidance, persistent support and super positive work attitude continuously motivated me to journey through the tough Ph.D. study.

I would also like to thank my dear committee members, Professor Ariella Shikanov, Professor Mark Day, Professor Sunitha Nagrath, and Professor Nils Walter. I really learned a lot of specialized knowledge through collaborations and discussions with them. Their resources, encouragement and suggestions have helped me a lot, not only in completing my research projects, but also in my academic career.

Finally, as an international student who has no family member in the United States, I would like to give special thanks to my Fanlab comrades (especially Dr. Yu-Cheng Chen, Dr. Qiushu Chen, Dr. Hongbo Zhu, Dr. Yuan Gong, Dr. Maung Kyaw Khiang Oo, Dr. Girish Kulkarni, Dr. Menglian Zhou, Dr. Xiaoqin Wu, Dr. Wenzhe Zang, Dr. Jinyan She, Dr. Wen Xue, Dr. Song Zhu, Mr. Xuzhou Li, Mr. Maxwell Li, Mr. Shiyu Wang and Ms. Wenyi Liu) and personal friends (especially Mr. Sicong Wang and Mr. Harald Yuanhui Liu). They are my families and my torches even during my darkest time.

I would also like to acknowledge University of Michigan (both my department and the Rackham graduate school) and National Science Foundation for providing financial support during my graduate studies.

Table of Contents

List of Figures

Abstract

Biosensors are devices or systems that can be used to detect, quantify, and analyze targets with biological activities and functions. As one of the largest subsets of biosensors, biomolecular sensors are specifically developed and programmed to detect, quantify and analyze biomolecules in liquid samples.

Wide-ranging applications have made immunoassays increasingly popular for biomolecular detection and quantification. Among these, enzyme-linked immunosorbent assays (ELISAs) are of particular interest due to high specificity and reproducibility. To some extent, ELISAs have been regarded as a "gold standard" for quantifying analytes (especially protein analytes) in both clinical diagnostics and fundamental biological research. However, traditional (96-well plate-based) ELISA still suffers from several notable drawbacks, such as long assay time (4–6 hours), lengthy procedures, and large sample/reagent consumption (~100 μL). These inherent disadvantages still significantly limit the applicability of traditional ELISA in areas such as rapid clinical diagnosis of acute diseases (e.g., viral pneumonia, acute organ rejection), and biological research that requires accurate measurements with precious or low abundance samples (e.g., tail vein serum from a mouse). Thus, a bimolecular sensing technology that has a high sensitivity, short assay time, and small sample/reagent consumption is still strongly desired.

In this dissertation, we introduce the development of a multifunctional and automated optofluidic immunoassay platform that can resolve the aforementioned problems. In contrast to conventional plate-based ELISA, our optofluidic ELISA platform utilizes mass-producible

polystyrene microfluidic channels with a high surface-to-volume ratio as the immunoassay reactors, which greatly shortens the total assay time. We also developed a low-noise signal amplification protocol and an optical signal quantification system that was optimized for the optofluidic ELISA platform.

Our optofluidic ELISA platform provides several attractive features such as small sample/reagent consumption (<8 μL), short total assay time (30-45 min), high sensitivity (~1 pg/mL for most markers), and broad dynamic ranges (3-4 orders of magnitude). Using these features, we successfully quantified mouse FSH (follicle stimulating hormone) concentration from a single drop of tail vein serum. We also successfully monitored bladder cancer progression in orthotopic xenografted mice with only <50 μL of mouse urine. More excitingly, we achieved highly sensitive exosome quantification and multiplexed immuno-profiling with <40 ng/mL of total input protein (per assay). These remarkable milestones could not be achieved with conventional plate-based ELISA but were enabled by our unique optofluidic ELISA.

As an emerging member of the biomolecular sensor family, our optofluidic ELISA platform provides a high-performance and cost-effective tool for a plethora of applications, including endocrinology, oncology, cellular biology, and even forensic science research. In the future, this technology platform can also be adopted for clinical applications such as personalized cancer diagnosis/prognosis and rapid point-of-care diagnostics for infectious diseases.

Chapter 1

Introduction

1.1. Introductory remark:

Biosensors are devices or systems that can be used to detect, quantify, and characterize analytes with biological activities and functions. Accurately and rapidly monitoring the functions and responses of biological systems has always been a major topic in the development of biosensing techniques. To achieve this goal, generations of scientists and engineers had dedicated their efforts[1].

In this dissertation, we will introduce the development of a new member in the biomolecular sensor family: an immunoassay-based optofluidic biosensing platform for multifunctional biomolecular analysis.

We will briefly introduce the definition and chemical mechanisms of biomolecular sensors, especially immunosensors in chapter one. In chapter two, we will introduce different types of traditional and new immunoassay systems. We will also introduce several general concepts for designing a solid-phase immunosensor. Chapters three and four introduce two preliminary prototypes of optofluidic biosensors, including a glass capillary-based optofluidic ELISA system (chapter 3)[2] and an on-chip optofluidic ELISA laser system (chapter 4)[3]. Chapter 5,6 and 7 are applications based on the mature and automated optofluidic biosensing system. The applications

include the quantification of the follicle stimulating hormone (FSH) from the mouse tail vein serum (chapter 5)[2]; quantitative bladder cancer surveillance of orthotopic xenografted mice based on urinary cancer marker measurements (chapter 6)[4] and the quantification and immunoprofiling of cancer cell-derived exosomes (chapter 7). The last chapter (chapter 8) will include a summary of the entire dissertation and some future perspectives in the development of the next generation immunosensors.

1.2. Biomolecular Sensors:

As one of the largest subsets of all biosensors by application, biomolecular sensors are developed and are defined as the sensors that can be used to specifically detecting and analyzing analytes majorly in liquid samples (the technologies that designed to detect biomolecules in cells and tissues are excluded in this context)[5]. They play unique roles in multiple fields such as medical diagnosis, molecular biology researches, and even criminal investigations. A brief illustration of the biosensor family can be found in Fig. 1.1.

Due to the limitation in information density, qualitative assays (e.g., test strips) that provide Yes/No results can only be used in simple applications such as rapid pregnancy test. In contrast, quantitative assays can provide information not only about the existence of the target but also the abundance of the target molecule in the sample. Thus, it can be used in more rigorous applications.

The enzymatic electrochemical biosensor is a subset of quantitative biomolecular sensors with a very long history (more than 50 years)[6]. It was widely used in blood glucose measurements. However, the application universality of this type of sensor was greatly limited by its own sensing principle – it can only be used to detect targets that can be oxidized or reduced by redox enzymes (e.g., glucose can be oxidized by glucose oxidase)[6].

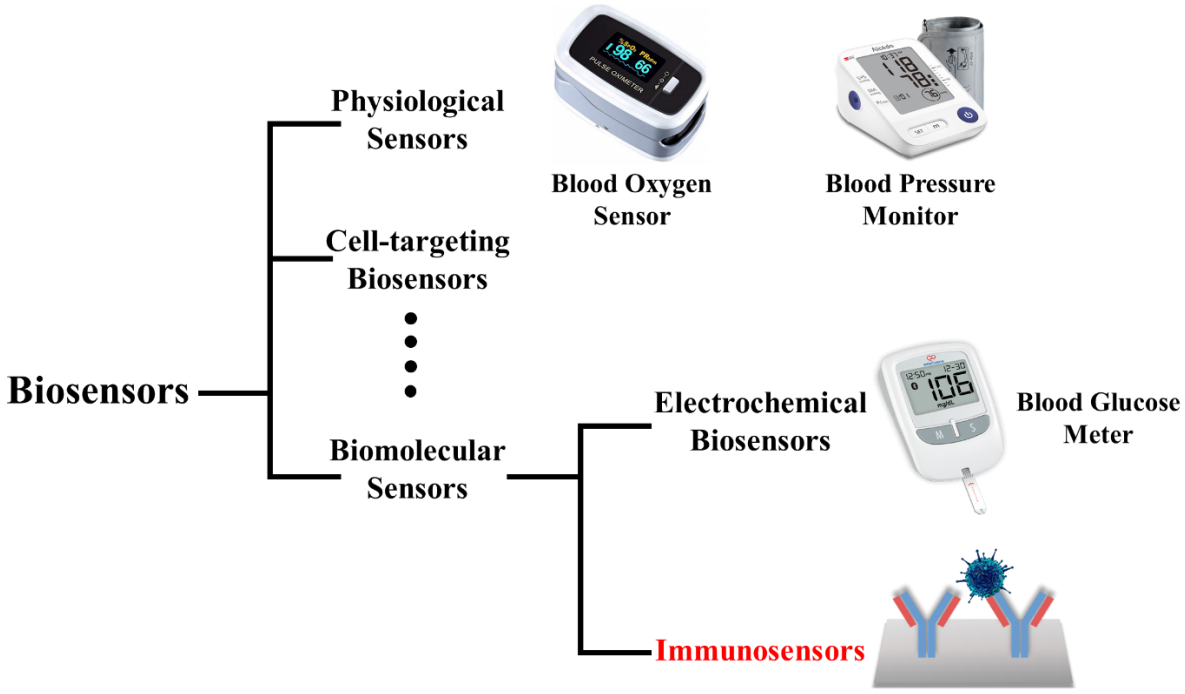

Figure 1.1. A dendrogram for different types of biosensors. Immunosensor is a branch of the biomolecular sensors

In contrast, there is another remarkable subset of the biomolecular sensor that does not rely on the specific chemical reactivity of analytes, which is called the immunosensor. The most commonly used molecule-recognition probes in immunosensors are antibodies (there are also other types of immuno-sensing probes such as DNA/RNA aptamers)[7-8]. The root "immuno" was developed because the antibodies are generally produced through an adaptive immune response[9]. In immunosensors, the recognition of biomolecular analytes is achieved through shape-dependent affinity binding[10]. In detail, the antibody's paratope can interacts with the antigen's epitope by spatial complementarity and the binding can be maintained by molecular forces such as electrostatic forces, hydrogen bonds or hydrophobic interactions (this mechanism was previously described as the lock and key model)[10]. Since the recognition mechanism of antibodies is solely dependent on the spatial structure of the analytes, it can be used to detect a broad range of targets,

including small physiological molecules (e.g., histamine)[11], special nucleic acids (e.g., DNA/RNA complex)[12] and proteins[2]. The size of the potential detection targets (antigens) distributed widely in a range between 0.1-300 kDa.

The tests that utilize immunosensors to quantify analytes in liquid samples are call immunoassays. Although an antibody can bind with its desired antigen, it does not have the ability to transduce this binding event into a measurable signal. To solve this problem, scientists have developed several generations of detection mechanisms and corresponding hardware.

1.3. Earlier generations of immunoassays

1.3.1. Radioimmunoassay (RIA)

The first generation of immunoassays that was widely used in public was the radioimmunoassay (RIA)[13-14]. As Fig. 1.2 shows, RIA is a bead-based competitive immunoassay (solid-phase immunoassay) that can be performed in a relatively large reactor (test tubes or cuvettes)[15]. In this type of assay, the antibodies are pre-labeled with a radioactive marker as a signal transducer (I-125 in most cases)[16], and the antibody-antigen complex can be eventually pulled-down with secondary antibody-coated beads[17]. The quantity of the analyte can be analyzed by measuring the intensity of radioactivity in the pellet. However, this technology was beleaguered from the dangerousness that can be caused by the radioactivity, since the first day it was developed. Moreover, the specificity of RIA was also questioned by scientists as it utilized only one type of antibody for target recognition. In addition, RIA also does not have the compatibility for performing multiplexed measurements. For all the above reasons, although RIA is still in use in certain applications, it is largely considered as outdated technology.

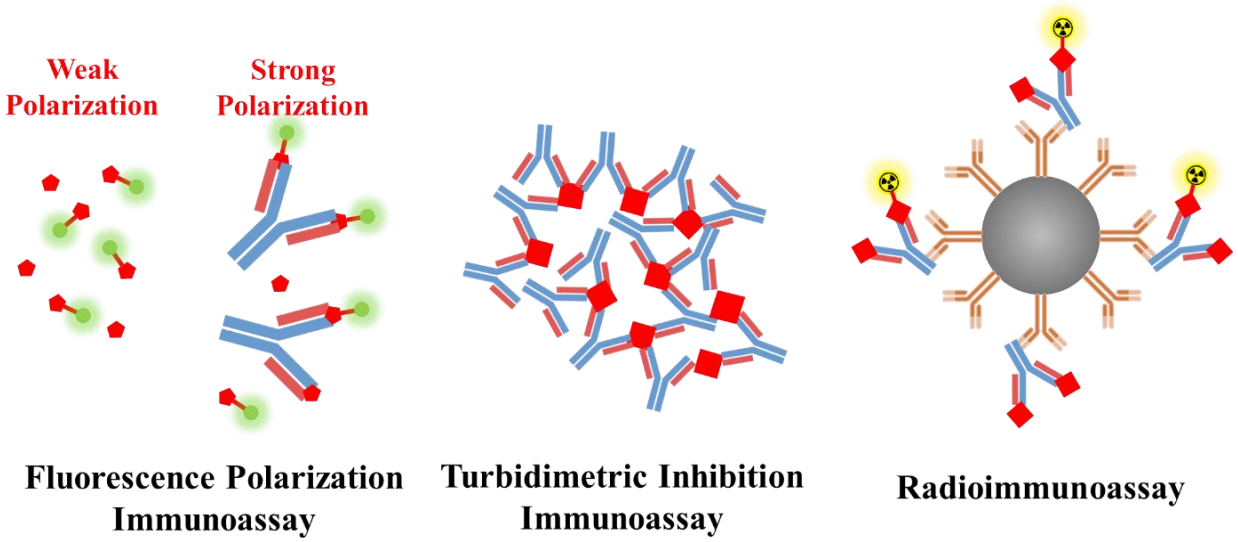

Figure 1.2. Schematic demonstrations of fluorescence polarization immunoassay (FPIA), Turbidimetric inhibition immunoassay (TINIA) and Radioimmunoassay (RIA).

1.3.2. Homogeneous immunoassays through optical readouts

Through decades of researches, scientists generally discovered that the optical signal is very promising in signal transduction for immunoassays as it has high multiplexing capability (through wavelengths), easy to be measured, low disturbance to the sample, and excellent safety (no radioactive source needed)[18].

Scientists have also developed several rinse-free homogeneous immunoassays that can be performed directly in the liquid phase. As examples, fluorescence polarization immunoassay (FPIA) quantifies analyte concentration through measuring the difference in fluorescence polarization after mixing the antibody with sample and analyte-fluorophore conjugate[19-20]; Turbidimetric inhibition immunoassay (TINIA)[21] measures the change in transmittance that was caused by the formation of antigen-antibody complexes (AACs) in bulk solution[22]. However, due to the lack of a signal amplification method, all aforementioned technologies are also suffering from relatively low sensitivity. In addition, each type of these homogeneous immunoassays can

only be applied to a particular type of analyte (small molecule analytes for FPIA and larger analytes for TINIA), so the application universality is also limited. For the wide range of applications that requires highly-quantitative analysis of low abundance targets (e.g., clinical diagnostics of cancer), an assay with high sensitivity is still strongly in desire.

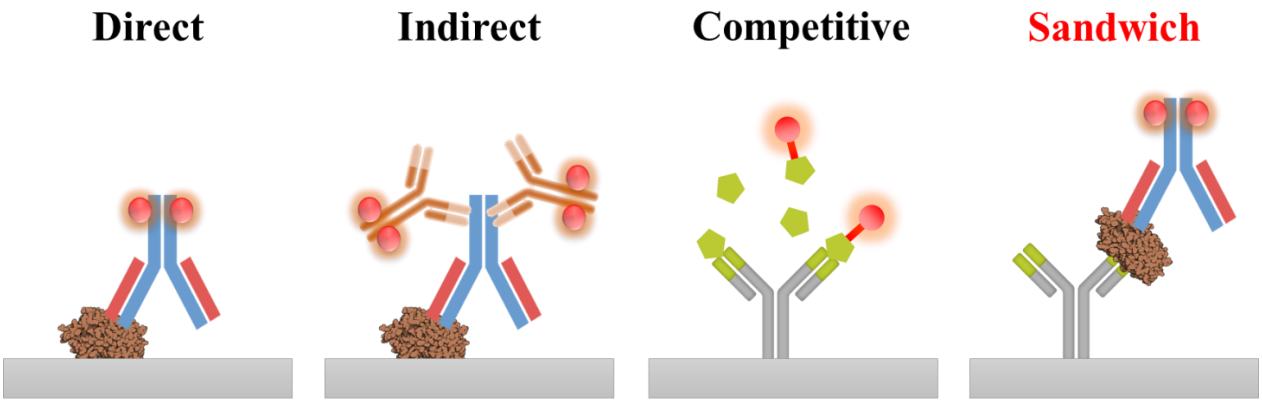

Figure 1.3. The concepts of different types of Enzyme-Linked Immunosorbents Assay (ELISA). Out of them, sandwich ELISA has the best specificity.

1.4. Enzyme-Linked Immunosorbents Assay (ELISA)

To enhance the detection sensitivity in immunoassays, scientists have dedicated their efforts in finding a way to amplify the signal, while maintaining the attractive features of optical detection[23]. As a result, enzyme-based signaling probes were developed as a replacement of radioactive probes and fluorophores[24]. Similar with other types of signaling probes, the enzymes are also conjugated on the antibodies. The enzyme molecules on the antibody can continuously turn colorless substrate molecules into detectable signals (chromogenic molecules, fluorogenic molecules or photons) and ultimately lead to a significantly enhanced signal intensity[25-26]. However, since the enzymatic activity is independent from the binding between the antibody and

the antigen, rinsing steps are always necessary in all enzyme-linked immunoassays. For the same reason, a solid supporting surface is also required[24].

After years of development, several sub-types of ELISA have been developed for various applications. Direct ELISA is the most senior member in this ELISA. In a direct ELISA, the analyte is first immobilized on the supporting surface through physical adsorption. Then, enzyme-conjugated antibodies (detection antibodies) are applied to the surface[27]. As a common last step of all types of ELISAs, the substrate solution is then applied to the surface of the sensor, after washing away all unbound detection antibodies. The concentration of the analyte can be quantified as the signal intensity is directly proportional to the analyte concentration. However, this direct ELISA is still facing several severe challenges. First, there is only one type of antibody that is involved in the assay. So, it doesn't solve the specificity problems of other types of immunoassays. Second, the immobilization of analyte is performed through physical adsorption, thus having a very low efficiency. Only a small portion of the analyte molecule in the sample can be immobilized on the sensor's surface. The low immobilization efficiency also leads to a low signal intensity in the final measurement. To solve the aforementioned reasons, additional types of ELISA are developed.

Indirect ELISA is a variant of direct ELISA, instead of conjugating the reporter enzymes directly on the primary antibody[28], it employs polyclonal secondary antibodies to amplify the signal. But due to the same reason with direct ELISA, the specificity of this assay is highly relying on the selection of antibodies. In most cases, the signal in an indirect ELISA is noisy and does not have an excellent signal-to-noise ratio.

In order to resolve the specificity problems in direct ELISA, scientists introduced another primary antibody (capture antibody) into the detection system, resulting in a sandwich structure[29]. The two antibodies are designed to recognize two unique epitopes on the same molecule[2-3, 30]. A

sandwich ELISA is typically used to detect larger molecules (e.g., proteins) or large particles (e.g., viruses, exosomes) that has multiple binding sites. Briefly, in a sandwich ELISA, capture antibodies are first immobilized on the sensor's surface. Then, the target analytes are added and captured by the capture antibodies. At last, the detection antibodies labelled with enzymes are added and bind to the immobilized analyte molecules. As a result of this double-selection process, only the molecules that can be recognized by both antibodies (capture + detection) are turned into the signal. This will result in a significantly improved signal-to-noise ratio when compared with direct ELISA. Another benefit of having the capture antibody is the enhancement in analyte capture efficiency. This improvement can ultimately lead to a shortened assay time and an enhanced signal intensity. Similar to the direct ELISA, the signal intensity is also directly proportional to the concentration of the analyte. For all aforementioned reasons, sandwich ELISA has become one of the most popular immunoassays due to its high specificity and high reproducibility.

Reporter Enzymes	Catalytic Activity
Glucose Oxidase (GOx)	Low
Beta Galactosidase (β-Gal)	Medium
Alkaline Phosphatase (ALP)	Medium
Horseradish Peroxidase (HRP)	High

Table 1.1. Various types of reporter enzymes for ELISA

Competitive ELISA is another popular form of ELISA. It is designed to detect the molecules that does not have enough room for two antibodies binding simultaneously (e.g., small molecules and small protein)[11, 31]. In this type of assay, enzyme-linked antigens are used as the "competitors" of native analytes in sample solution. Different from other types of ELISAs, in competitive ELISA, the signal intensity is inversely proportional to the analyte concentration in the sample[11].

Till today, several reporter enzymes have been discovered and tested in ELISA applications (see table 1.1), including Alkaline Phosphatase (AP), glucose oxidase (GOx), beta galactose (β-Gal) and horseradish peroxidase (HRP). Out of these enzymes, HRP has the strongest enzymatic activity and an outstanding catalytic specificity so it generally has become the most popular reporter enzyme for ELISA[32]. There are also several types of matched substrate systems that have been developed for ELISA applications. As a type of peroxidase, all HRP substrates must work under the existence of hydrogen peroxide. With excessive amount of hydrogen peroxide, the initial reaction rate is proportional to the immobilized HRP quantity. The most popular substrate for HRP is TMB (3 3' 5 5'-tetramethylbenzidine)[25], it can be turned from a colorless molecule into a chromogenic molecule by HRP. In additional to chromogenic, other types of HRP substrates, including fluorescent substrates (colorless molecules can be turned into fluorogenic molecules)[33] or chemiluminescent substrates[34] (can directly emit photons) are also available on the market.

With the pieces of knowledge about the chemical mechanisms in immune-sensing and enzyme-mediated signal transduction, we can now move forward to the concepts for designing a good immunoassay reactor.

1.5. References

1. Turner, A.; Karube, I.; Wilson, G. S., *Biosensors: fundamentals and applications*. Oxford university press: 1987.
2. Tan, X.; Oo, M. K. K.; Gong, Y.; Li, Y.; Zhu, H.; Fan, X., Glass capillary based microfluidic ELISA for rapid diagnostics. *Analyst* **2017,** *142* (13), 2378-2385.
3. Tan, X.; Chen, Q.; Zhu, H.; Zhu, S.; Gong, Y.; Wu, X.; Chen, Y.-C.; Li, X.; Li, M. W.-H.; Liu, W., A Fast and Reproducible ELISA Laser Platform for Ultrasensitive Protein Quantification. *ACS sens.* **2019**.
4. Tan, X.; Broses, L. J.; Zhou, M.; Day, K. C.; Liu, W.; Li, Z.; Weizer, A.; Munson, K. A.; Oo, M. K. K.; Day, M., Multiparameter Urine Analysis for Quantitative Bladder Cancer Surveillance of Orthotopic Xenografted Mice. *Lab Chip* **2020**.
5. Gizeli, E.; Lowe, C. R., *Biomolecular sensors*. CRC Press: 2002.
6. Bilen, H.; Kilicaslan, A.; Akcay, G.; Albayrak, F., Performance of glucose dehydrogenase (GDH) based and glucose oxidase (GOX) based blood glucose meter systems at moderately high altitude. *J. Med. Eng. Technol.* **2007,** *31* (2), 152-156.
7. Ilkhani, H.; Sarparast, M.; Noori, A.; Bathaie, S. Z.; Mousavi, M. F., Electrochemical aptamer/antibody based sandwich immunosensor for the detection of EGFR, a cancer biomarker, using gold nanoparticles as a signaling probe. *Biosens. Bioelectron.* **2015,** *74*, 491-497.
8. German, I.; Buchanan, D. D.; Kennedy, R. T., Aptamers as ligands in affinity probe capillary electrophoresis. *Anal. Chem.* **1998,** *70* (21), 4540-4545.
9. Wilson, I. A.; Stanfield, R. L., Antibody-antigen interactions. *Curr. Opin. Struct. Biol.* **1993,** *3* (1), 113-118.
10. MacCallum, R. M.; Martin, A. C.; Thornton, J. M., Antibody-antigen interactions: contact analysis and binding site topography. *J. Mol. Biol.* **1996,** *262* (5), 732-745.
11. Xue, W.; Tan, X.; Oo, M. K. K.; Kulkarni, G.; Ilgen, M. A.; Fan, X., Rapid and sensitive detection of drugs of abuse in sweat by multiplexed capillary based immuno-biosensors. *Analyst* **2020**.
12. Phillips, D. D.; Garboczi, D. N.; Singh, K.; Hu, Z.; Leppla, S. H.; Leysath, C. E., The sub-nanomolar binding of DNA–RNA hybrids by the single-chain Fv fragment of antibody S9. 6. *J. Mol. Recognit.* **2013,** *26* (8), 376-381.
13. Diamandis, E. P.; Christopoulos, T. K., *Immunoassay*. Academic Press: 1996.
14. ABRAHAM, G. E.; SWERDLOFF, R.; Tulchinsky, D.; ODELL, W. D., Radioimmunoassay of plasma progesterone. *J. Clin. Endocrinol. Metab.* **1971,** *32* (5), 619-624.
15. Yalow, R. S.; Berson, S. A., Radioimmunoassay of gastrin. *Gastroenterology* **1970,** *58* (1), 1-14.
16. Molinatti, G.; Massara, F.; Strumia, E.; Pennisi, F.; Scassellati, G.; Vancheri, L. *Radioimmunoassay of human growth hormone*; Univ., Turin: 1969.
17. Udenfriend, S.; Gerber, L. D.; Brink, L.; Spector, S., Scintillation proximity radioimmunoassay utilizing 125I-labeled ligands. *Proc. Natl. Acad. Sci.* **1985,** *82* (24), 8672-8676.
18. Rabbany, S. Y.; Donner, B. L.; Ligler, F. S., Optical immunosensors. *Crit. Rev. Biomed. Eng.* **1994,** *22* (5-6), 307-346.

19. Dandliker, W.; Kelly, R.; Dandliker, J.; Farquhar, J.; Levin, J., Fluorescence polarization immunoassay. Theory and experimental method. *Immunochemistry* **1973,** *10* (4), 219-227.
20. Jolley, M.; Stroupe, S.; Schwenzer, K.; Wang, C.; Lu-Steffes, M.; Hill, H.; Popelka, S.; Holen, J.; Kelso, D., Fluorescence polarization immunoassay. iii. an automated system for therapeutic drug determination. *Clin. Chem.* **1981,** *27* (9), 1575-1579.
21. Yang, X.; Shu, W.; Wang, Y.; Gong, Y.; Gong, C.; Chen, Q.; Tan, X.; Peng, G.-D.; Fan, X.; Rao, Y.-J., Turbidimetric inhibition immunoassay revisited to enhance its sensitivity via an optofluidic laser. *Biosens. Bioelectron.* **2019,** *131*, 60-66.
22. Sheriff, S.; Silverton, E. W.; Padlan, E. A.; Cohen, G. H.; Smith-Gill, S. J.; Finzel, B. C.; Davies, D. R., Three-dimensional structure of an antibody-antigen complex. *Proc. Natl. Acad. Sci.* **1987,** *84* (22), 8075-8079.
23. Van Weemen, B.; Schuurs, A., Immunoassay using antigen—enzyme conjugates. *FEBS lett.* **1971,** *15* (3), 232-236.
24. Engvall, E.; Perlmann, P., Enzyme-linked immunosorbent assay (ELISA). *Protides of the biological fluids* **1971**, 553-556.
25. Fanjul-Bolado, P.; González-García, M. B.; Costa-García, A., Amperometric detection in TMB/HRP-based assays. *Anal. Bioanal. Chem.* **2005,** *382* (2), 297-302.
26. Fei, L. H. C. J. X.; Eugenia, C. H. M., Optimization of TMB Substrate Chromogenic System in ELISA and the Study of Its Stability in Storage [J]. *Biotech. Bull.* **2010,** *2*.
27. Beier, J. C.; Perkins, P. V.; Wirtz, R. A.; Koros, J.; Diggs, D.; Gargan, T. P.; Koech, D. K., Bloodmeal identification by direct enzyme-linked immunosorbent assay (ELISA), tested on Anopheles (Diptera: Culicidae) in Kenya. *J. Med. Entomol.* **1988,** *25* (1), 9-16.
28. Koenig, R., Indirect ELISA methods for the broad specificity detection of plant viruses. *J. Gen. Virol.* **1981,** *55* (1), 53-62.
29. Bange, A.; Halsall, H. B.; Heineman, W. R., Microfluidic immunosensor systems. *Biosens. Bioelectron.* **2005,** *20* (12), 2488-2503.
30. Vanmechelen, E.; Vanderstichele, H.; Davidsson, P.; Van Kerschaver, E.; Van Der Perre, B.; Sjögren, M.; Andreasen, N.; Blennow, K., Quantification of tau phosphorylated at threonine 181 in human cerebrospinal fluid: a sandwich ELISA with a synthetic phosphopeptide for standardization. *Neurosci. Lett.* **2000,** *285* (1), 49-52.
31. Lin, A. V., Indirect Elisa. In *ELISA*, Springer: 2015; pp 51-59.
32. Khatkhatay, M. I.; Desai, M., A comparison of performances of four enzymes used in ELISA with special reference to β-lactamase. *J. Immunoassay* **1999,** *20* (3), 151-183.
33. Wu, X.; Oo, M. K. K.; Reddy, K.; Chen, Q.; Sun, Y.; Fan, X., Optofluidic laser for dual-mode sensitive biomolecular detection with a large dynamic range. *Nat. Commun.* **2014,** *5* (1), 1-7.
34. Thorpe, G.; Kricka, L. J.; Moseley, S.; Whitehead, T. P., Phenols as enhancers of the chemiluminescent horseradish peroxidase-luminol-hydrogen peroxide reaction: application in luminescence-monitored enzyme immunoassays. *Clin. Chem.* **1985,** *31* (8), 1335-1341.

Chapter 2

Immunoassay Reactors

2.1. Introductory remark:

In this chapter, we will introduce the layout, features, and limitations of the traditional ELISA reactor. We will also critically review several renovations of ELISA from different perspectives. Finally, we will summarize four general concepts that can be used to guide the development of next-generation ELISA-based biosensors.

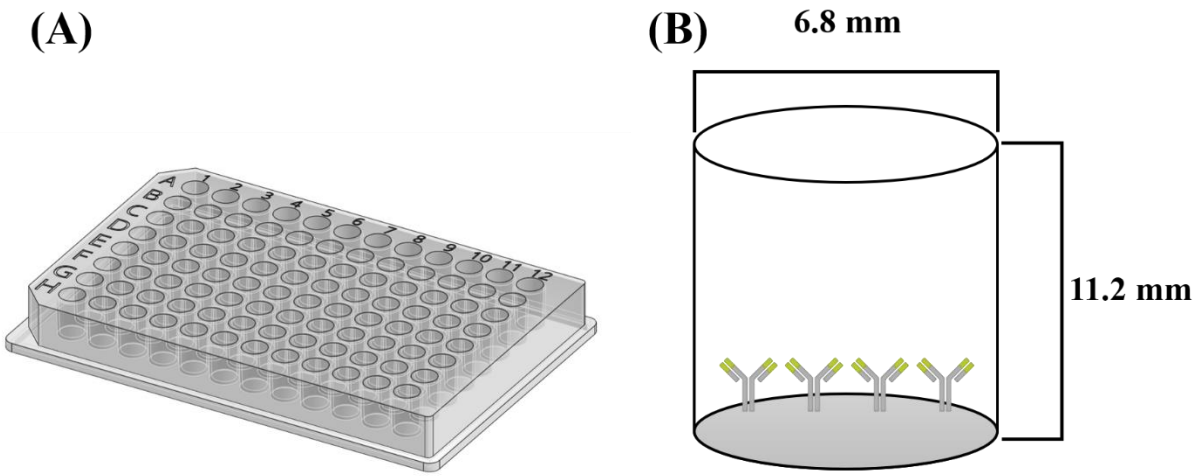

Figure 2.1. Layouts and dimensions of a 96-well plate. (A). General layout of a 96-well plate. (B). Dimensions of a well in the 96-well plate. The bottom of the well serves as the supporting surface in ELISA.

2.2. Traditional plate-based ELISA reactor

As we presented in Fig. 2.1., the typical reactor for most types of ELISA is called microtiter plate (also can be called as microplate)[1]. Since it has a layout with 12×8 wells, it also can be referred as 96-well plates. In a 96-well plate, each well serve as an individual ELISA reactor and the immunosorbent reactions take place on the bottom of the well. In theory, the side wall can also serve as the supporting surface for immunosorbent reactions, but since only the bottom of the well is pre-treated to have high protein affinity, the binding capability of the side wall can be neglected in most cases.

Although the plate's name contains "micro", the dimensions of the reaction wells are in fact quite large. A well in a standard 96-well plate typically has a top diameter of 6.8 mm and a height of 11.2 mm (actual dimensions varies depending on the manufacturers)[2]. Bases on these dimensions, the bottom surface area is $36.32\ mm^2$. When applying 100 µL of liquid (the typical sample volume for a standard ELISA) in the well, the surface-to-volume ratio is only $0.36\ mm^{-1}$. The low surface-to-volume ratio makes the required time of the immunosorbent reactions very long (typically 90-120 minutes for each step, 4-6 hours in total for a sandwich ELISA test). The same problem also limited the optimal sensitivity of the plate-based ELISA.

As a corollary equipment of the microtiter plates, microplate readers are used for taking measurements with traditional plate-based ELISA. A comprehensive microplate reader should be able to take measurement in the forms of light absorbance, fluorescent intensity and chemiluminescent intensity. To fulfill such requirements, the microplate reader needs to be equipped with a few wavelength selective light sources, a spectrometer, and a highly sensitive light sensor. Such requirements make the cost and price of a good microplate reader very high (typically higher than 10000 dollars).

In summary, traditional plate-based ELISA technology still suffers from several notable drawbacks, such as requiring expensive measurement equipment, long assay time (4–6 hours), relatively low sensitivity, burdensome procedures, and large sample/reagent consumption (~100 μL). These inherent disadvantages still significantly limit traditional ELISA's applications in areas such as rapid clinical diagnosis of acute diseases (e.g., sepsis, acute organ rejection) and biological researches that require accurate measurements with precious samples (e.g., tail vein serum from a mouse).

2.3. Existing improvements of ELISA

To overcome the limitations in traditional plate-based ELISA, scientists have tried to innovate it from multiple perspectives. In this section, we will introduce a few representative approaches with different concepts.

2.3.1. Improvements based on the plate-based approaches

As previously introduced, one of the most intrinsic problems for traditional plate-based ELISA is the low sensitivity that was caused by low surface-to-volume ratio. And the "behind-the-scenes" problem is there is not enough immobilized antibody available for analyte binding. Meso Scale Discovery (MSD) developed a carbon-bottomed electro-chemiluminescent immunoassay plate which has stronger affinity toward proteins[3-5]. With this type of plate, the surface density of immobilized antibody is significantly enhanced, compared with traditional polystyrene plates. The specially designed measurement system for this type of assay is composed of an electrode-stimulation unit and an EMCCD (electron multiplying charge-coupled device)-based signal quantification unit[3, 6]. Although this system achieved outstanding detection sensitivity (sub pg/mL level) and very large dynamic range (about 5 orders of magnitude), it does not solve problems such as burdensome procedure and long assay time. In addition, the complicated structures on the plate

and the highly sensitive CCD in the detection system made the cost of the assay tremendously high (the imager itself worth more than 50000 dollars).

Dr. Ozcan's group in UCLA provided another approach to simplify the signal detection instrument of the plate-based ELISA (Fig. 2.2(A)). His group designed a compact and hand-held cellphone-based colorimetric microplate reader as a replacement of the bulky traditional plate reader[7]. The light absorbance measurement was achieved with a light-emitting-diode (LED) array and 96 individual optical fibers. The camera on the cellphone serve as the light sensor in this device. But unfortunately, this invention is still not able to solve the inherent disadvantages of the plate-based ELISA reactor.

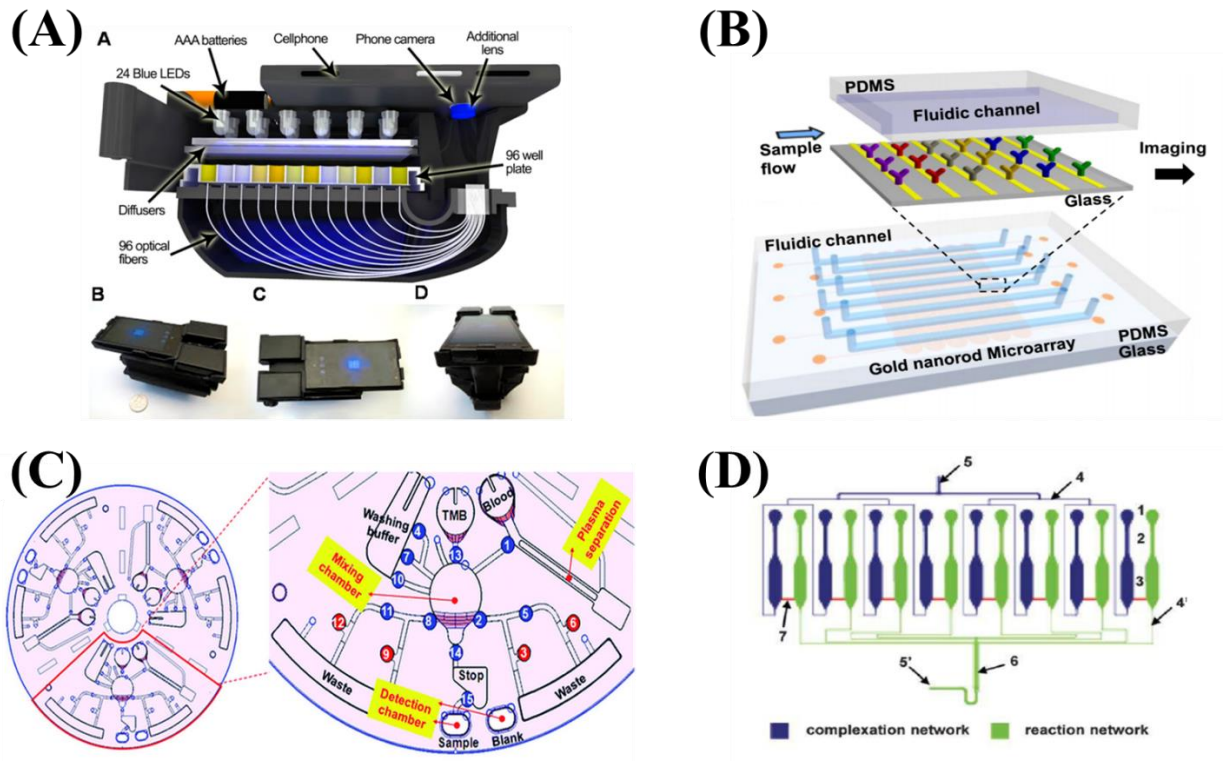

Figure 2.2. Recent modifications on ELISA. (A). A cellphone based 96-well plate reader for colorimetric measurements. (B). An example of SPR-based microfluidic immunoassays. (C). Bead-based ELISA with a centrifugal disc. (D). Microfluidic ELISA in a microfluidic chip.

2.3.2. Optofluidic immunoassays

Recent developments in microfluidic technologies provide a promising solution to address the inherent problems in plate-based immunoassay reactors. The attractive features such as high surface-to-volume can potentially enhance the reaction rate of immunosorbent reactions thus reduce the assay time in the immunoassays. More importantly, the required sample volume for microfluidic reactors are dramatically smaller than plate-based reactors. Despite the advances in other types of signal transduction methodologies (e.g., electrochemical assays, mass-based assays), we will still focus our attention on optofluidic immunoassays, which is a subtype of microfluidic immunoassay that utilizes optical signal for sensing transduction.

In the past two decades, surface plasmon resonance-based (SPR-based) immunoassay has become a popular optical-based method in protein quantification and binding kinetics measurements (including its derivative LSPR)[8]. SPR is a type of electromagnetic resonant oscillation on the interface of negative (e.g., water, air) and positive permittivity material (metals). An SPR is typically stimulated by incident light. Since the oscillation happens on the boundary of the conductor, it is very sensitive to any adsorption of molecules on the surface of the conductor, especially at the resonance wavelength. Thus, it can be used to detect the quantity of molecules that was captured in an immunosorbent assay[8]. Unlike ELISA, SPR immunoassay is a label-free assay (no external labeling is required)[8]. The analyte quantification can be done in real time, through tracking the shift in resonance wavelength. Several groups have successfully integrated SPR sensing components into microfluidic reactors. The schematic diagram of a representative SPR-based microfluidic immunoassay can be found in Fig. 2.2.(B)[9-10]. However, due to lacking the detection antibody and enzyme-mediated signal amplification methods, the specificity and sensitivity of SPR-based immunoassay is still considerably worse than sandwich ELISA. For this

reason, people generally consider SPR-based immunoassay as a powerful tool for binding kinetics measurements (especially for proteins) rather than a tool for biomarker quantification.

The feasibility of performing sandwich ELISA in an integrated optofluidic system such as a PDMS chip, polystyrene chip, and centrifugal disc has also been demonstrated. See Fig. 2.2 (C)-(D) for examples[11-12]. However, most of these approaches involve sophisticated fluidic designs. They usually suffer from low multiplexing capacity, insufficient rinsing (due to residual liquids), low repeatability, strong background, small dynamic range, and low signal-to-noise ratios[2, 13].

Different from the mediocre optofluidic ELISA systems, digital ELISA is a very successful invention in the field of immunoassay (see Fig. 2.3). It separates the bulk sample into thousands of microscale reactors (typically beads with < 5 μm in diameter), and typically each bead can only capture 0 or 1 analyte molecule[14]. Since the reactors are very small, a high local concentration of the enzymatic reaction product can be readily achieved. For each bead-based reactor, only a single molecule is needed to reach the detection limit. Instead of doing bulk measurements of signal intensities, digital ELISA counts the fraction of beads that generate a detectable signal. Since measuring the presence or absence (0 or 1) of the signal is much easier than to detect the absolute intensity of the signal, the lower limit of detection (LLOD) for digital ELISA assay is typically 100-1000 times lower than traditional plate-based ELISA (even using the same pair of antibodies)[14-16].

However, even this powerful invention has its own inherent drawback: the upper limit of detection is typically lower than traditional plate-based ELISA for several folds. This is due to the saturation effect of the molecule-counting approach—digital ELISA is not able to recognize beads with more than one binding molecules. Furthermore, despite the use of microfluidic reactors, all

systems mentioned above still require expensive equipment such as a fluorescent microscope or a PMT (photomultiplier tube)-equipped reader for taking measurements.

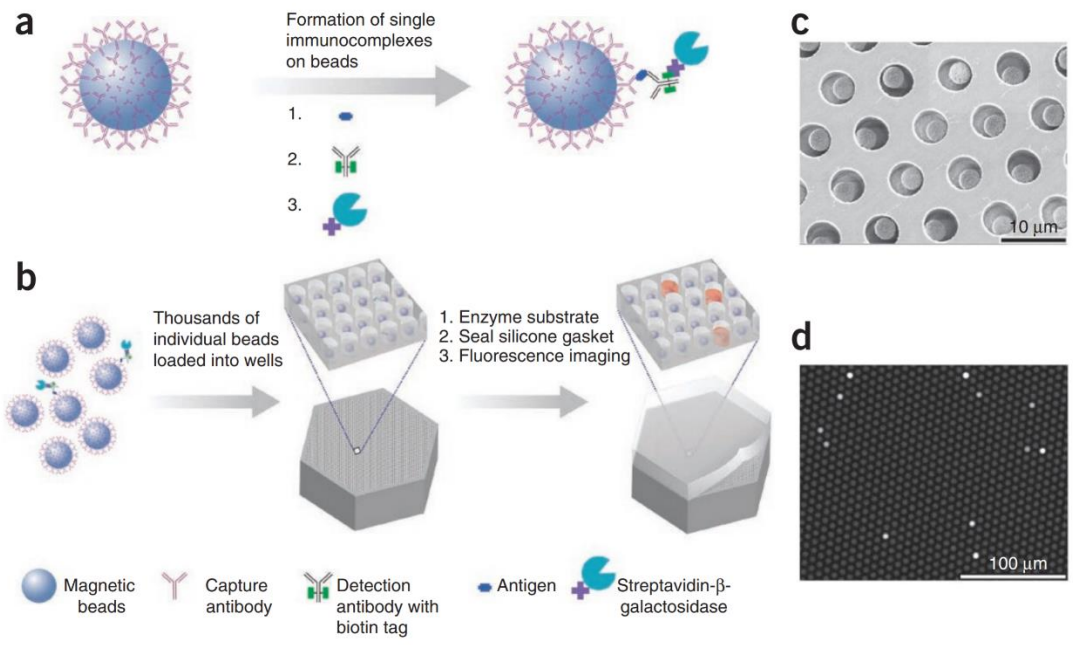

Figure 2.3. Conceptual demonstration of a digital ELISA (Simoa).

2.4. General concepts for improving ELISA-based immunosensors

As the examples listed above, all conventional and new immunoassay technologies have their own advantages and limitations, and a practically feasible and inexpensive immunoassay system with simple design, high speed, high sensitivity, large dynamic range, low sample/reagent consumption, optical readout, and multiplexed capability is still highly desirable. But from the technology roadmaps of the aforementioned technologies, we may be able to summarize a few concepts that is broadly applicable for the development of next-generation solid-phase immunosensor. The illustration of the following concepts can be found in Fig. 2.4.

2.4.1. Enhancing the binding capacity of the reactor

In a sandwich immunoassay, the capture antibody is first immobilized on the sensor's surface. The surface density of the capture antibody is one of the key factors for determining the efficiency of the immunosorbent reaction of analyte molecules (surface-to-volume ratio of the reactor and the binding affinity of antibodies are the other two key factors). For this reason, having a surface with a good protein immobilization affinity is an essential cornerstone for developing a sensitive solid-phase immunosensor. In traditional plate-based ELISA using a polystyrene plate, the immobilization of capture antibody is typically achieved through hydrophobic interactions (a type of physical adsorption). However, the natural strength of hydrophobic interaction between proteins and polymer substrates is not very strong, this will result in a relatively low surface density for the capture antibody. Moreover, if a sensor is using a glass substrate as the binding surface, this hydrophobic interaction does not even happen.

The limitation in physical adsorption can be resolved with the following approaches: 1. Use a material that naturally has a high protein affinity as the solid substrate. The carbon-based reaction plate that was developed by MSD is a good example of this approach[4, 17]. 2. Generate specific functional groups on the surface that can directly bind with proteins (typically amino groups or carboxyl groups). Although the functionalized surface will have a very strong affinity toward proteins, this surface modification process requires very complicated chemical treatments to achieve. Thus, this option is typically selected by large manufacturers (e.g., Thermo Fisher). 3. Enhance the hydrophobicity of the surface so the hydrophobic interaction can become stronger. This process is relatively easy to achieve (through silanization) and is broadly applicable to both polymer-based and glass-based substrates. However, the binding capacity will still be lower than the surface with specific functionalization.

It is worth noting that when increasing the binding affinity of the capture antibodies, the chance of non-specifically adsorbing "noise proteins" or detection antibodies will also increase. So, it is essential to have an efficient blocking protocol for reducing the potential noises. This part will be discussed in detail in the following sections.

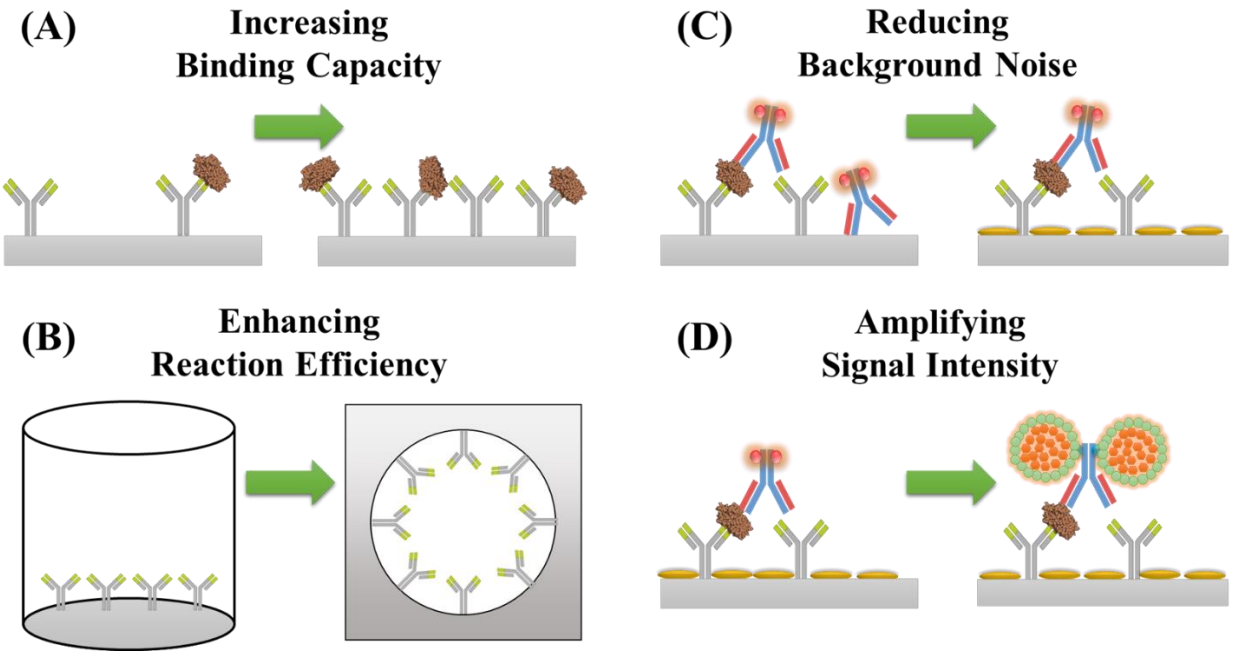

Figure 2.4. General concepts for improving ELISA. (A). Increasing the binding capacity though enhance the surface density of capture antibodies. (B). Enhancing the reaction efficiency through increasing the surface-to-volume ratio. (C). Reducing the background noise through appropriate blocking. (D). Enhancing the absolute signal intensity though enzymatic signal amplifications.

2.4.2. Increasing the surface-to-volume ratio

As we discussed in the previous sections, the surface-to-volume ratio of the reactor is one of the key factors for determining the efficiency in the immunosorbent reactions for all solid phase immunoassays. For a given volume of sample, the reaction efficiency is proportional to the total area that exposed to the sample. In plate-based ELISA, the low surface-to-volume ratio in the reaction wells is one of the "arch-criminals" for the long assay duration.

In general, two approaches are popularly used for enhancing the surface-to-volume ratio in an immunosorbent reaction. Bead-based assays is one of them. Take the digital ELISA as an example, the employment of thousands of microscale beads can maximize the surface area for immunosorbent reactions. Assuming two million beads with 4 μm in diameter (a typical condition for digital ELISA) are mixed with 100 μL of sample, the surface-to-volume ratio will be close to 1 mm^{-1}, which is about three times higher than a typical reaction well in a 96-well plate. Another approach to enhance the surface-to-volume ratio is using microfluidic channels as the reactors of immunosorbent reactions. For example, the surface-to-volume ratio of a circular tubular reactor with 800 μm of diameter is 5 mm^{-1}, which is about 14 time higher than a typical reaction well in a 96-well plate. The technologies equipped with these types of immunosorbent reactor, will definitely have higher reaction efficiencies than the plate-based reactors.

2.4.3. Reducing the background noise

Having a high enough signal-to-noise ratio is another essential requirement for the development of an immunosensor system with high sensitivity and large dynamic range[18]. The typical signal-to-noise ratio for a plate-based ELISA with standard adsorption measurement is around 50 (varies based on the ELISA kits). Any systems with <50 signal-to-noise ratios should not be considered as a good system for highly sensitive analyte quantification. Different from many people's imagination, in the optimization of the signal-to-noise ratio, reducing the noise is probably more important than enhancing the absolute signal. This is especially true for the sensing systems with high protein affinity or high surface-to-volume ratio, or both.

Blocking is a very critical step in noise reduction. People typically use 1-5 % (by mass/volume) high purity bovine serum albumin (BSA) in phosphate buffer solution (PBS) for the blocking in most of the solid-phase immunoassays. For plate-based ELISA, two hours or overnight

blocking with this type of buffer should be sufficient for providing a reasonably low background. But for surfaces with high protein affinity or sensors with high surface-to-volume ratios, this protocol may not be enough. This was partially due to the relatively large size of BSA (~66 kDa). There would be some black space between the immobilized BSA molecules, even after an overnight incubation. This problem can be resolved by introducing another blocking solution in addition to the BSA-based blocking solution[19]. This additional blocker needs to have a smaller molecular size than BSA, high affinity toward the surface, and does not provide any additional noise into the immunoassay. Casein-based buffers (casein is a smaller protein with a ~21 kDa molecular weight) and protein-free blocking buffers may be good candidates for the secondary blocking buffers. Rinsing is another critical step in noise reduction. It is used to remove all unbound molecules from the surface of the sensors. Tween-20-based wash buffer generally have better rinsing performance than pure PBS.

2.4.4. Amplifying the signal

For an immunoassay system with a low background noise, signal amplification becomes the next thing that should be taken into consideration. Appropriate amplification of signal could also enhance the dynamic range of the assay. The selection of detection antibody plays an important role in signal amplification (as well as in noise cancellation). In order to achieve a good signal-to-noise ratio, the detection antibody should have high affinity and very high specificity toward the targeting analyte. It also should not interfere or cross-react with the capture antibody. Note that the detection antibodies are typically biotinylated for signaling purposes. Polyclonal detection antibodies are widely used for detecting low-abundance targets (pg/mL level). They can amplify the signal by 2-3 times (compared with using monoclonal detection antibodies) as one analyte molecule can bind with several antibody molecules that recognize different epitopes. In

ELISA, streptavidin-HRP is typically used for signal transduction and amplification (HRP can also be replaced by other reporter enzymes if needed). As the binding between streptavidin and biotin is very specific, this process generally does not cause any additional noise. People also developed methods for further signal amplification. High sensitivity streptavidin-HRP (2-3 HRP per streptavidin molecule) and streptavidin poly-HRP (>20 HRP per streptavidin molecule) are also widely used in assays that detects analytes with very low abundance[20]. However, these types signal amplification reagents must be handled in a different way than classical streptavidin-HRP. This will be introduced in detail in chapter 6.

Choosing the substrate for signal transduction is another important factor in enhancing the signal-to-noise ratio. Generally, the sensitivity with active measurements (fluorescent, chemiluminescent) is higher than passive measurements (light absorbance). Due to low auto-luminescence, chemiluminescence substrates can generate the highest signal-to-noise ratio under ideal conditions. Correspondingly, the signal quantification system should also be designed appropriately. As a replacement of the comprehensive plate-readers, light sensors such as CCD, CMOS, and spectrometers that have high light sensitivities and large dynamic ranges can be used.

2.4.5. Enhancing the reproducibility of the assay

A successful biosensing system should be a system with high reliability and reproducibility. To achieve this, sophisticated fluidic designs that may cause insufficient rinsing and non-specific binding should be avoided (may result in strong background noise). In addition, automated systems generally have better consistency in results than manually operated systems.

With the rules and concepts summarized above, we should be able to develop a multifunctional optofluidic immunoassay platform with high sensitivity, large dynamic range, short assay duration and low sample/reagent consumption (see Fig. 2.5 for conceptual illustration).

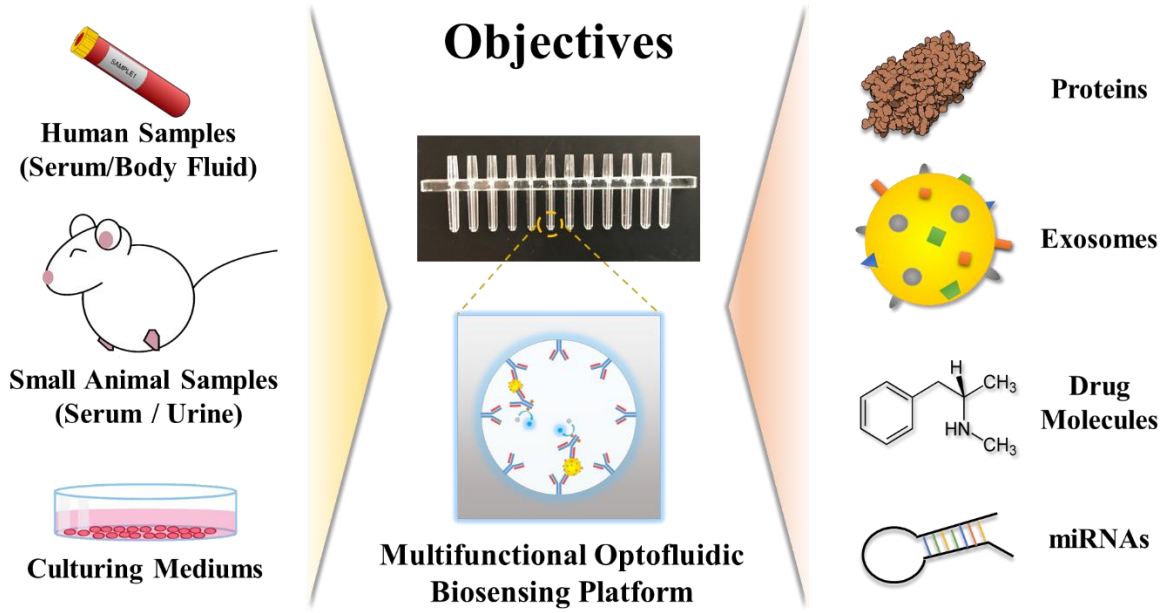

Figure 2.5. Illustration of the functions of the proposed highly sensitive optofluidic biomolecular sensing platform. The samples can be collected from a wide range of sources, including human samples (blood/serum/urine), small animal samples (serum/urine) and cell culturing medium samples. The proposed detection targets including proteins, exosomes, small molecules and miRNAs.

2.5. References

1. Engvall, E.; Perlmann, P., Enzyme-linked immunosorbent assay (ELISA). *Protides of the biological fluids* **1971**, 553-556.
2. Tan, X.; Oo, M. K. K.; Gong, Y.; Li, Y.; Zhu, H.; Fan, X., Glass capillary based microfluidic ELISA for rapid diagnostics. *Analyst* **2017,** *142* (13), 2378-2385.
3. Pavkovic, M.; Riefke, B.; Gutberlet, K.; Raschke, M.; Ellinger-Ziegelbauer, H., Comparison of the MesoScale Discovery and Luminex multiplex platforms for measurement of urinary biomarkers in a cisplatin rat kidney injury model. *J. Pharmacol. Toxicol. Methods* **2014,** *69* (2), 196-204.
4. Burguillos, M. A., Use of meso-scale discovery™ to examine cytokine content in microglia cell supernatant. In *Microglia*, Springer: 2013; pp 93-100.
5. Chowdhury, F.; Williams, A.; Johnson, P., Validation and comparison of two multiplex technologies, Luminex® and Mesoscale Discovery, for human cytokine profiling. *J. Immunol. Methods* **2009,** *340* (1), 55-64.
6. Steinkellner, H.; Scheiber-Mojdehkar, B.; Goldenberg, H.; Sturm, B., A high throughput electrochemiluminescence assay for the quantification of frataxin protein levels. *Anal. Chim. Acta* **2010,** *659* (1-2), 129-132.
7. Berg, B.; Cortazar, B.; Tseng, D.; Ozkan, H.; Feng, S.; Wei, Q.; Chan, R. Y.-L.; Burbano, J.; Farooqui, Q.; Lewinski, M., Cellphone-based hand-held microplate reader for point-of-care testing of enzyme-linked immunosorbent assays. *ACS nano* **2015,** *9* (8), 7857-7866.
8. Homola, J.; Piliarik, M., Surface plasmon resonance (SPR) sensors. In *Surface plasmon resonance based sensors*, Springer: 2006; pp 45-67.
9. Chen, P.; Chung, M. T.; McHugh, W.; Nidetz, R.; Li, Y.; Fu, J.; Cornell, T. T.; Shanley, T. P.; Kurabayashi, K., Multiplex serum cytokine immunoassay using nanoplasmonic biosensor microarrays. *ACS Nano* **2015,** *9* (4), 4173-4181.
10. Song, Y.; Chen, P.; Chung, M. T.; Nidetz, R.; Park, Y.; Liu, Z.; McHugh, W.; Cornell, T. T.; Fu, J.; Kurabayashi, K., AC electroosmosis-enhanced nanoplasmofluidic detection of ultralow-concentration cytokine. *Nano Lett.* **2017,** *17* (4), 2374-2380.
11. Lee, B. S.; Lee, J.-N.; Park, J.-M.; Lee, J.-G.; Kim, S.; Cho, Y.-K.; Ko, C., A fully automated immunoassay from whole blood on a disc. *Lab Chip* **2009,** *9* (11), 1548-1555.
12. Herrmann, M.; Roy, E.; Veres, T.; Tabrizian, M., Microfluidic ELISA on non-passivated PDMS chip using magnetic bead transfer inside dual networks of channels. *Lab Chip* **2007,** *7* (11), 1546-1552.
13. Weng, X.; Gaur, G.; Neethirajan, S., Rapid detection of food allergens by microfluidics ELISA-based optical sensor. *Biosensors* **2016,** *6* (2), 24.
14. Rissin, D. M.; Kan, C. W.; Campbell, T. G.; Howes, S. C.; Fournier, D. R.; Song, L.; Piech, T.; Patel, P. P.; Chang, L.; Rivnak, A. J., Single-molecule enzyme-linked immunosorbent assay detects serum proteins at subfemtomolar concentrations. *Nat. Biotechnol.* **2010,** *28* (6), 595.
15. Rissin, D. M.; Walt, D. R., Digital readout of target binding with attomole detection limits via enzyme amplification in femtoliter arrays. *J. Am. Chem. Soc.* **2006,** *128* (19), 6286-6287.
16. Cohen, L.; Walt, D. R., Single-molecule arrays for protein and nucleic acid analysis. *Annu. Rev. Anal. Chem.* **2017,** *10*, 345-363.

17. Umek, R. M.; Eason, P. D.; Maheshwari, G.; Mathew, A.; Woods, D., Assay electrode having immobilized lipid/protein layers, methods of making the same and methods of using the same for luminescence test measurements. Google Patents: 2014.
18. Tan, X.; Broses, L. J.; Zhou, M.; Day, K. C.; Liu, W.; Li, Z.; Weizer, A.; Munson, K. A.; Oo, M. K. K.; Day, M., Multiparameter Urine Analysis for Quantitative Bladder Cancer Surveillance of Orthotopic Xenografted Mice. *Lab Chip* **2020**.
19. Vogt Jr, R. V.; Phillips, D. L.; Henderson, L. O.; Whitfield, W.; Spierto, F. W., Quantitative differences among various proteins as blocking agents for ELISA microtiter plates. *J. Immunol. Methods* **1987,** *101* (1), 43-50.
20. Ojeda, I.; Moreno-Guzmán, M.; González-Cortés, A.; Yáñez-Sedeño, P.; Pingarrón, J., Electrochemical magnetoimmunosensor for the ultrasensitive determination of interleukin-6 in saliva and urine using poly-HRP streptavidin conjugates as labels for signal amplification. *Anal. Bioanal. Chem.* **2014,** *406* (25), 6363-6371.

Chapter 3

Glass Capillary Based Microfluidic ELISA

3.1. Introductory Remarks

In this chapter, we will introduce the first manually operated prototype of the optofluidic ELISA, which is a microfluidic chemiluminescent ELISA that uses glass capillaries as the immunoassay reactors. A single lens reflex (SLR) camera was used as the signal detector. We successfully achieved sensitive biomarkers quantification in very short assay durations (15 - 40 min). Note that this chapter was published on *Analyst* in 2017.

3.2. Motivations

As we introduced in chapter 1 and 2, advances in microfluidic technologies provide a promising solution to address problems such as long assay duration and large sample consumption that occurs in conventional 96-well plate-based ELISA. However, most of the existing approaches involve sophisticated fluidic designs and usually suffer from low multiplexed capacity, insufficient rinsing (due to residual liquids), low repeatability, strong background, small dynamic range, and low signal-to-noise ratios [5, 14]. Furthermore, despite the use of microfluidics, the entire device still requires expensive equipment such as fluorescent microscope [5] or photomultiplier tube (PMT) equipped reader [15] to take measurement. Consequently, a practically feasible and inexpensive ELISA device with simple design, high speed, high sensitivity, large dynamic range, low sample/reagent consumption, and multiplexed capability is highly desirable.

Benefitting from the high surface-to-volume ratio, small sample consumption, and structural simplicity, capillaries provide another microfluidic platform for ELISA. Over the past few years, the standard or simplified versions of ELISA have been carried out using thin microfluidic glass capillaries (0.1 mm × 0.1 mm for inner dimensions, wall thickness 0.1 mm), showing that the immunoassay can be quantified either fluorescently or colorimetrically with a fluorescent microscope [16-19] or a transmitting light detector [20]. However, in those capillary systems, samples and reagents are delivered via the capillary force, which is difficult to control. Consequently, they suffer from low repeatability, low reliability, high background (due to the incomplete rinse of the liquid residuals at the capillary corners), and low sensitivity and dynamic range. Moreover, since fluorescent or colorimetric substrates are used in those systems, additional 15-30 minutes of enzyme-substrate reaction time is needed to generate a detectable signal, which is a bottleneck for further reduction in total assay time.

Here we developed a user-friendly glass capillary based microfluidic ELISA device. The capillaries were chemically pre-activated before starting a sandwich ELISA. Thanks to the high surface-to-volume ratio of the capillary and the rapid chemiluminescent imaging method (with a commercial camera), this technique significantly reduced the sample volume to 20 μL and shortened the total assay time to around 16 minutes (including the final chemiluminescence measurement), which is considerably faster and simpler than existing microfluidic approaches. In comparison with the traditional ELISA using 96-well plates, our capillary based microfluidic ELISA has >10-fold reduction in assay time, 5-fold reduction in sample/reagent consumption volumes, and ~10-fold enhancement in the dynamic range (from 2.5 orders to ~4 orders of magnitude), while maintaining comparable sensitivity.

3.3 Materials and Methods

3.3.1 Materials

The chemiluminescent substrate (SuperSignal™ ELISA Femto Substrate) was purchased from Thermo Fisher. The substrate kit (product no. 37075) contains a bottle of 50 ml Luminol + Enhancer Solution and a bottle of 50 ml Stable Peroxide Solution. The working substrate solution was prepared by equal-volumetrically mixing the Luminol + Enhancer Solution and the Stable Peroxide Solution at room temperature. The human serum (from human male AB plasma) used in this experiment was purchased from Sigma-Aldrich (product number H4522). The reagents used for surface activation, 3-APTMS, toluene and methanol, were purchased from Sigma-Aldrich.

For interleukin-6 (IL-6) ELISA, Human IL-6 DuoSet ELISA Kit (DY206), ELISA Plate-coating buffer (1×PBS, DY006), wash buffer (WA126) and reagent diluent (10% BSA in 10×PBS, DY995) were purchased from R&D Systems. The stock solutions of the capture antibody, detection antibody and Human IL-6 standard were prepared according to the procedure described in the kits' user manual. The working solution of wash buffer and reagent diluent were diluted with Milli-Q water (R=18.2 Ω) to achieve 1× working concentration. The 1× reagent dilute solution (1% BSA in PBS) was further used as blocking buffer. In this set of experiment, the capture antibody stock solution was diluted with PBS buffer and finally achieved a concentration of 10 μg/ml (working concentration). The working solution of biotinylated detection antibody was prepared by diluting the stock solution with 1× reagent diluent and finally achieved an antibody concentration of 0.3 μg/ml (the detection antibody was biotinylated by the manufacturer). The concentrated Human IL-6 standard was diluted to a desired concentration with 1× reagent diluent or human serum (H4522). The working solution of Streptavidin-HRP conjugate (SAv-HRP) was prepared by diluting the stock solution (included in DY206 kit) to 1/20 of its original concentration

(with 1× reagent diluent). The concentrations of the working solutions were identical for both capillary based and 96-well plate based ELISA.

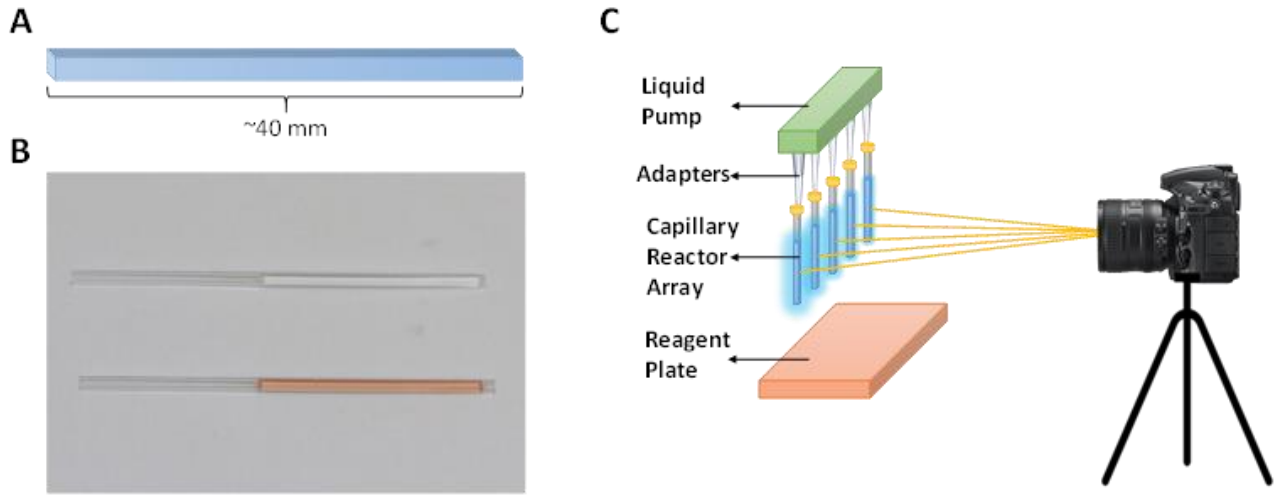

Figure 3.1. Glass capillary-based microfluidic ELISA reactor. (A). A schematic of the glass capillary. (B). A picture of the glass capillary reactors. (C). A schematic of the experimental setup. A 12-channel pipette was used as a liquid pump, pipette tips were used as adapters, PCR tubes were used as sample/reagent reservoirs, a Canon 80D SLR camera was used as an imager.

For CK-MB ELISA, the CK-MB protein standard (AKC0325) was purchased from Thermo Fisher. A mouse monoclonal antibody (ab19603) and a goat polyclonal antibody (ab110655) were used as the capture antibody and the detection antibody, respectively, both of which were purchased from Abcam. Same as the IL-6 experiments, the stock solution of ELISA Plate-coating buffer (DY006), wash buffer (WA126) and reagent diluent (DY995) were purchased from R&D Systems. The working solution of wash buffer and reagent diluent were diluted with Milli-Q water (R=18.2 Ω) to achieve 1× working concentration. In CK-MB experiments, 2× reagent dilute solution (2% BSA in PBS) was used as blocking buffer. The working solution of capture antibody was prepared by diluting the stock solution with PBS buffer to achieve a final concentration of 8 μg/ml. The concentrated Human CK-MB standard was diluted to a desired

concentration with 1× reagent diluent or human serum (H4522). Since the detection antibody was not pre-conjugated with biotin or reporter enzyme, it was modified by conjugating with HRP in a molar ratio of Antibody:HRP=1:4. The conjugation reaction was performed covalently with Abcam's HRP Conjugation Kit (ab102890). The concentration of HRP-conjugated detection antibody stock solution was 1 mg/ml. It was further diluted with 1× reagent diluent and finally achieved a working antibody concentration of 0.7 μg/ml. The concentrations of the working solutions were identical in both capillary based and plate based ELISA assays.

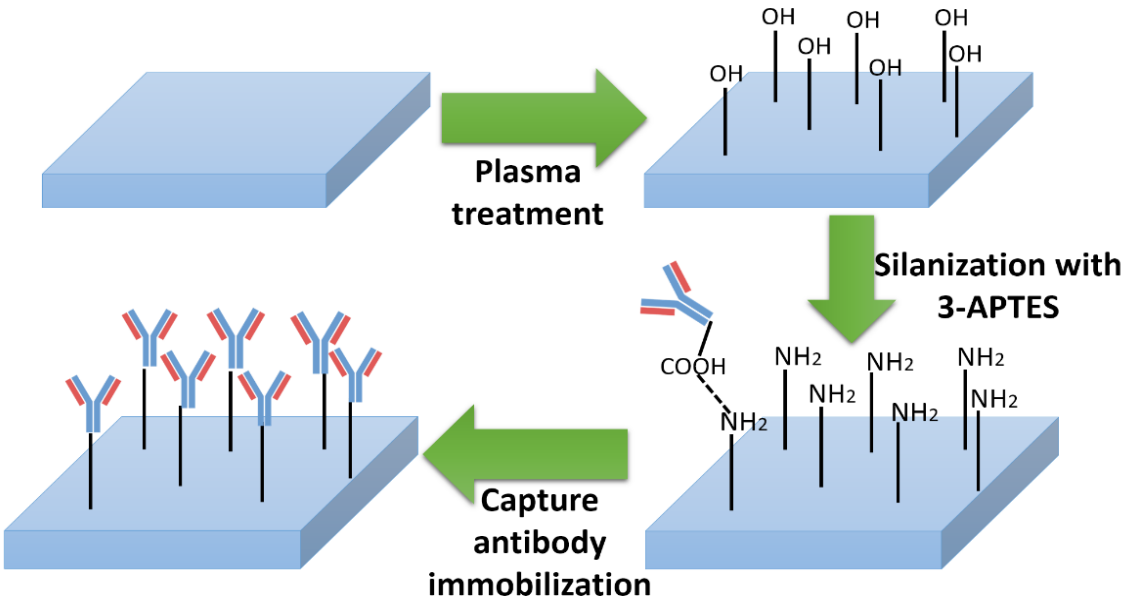

Figure 3.2. Mechanism of surface chemical activation. Air plasma treatment can promote hydroxylation on glass surface, thus facilitates silanization with 3-APTES. The silanized glass surface will have a monolayer of free amino group, which has a high affinity toward free carboxyl groups on the proteins (can be found on Aspartic acid, Glutamic acid and c-terminus of proteins).

The borosilicate glass capillaries (1 mm × 1 mm inner cross section, 150 μm wall thickness, and 30.5 cm in length) were purchased from Friedrich & Dimmock and then cut into 4 cm long pieces with a ceramic wafer. The volume of the entire capillary was 40 μl. During our experiments, we used only a half of it (i.e., 20 μl).

3.3.2. Preparation of capillary reactors

In order to reduce the impact by liquid residue at the corners of reactors and increase the signal intensity generated in each capillary, we decided to use capillary reactors with relatively large interior dimensions (1 mm×1 mm). Fig. 3.1 (A) and (B) show the exterior appearance of capillary ELISA reactors. In order to improve the protein affinity of the capillaries, we performed surface chemical activation on the capillary inner surface, as illustrated in Fig. 3.2.

The activation process is composed of three steps: 1. Treat with air plasma for 5 minutes with a plasma etching machine (for cleaning and hydroxylation). 2. Incubate with 20 mM 3-APTES toluene solution overnight (for anchoring a layer of 3-APTES). 3. Rinse with toluene and methanol (for removal of unbounded 3-APTES). The activated glass surface is coated with a layer of primary amino groups, which are reactive with the free carboxyl groups that can be found on aspartic acid, glutamic acid, and c-terminus of proteins. Since the amount of free carboxyl groups is limited by the number of available amino acids, this approach will generate a modest, but not overly strong affinity toward proteins, thus lowering the risk of non-specific bindings. The capillaries can be batch-processed (up to 200 capillaries per batch) to ensure the consistency in surface activation and subsequent ELISA. The surface activated capillaries are stable and can be stored at room temperature (soaked in deionized water) for over two months without reduction in protein affinity. The activated capillaries were then glued onto pipette tips (Fisherbrand 200 μl pipette tips). 12 capillary reactors were then connected with a liquid pump (in this case, a Scilogex 5-50 μl 12-channel pipette) to form a capillary reactor array.

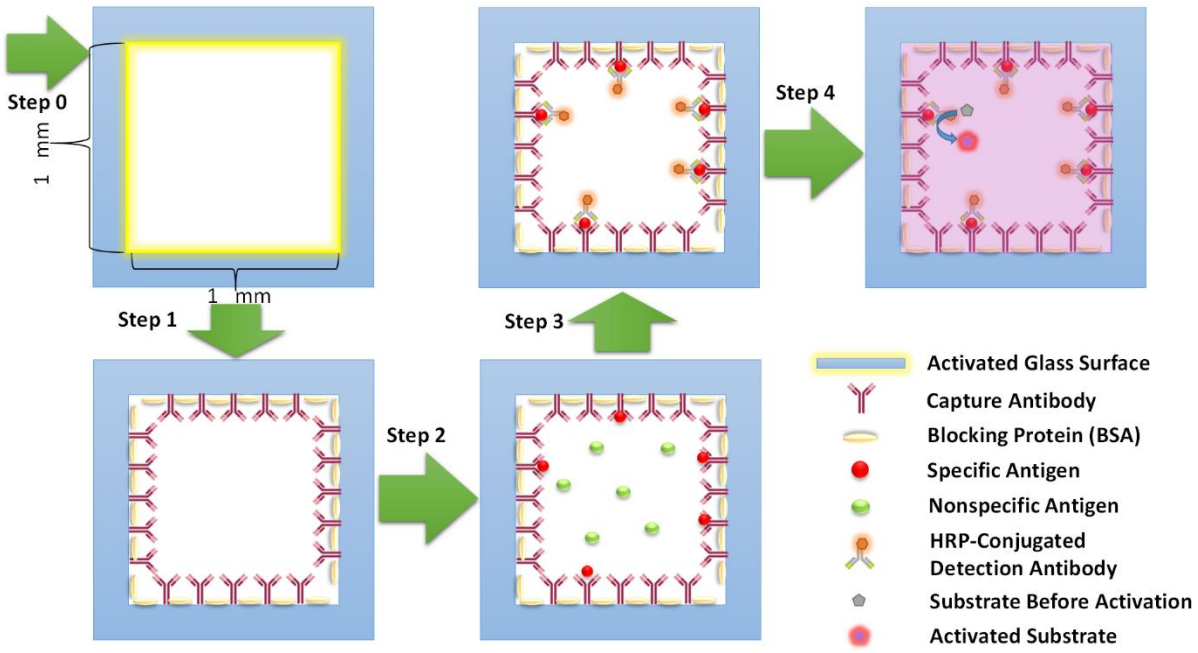

Figure 3.3. Procedures for running ELISA in a glass capillary. Step 0: Surface activation; Step 1: Capture antibody immobilization and surface blocking. Step 2: Sample addition and incubation. Step 3: Detection antibody addition and incubation. Step 4: Substrate addition and measurement.

3.3.3. Experimental setup

A schematic diagram of the experimental setup is shown in Fig. 3.1(C). For chemiluminescent imaging, a Canon 80D SLR camera equipped with a Canon EF 100 mm f/2.8L Macro IS USM Lens was used as an image detector. When taking measurement, the camera was connected to a tripod and placed 45 cm from the focal plane (the distance from the lens to capillaries). Owing to the adjustable negative pressure generated by the multi-channel pipette, the capillaries can accurately draw liquid from the reagent plate and maintain the liquid level. Consequently, the entire assay, including incubation, rinsing, and measurement can all be performed when the capillaries are positioned vertically. During the assay, we usually drew only 20 μl of samples/reagents into the capillary.

Figure 3.3. Illustrated a detailed schematic of a standard sandwich ELISA performed in a glass capillary reactor. The reaction contains 4 steps: 1. Capture antibody immobilization and surface blocking. 2. Sample addition and incubation. 3. Detection antibody addition and incubation. Note that in this step if the detection antibody is not pre-conjugated with reporter enzymes such as HRP (Horseradish peroxidase), an additional step for enzyme conjugation is needed. 4. Substrate addition and final measurement with the camera. The time for Steps 1-3 may vary, depending on the analytes. Between two adjacent steps, waste liquid discharge and 4 times of rinsing with wash buffer are carried out.

3.4. Results and Discussion

Unlike fluorescent or colorimetric substrates that requires 15-30 minutes of reaction time to generate adequate signal, chemiluminescent ELISA substrate can generate detectable optical signal immediately after it reacts with the reporter enzyme (HRP, in this work) conjugated on the detection antibody. The emission intensity of SuperSignal™ substrate remains steady for several minutes. Therefore, the signal intensity during this plateau period can be quantified by the imaging method with a camera.

According to the emission spectrum shown in Fig. 3.4 (A), a large portion of the emitting light has a wavelength between 375 nm and 525 nm. Fig. 3.4 (B) describes the procedure to generate analyzable data from an image. In order to enhance the signal intensity and reduce unrelated background noises, only the signal from the blue channel, which covers the spectral range of 420 – 520 nm, was analyzed. To avoid the potential disturbance caused by light reflection at the capillary edges, only the intensity along the central axis of each capillary was recorded and then averaged along the capillary longitudinal direction.

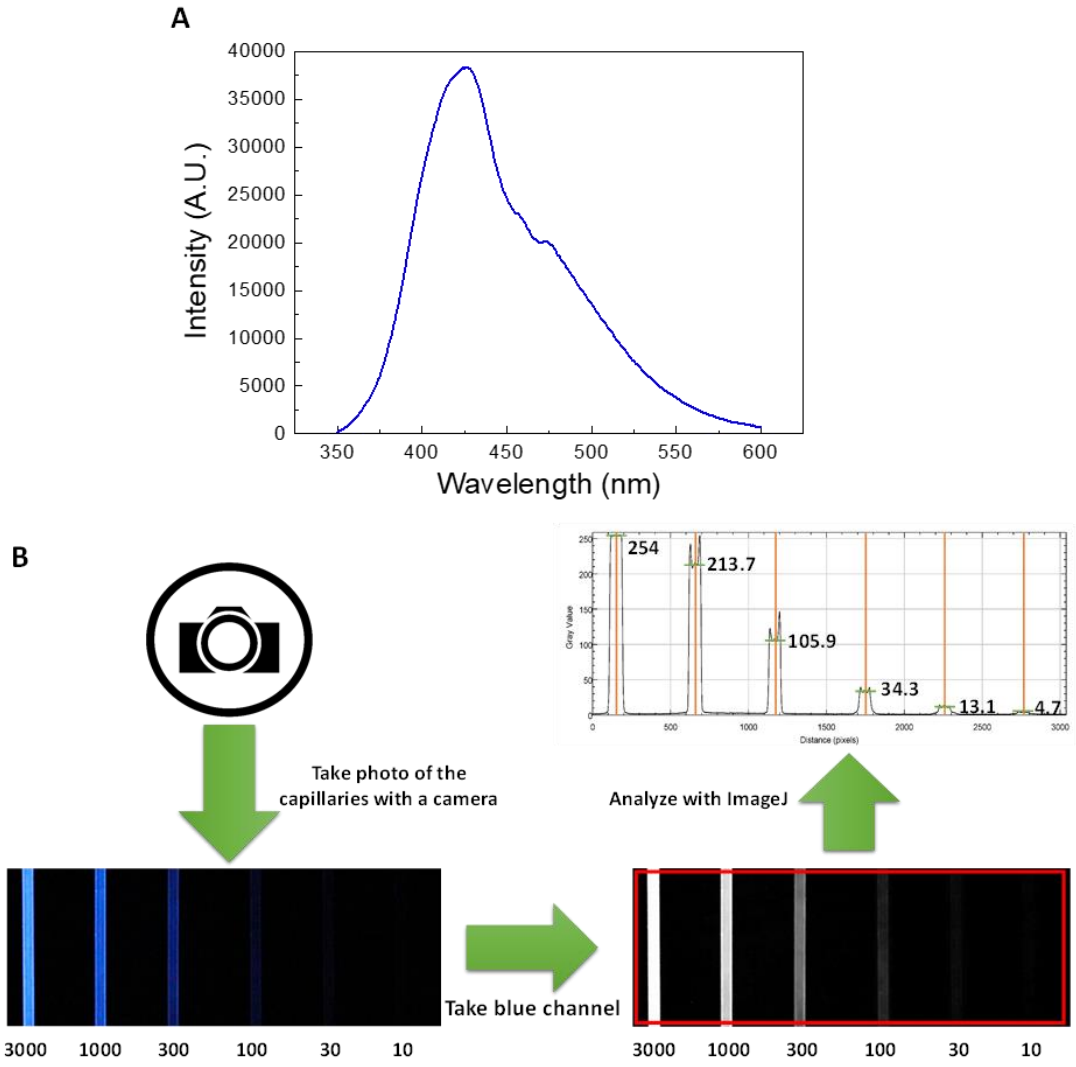

Figure 3.4. Chemiluminescent ELISA signal quantification. (A) Emission spectrum of SuperSignal™ chemiluminescent ELISA substrate (Luminol-based substrate). (B) Procedures of signal quantification. The signal from the blue channel was extracted and analyzed. A plot profile of light intensity was generated with ImageJ. The red box indicates the light intensity measurement region. The numbers under each capillary are the corresponding IL-6 concentration in a sample (in units of pg/mL).

The capillary based microfluidic ELISA system was evaluated with several clinically important biomarkers. We first chose to use human IL-6, which is a widely-used indicator of inflammatory response status and also a marker for immunological diseases such as sepsis and acute organ rejection [21, 22]. The corresponding ELISA protocol is illustrated in Fig. 3A. Note that, since the detection antibody provided in the commercial IL-6 ELISA kit was only biotinylated but

not pre-conjugated with the reporter enzyme (HRP), a HRP conjugation step was preformed after detection antibody incubation (through biotin-streptavidin interaction). Due to the high surface-to-volume ratio (4 mm^{-1} for our capillary reactor, in comparison to 0.32 mm^{-1} for a typical well on a microplate) and short diffusion distance of the capillaries, during the IL-6 ELISA the sample incubation time was shortened to only 15 minutes, and the incubation time for detection antibody and HRP was also shortened significantly to 12 minutes and 7 minutes, respectively. Furthermore, the quadruplicated rinsing took only 1.5 minutes. Altogether, the total assay time from sample addition to final reading was reduced to only 40 minutes, approximately 8 times faster than 320 minutes needed for the traditional 96-well plate based ELISA according to the manufacturer's protocol.

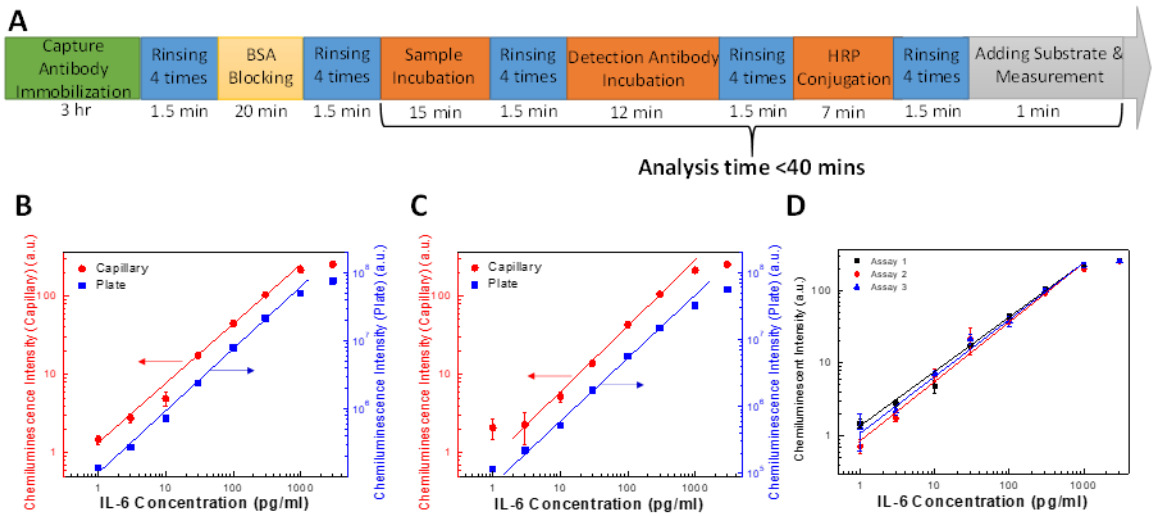

Figure 3.5. IL-6 results. (A). Protocol of running sandwich IL-6 ELISA in capillary reactors. The total assay time is less than 40 minutes. (B). ELISA measurement of IL-6 in buffer solution with capillary reactors and a 96-well plate. (C). ELISA of IL-6 in human serum with capillary reactors and a 96-well plate. (D). The performance of ELISA measurement of IL-6 in buffer solution in three different trials using capillary reactors. Error bars are obtained from triplicate measurements. Camera setting: f=5.6, ISO=6400 and exposure time=30 s.

The capillary-based ELISA measurement of IL-6 in buffer solution (1% BSA in PBS) and human serum are shown in Figs. 3.5 (B)-(C), respectively. The linear dynamic range is 1-1000 pg/ml and 3-1000 pg/ml for IL-6 in buffer and human serum, respectively. The response curves generated with buffer solution and human serum also appear to have high consistency with each other. For comparison, Figs. 3.5 (B)-(C) also plot the ELISA measurements of the same IL-6 samples using traditional 96-well plates and an ELISA reader (PerkinElmer EnSpire 2300 multimode plate reader), showing that, despite 8-fold reduction in assay time (40 minutes vs. 320 minutes) and 5-fold reduction in samples/reagents volume (20 μl vs. 100 μl), our capillary-based microfluidic ELISA system is able to generate results comparable with 96-wel plate based chemiluminescent ELISA. In addition, the capillary based ELISA was found to have good reproducibility among assays performed on different days. Figure 3D indicates the slopes of the regression lines for different IL-6 assays are very close to each other. The slopes are within the range of 0.781 ± 0.033 on the log-log scale, which means the SD $\leqslant \pm 4.24\%$ of average slope.

To validate broader applicability of the capillary based microfluidic ELISA system, we further chose Creatine Kinase-isoform MB (CK-MB), a diagnostic/prognostic marker for myocardial infarction, as the second analyte. Since myocardial infarction is a progressive aggravating deadly disease, rapid quantification of the CK-MB level in serum is crucial to saving patient's life. To further reduce the assay time, we pre-conjugated HRP molecules on the detection antibodies (by amino group crosslinking) with approximately four HRP molecules for one antibody molecule. The revised protocol for CK-MB measurement is illustrated in Fig. 4A, showing the total assay time of only 16 minutes.

The capillary based ELISA measurement of CK-MB in buffer solution (1% BSA in PBS) and human serum are shown in Figs. 4B and C, respectively, showing the linear dynamic range in the log-log scale of 0.1 – 30 ng/ml and 0.3 – 30 ng/ml. For comparison, Figs. 4B and C also plot the ELISA measurements of the same CK-MB samples using traditional 96-well plates and an ELISA reader (which requires a total assay time of 210 minutes and 100 µl sample/reagent volume). Note that due to the existence of background CK-MB (~1 ng/ml) in human serum, a sudden change in the slope for both capillary and traditional ELISA is observed near the lower end of the CK-MB concentration in Fig. 4C. In both Figs. 3.6 (B)-(C), the clinically relevant range of CK-MB concentration in serum is marked with the grey shades for normal people (0.2 – 4 ng/ml) and red shades for patients with myocardial infarction (4 – 32 ng/ml) [23, 24], which is well within the linear response range of the capillary based ELISA system.

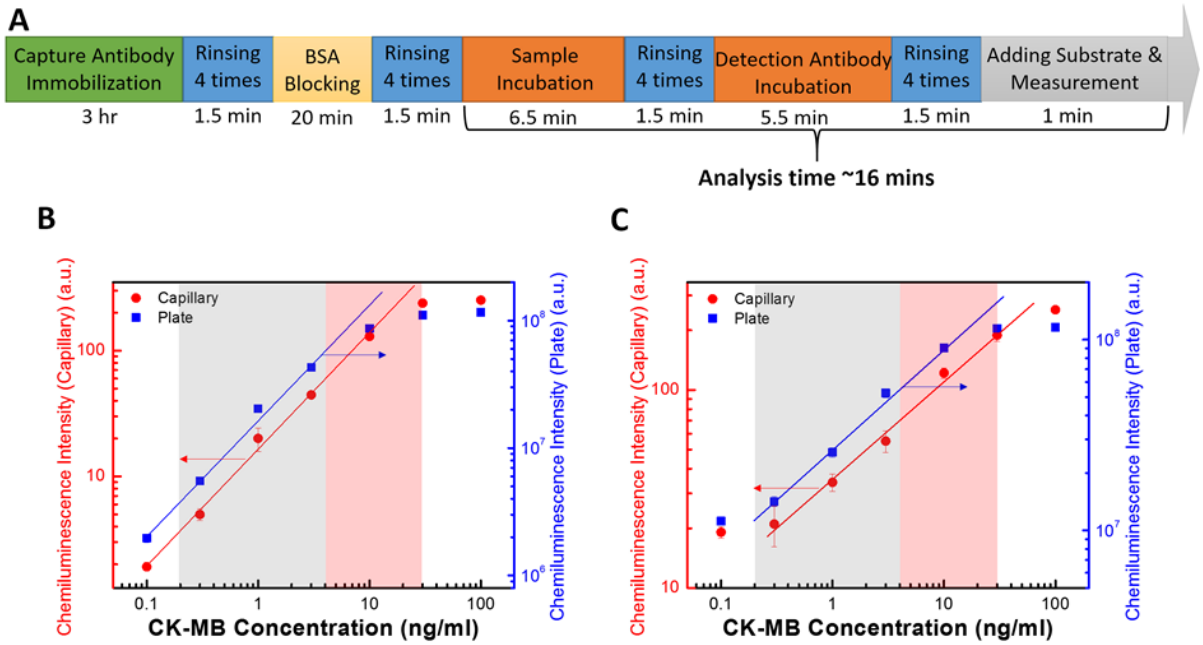

Figure 3.6. CK-MB results. (A). Protocol of CK-MB ELISA in capillary reactors. In this case, HRP was pre-conjugated on detection antibody. The total assay time is around 16 minutes. (B). Response curves of CK-MB ELISA in buffer solution with capillary reactors and a 96-well plate. (C). Response curves of CK-MB ELISA in human serum with capillary reactors and a 96-well plate. Grey shaded areas indicate the range for normal people and red shaded areas indicate the range for myocardial infarction patients.

Our final task in the development of the capillary based ELISA system is to extend its linear dynamic range. Here we used CK-MB in Fig. 3.6 as the model system to illustrate our approach. Figs. 4B and C show that saturation occurs near the upper end of each response curve, which is caused by the long exposure time of the camera. Fig. 3.7 suggests that the response of the CMOS on the camera remains linear when the light intensity is between 0 and 160 counts and starts to level off beyond 160 counts. Therefore, if we keep the intensity counts below 160 using different exposure times, the linear dynamic range can be extended.

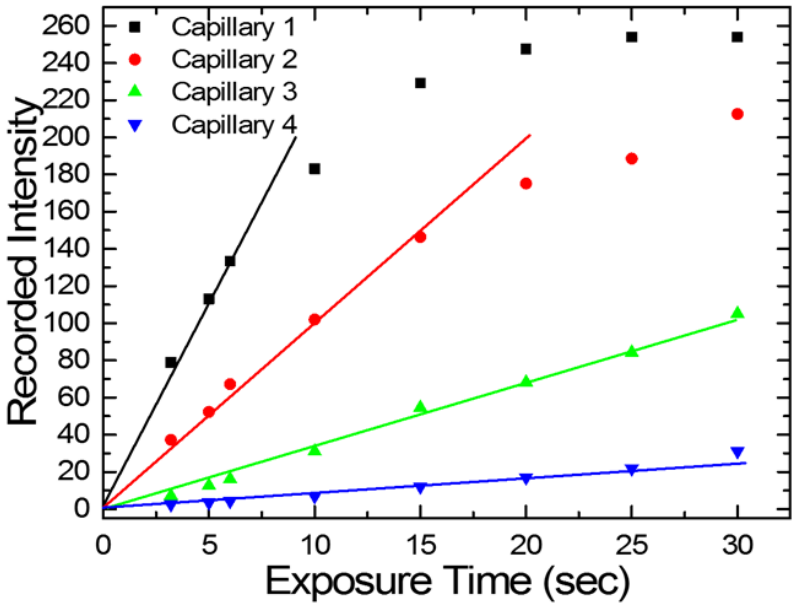

Figure 3.7. The response of the CMOS sensor to different light intensities. Calibration data points show the CMOS sensor in Canon 80D camera has a good response linearity when integrated light intensity is not close to saturation (<160 out of 254). For readings below 160, the recorded light intensity is mostly proportional to exposure time.

In our experiment, we utilized the double-exposure method, in which the emission intensity was recorded with 5 seconds of exposure followed by 30 seconds of exposure. Since the emitting light intensity from the substrate remains stable over a few minutes (which is guaranteed by the manufacturer and validated by our own experiments), the intensity counts can be converted between the two exposures using a factor of 6. The two insets in Fig. 3.8(A) show the response

curves for lower (0.03 – 10 ng/ml) and higher (10 – 3000 ng/ml) CK-MB concentration ranges with the exposure time of 30 seconds and 5 seconds, respectively. The whole response curve can be established in Fig. 3.8(A) by combining these two curves after adjusting the 30-second intensity to that for 5-second exposure. Using this combined response curve as the calibration curve and the double exposure method, the CK-MB concentration in 8 unknown samples were measured and plotted in Fig. 3.8(B). Our results show that the linear dynamic range for CK-MB can easily be extended by around 10-fold while maintaining a good accuracy.

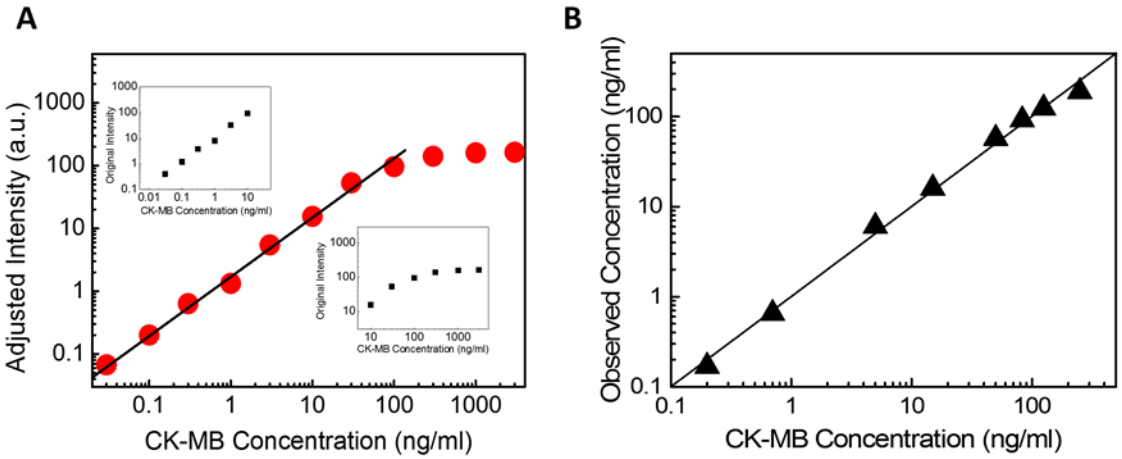

Figure 3.8. Extending the dynamic range. (A). Combined CK-MB response curve generated with the double-exposure method (measured in buffer solution). It is adjusted to 5-second exposure time. The dynamic range was extended from less than three orders of magnitude to approximately four orders of magnitude (0.03 – 200 ng/ml). The solid curve is the linear fit in the log-log scale with a slope of 0.95. Left inset: CK-MB response curve in the low concentration range (0.03 – 10 ng/ml) with an exposure time of 30 seconds. Right inset: CK-MB response curve in the high concentration range (10 – 3000 ng/ml) with an exposure time of 5 seconds. (B). The measured CK-MB concentrations using the capillary based ELISA and the data in A as the calibration curve agree well with the expected value. The solid line indicates the ideal reading (i.e., slope=1) within the concentration range of 0.1 – 500 ng/ml).

3.5. Summary

In this work, we demonstrated the performance and applicability of a glass capillary based microfluidic ELISA technique. Our work significantly reduced the required assay time (to 1/8 – 1/12 of traditional microplate-based ELISA, there's still room for further optimization) and sample volume (to 1/5 of microplate-based ELISA) while maintaining the excellent sensitivity and good repeatability of the chemiluminescent microplate-based ELISA. When utilizing the double exposure approach, the dynamic range can be increased 10-fold.

Our work provides a powerful tool to a broad range of clinical and research/development laboratorial applications. Its short assay time and large dynamic range will enable rapid quantification of the serum level of clinically important biomarkers such as C-reactive protein (CRP), troponin I, troponin T and glial fibrillary acidic protein (GFAP), thus benefitting the diagnosis and prognosis of rapid-developing diseases such as sepsis, acute organ rejection, myocardial infarction and traumatic brain injury. In addition to clinical applications, our small sample volumes can help save precious biological samples for fundamental biological researches (such as mouse's tail vein blood and mouse's cerebrospinal fluid) and avoid the necessity of sample dilution, thus reducing the error caused by pipetting.

However, we noticed this microfluidic ELISA prototype is still immature. It relies on a commercial SLR camera for taking measurements, which made the detection system relatively bulky. In addition, the distance between the camera and capillary reactors was still too far. Further miniaturization and customization of the imaging system are needed to make the device more practically viable.

3.6. Reference

1. H. Matsumoto, S. Shinzaki, M. Narisada, S. Kawamoto, K. Kuwamoto, K. Moriwaki, F. Kanke, S. Satomura, T. Kumada and E. Miyoshi, *Clin. Chem. Lab. Med*, 2010, **48**, 505.
2. R. M. Lequin, *Clin. Chem.*, 2005, **51**, 2415-2418.
3. E. Engvall and P. Perlmann, *Immunochemistry*, 1971, **8**, 871-874.
4. E. Eteshola and D. Leckband, *Sens Actuators B Chem.*, 2001, **72**, 129-133.
5. M. Herrmann, E. Roy, T. Veres and M. Tabrizian, *Lab Chip*, 2007, **7**, 1546-1552.
6. T. Wang, M. Zhang, D. D. Dreher and Y. Zeng, *Lab Chip*, 2013, **13**, 4190-4197.
7. J. Kai, A. Puntambekar, N. Santiago, S. H. Lee, D. W. Sehy, V. Moore, J. Han and C. H. Ahn, *Lab Chip*, 2012, **12**, 4257-4262.
8. B. S. Lee, J.-N. Lee, J.-M. Park, J.-G. Lee, S. Kim, Y.-K. Cho and C. Ko, *Lab Chip*, 2009, **9**, 1548-1555.
9. R. Gorkin, J. Park, J. Siegrist, M. Amasia, B. S. Lee, J.-M. Park, J. Kim, H. Kim, M. Madou and Y.-K. Cho, *Lab Chip*, 2010, **10**, 1758-1773.
10. B. S. Lee, Y. U. Lee, H.-S. Kim, T.-H. Kim, J. Park, J.-G. Lee, J. Kim, H. Kim, W. G. Lee and Y.-K. Cho, *Lab Chip*, 2011, **11**, 70-78.
11. M. Garcia, J. Orozco, M. Guix, W. Gao, S. Sattayasamitsathit, A. Escarpa, A. Merkoci and J. Wang, *Nanoscale*, 2013, **5**, 1325-1331.
12. M. Herrmann, T. Veres and M. Tabrizian, *Lab Chip*, 2006, **6**, 555-560.
13. T. Ohashi, K. Mawatari, K. Sato, M. Tokeshi and T. Kitamori, *Lab Chip*, 2009, **9**, 991-995.
14. X. Weng, G. Gaur and S. Neethirajan, *Biosensors (Basel)*, 2016, **6**, 24.
15. S. Wang, L. Ge, X. Song, J. Yu, S. Ge, J. Huang and F. Zeng, *Biosens. Bioelectron.*, 2012, **31**, 212-218.
16. E. Tsutsumi, T. G. Henares, S.-i. Funano, K. Kawamura, T. Endo and H. Hisamoto, *Anal. Sci.*, 2012, **28**, 51-51.
17. T. G. Henares, E. Tsutsumi, H. Yoshimura, K. Kawamura, T. Yao and H. Hisamoto, *Sens Actuators B Chem.*, 2010, **149**, 319-324.
18. S.-i. Funano, M. Sugahara, T. G. Henares, K. Sueyoshi, T. Endo and H. Hisamoto, *Analyst*, 2015, **140**, 1459-1465.
19. S.-i. Funano, T. G. Henares, M. Kurata, K. Sueyoshi, T. Endo and H. Hisamoto, *Anal. Biochem*, 2013, **440**, 137-141.
20. W.-J. Kim, S. H. Hyun, H. Y. Cho, S. Byun, B. K. Kim, C. Huh, K. H. Chung and Y. J. Kim, *Sens Actuators B Chem.*, 2016, **233**, 281-288.
21. R. Huda, Daneshvari R. Solanki and M. Mathru, *Clin. Sci.*, 2004, **107**, 497-503.
22. A. N. Vgontzas, D. A. Papanicolaou, E. O. Bixler, A. Kales, K. Tyson and G. P. Chrousos, *J. Clin. Endocrinol. Metab.*, 1997, **82**, 1313-1316.

23. J. F. Saucedo, R. Mehran, G. Dangas, M. K. Hong, A. Lansky, K. M. Kent, L. F. Satler, A. D. Pichard, G. W. Stone and M. B. Leon, *J. Am. Coll. Cardiol.*, 2000, **35**, 1134-1141.

24. S. Fuchs, R. Kornowski, R. Mehran, A. J. Lansky, L. F. Satler, A. D. Pichard, K. M. Kent, C. E. Clark, G. W. Stone and M. B. Leon, *Am. J. Cardiol.*, 2000, **85**, 1077-1082.

Chapter 4

A Fast and Reproducible ELISA Laser Platform

4.1. Introductory Remarks

In this chapter, we will introduce another prototype of the optofluidic ELISA that was developed based on a previous ELISA laser technology and the microfluidic chemiluminescent technology (chapter 3). With this approach, highly sensitive IL-6 quantification (LLOD = 0.1 pg/mL) was achieved. Note that the materials in this chapter was published on *ACS Sensors* in 2019.

4.2. Motivations

Enzyme-linked immunosorbent assay (ELISA) is one of the most popular methods used for quantification of functional proteins in biological research and clinical diagnosis. Traditional ELISA is carried out in the wells of a microtiter plate (typically made from polystyrene)[1, 2]. However, the current sensing signal transduction mechanisms based on colorimetric[2], fluorescence[3, 4], or chemiluminescence measurement[5, 6] and the low surface-to-volume ratio (0.32 mm^{-1}) of reaction wells still limit the performance of ELISA, especially in terms of sensitivity (~10 pg/mL), dynamic range (~2-3 orders of magnitude), sample/reagent consumption (~100 μL per well), and assay time (~5 hours)[6, 7].

In recent years, optofluidic lasers as a new sensing transduction technique are being investigated for sensitive intra-cavity biochemical analysis such as DNA melting analysis[8, 9],

sulfide ion sensing[10], cellular analysis, and cancer diagnostics that based on nucleic acid staining[11-14]. The intrinsic characteristics of the optofluidic laser enable optical amplification of small analyte concentration differences present in the gain medium, thus achieving highly sensitive detection[15, 16]. Additionally, the optical cavity acts as an optical filter to significantly reduce the fluorescence background for a high signal-to-noise ratio. Previously, the optofluidic laser based on a glass microfluidic capillary sandwiched between two gold-coated mirrors has been employed in ELISA to detect a type of cytokine and inflammatory marker IL-6 (Interleukin-6)[17]. While a proof-of-the-concept optofluidic ELISA laser was demonstrated and high sensitivity was achieved, that optofluidic laser platform has a few drawbacks. First, due to the limitation in glass capillary fabrication, it is challenging to repetitively achieve nearly identical optical alignment conditions for the cavity, thus leading to batch-to-batch inconsistency in the cavity Q-factor among cavities, which ultimately causes low reproducibility and low reliability for ELISA laser measurement and limits the practical use of capillary-based ELISA laser systems. Moreover, since no surface modification was applied to the glass capillary ELISA reactors, the protein immobilization affinity was extremely low, resulting in a very long assay time (up to 7 hours for laser measurements and up to ~8 hours in total assay time)[6].

Here, we developed a novel, on-chip, optofluidic ELISA laser technique based on the Fabry–Pérot optofluidic laser platform. In this work, a chemically functionalized polymer substrate with high protein affinity was directly microfabricated on dielectric mirrors that can be processed in batches with high reproducibility. The mirrors were divided into two groups – top mirrors and bottom mirrors – according to specially designed microscale reaction well structures on them. By sandwiching a top and a bottom mirror together, a micro-reactor with a high surface-to-volume ratio was formed in a well-spaced FP cavity. In this scheme, the repeatability and reliability of FP

cavity mirror alignment and hence the ELISA laser measurement was drastically improved and the enzymatic fluorogenic reaction efficiency was significantly enhanced, resulting in a shortened assay time. With all these new designs, our ELISA laser technique is able to complete an assay within 1.5 hours (including 30 minutes for laser measurement) while maintaining a small sample volume, large dynamic range (~4 orders of magnitude), and high sensitivity (LOD ~100 fg/mL for IL-6).

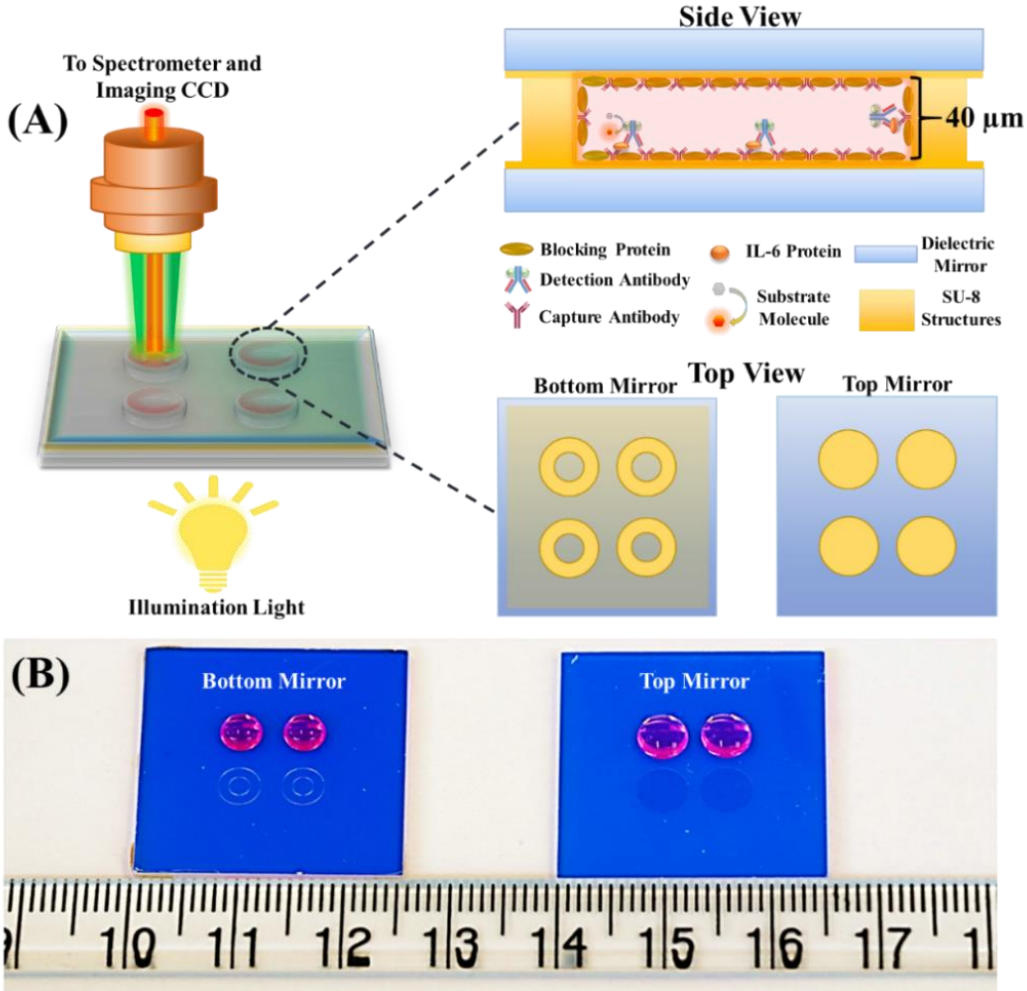

Figure 4.1. Layout, structures, and mechanism of the ELISA laser system. (A) Conceptual illustration of the ELISA laser experimental platform. The ELISA assay can be performed separately on the microfabricated bottom and top mirrors. Before taking measurements, the bottom and the top mirror will be sandwiched together and forms a high-Q Fabry–Pérot (FP) cavity. (B) Photos of the microfabricated bottom and top mirrors. The bottom mirror has four reaction wells, each of which had a diameter of 2 mm and a depth of ~42 µm. The top mirror also has four SU-8 flat pads that can be used for protein binding. They were fabricated at locations that can directly cover the wells on the bottom mirror.

4.3. Theoretical analysis

The rate of the enzymatic reaction in a typical ELISA assay, *v*, can be described by the Michaelis–Menten equation[18]:

$$v = \frac{d[P]}{dt} = k[E]\frac{[S]}{K_M+[S]}, \qquad (1)$$

where [P] is the enzymatic reaction product concentration, k is the enzymatic reaction rate, [E] is the enzyme concentration in an ELISA reactor, which is directly proportional to the quantity of immobilized analyte and detection antibody, [S] is the concentration of unreacted substrate molecule (as a function of time), and K_M is the Michaelis constant. Under our ELISA laser condition, the initial substrate concentration is orders of magnitude higher than K_M. During the initial stage of the reaction, the term $\frac{[S]}{K_M+[S]}$ can be approximated as unity. As a result, the product concentration [P] increases over time, t, with a rate linearly proportional to the enzyme concentration, *i.e.*[17],

$$[P] = k \cdot [E] \cdot t. \quad (2)$$

From a laser perspective, [P] represents the gain medium concentration in the ELISA laser. Initially, [P] is zero and no laser emission can be observed. However, [P] increases linearly with time based on Eq. (2) and the laser emission starts to emerge when the gain concentration reaches a threshold value, $[P]_{threshold}$. Under fixed laser conditions with a given cavity Q-factor and given pump intensity, $[P]_{threshold}$ is a constant. The laser onset time, τ, is defined as the reaction time needed for an ELISA laser to reach $[P]_{threshold}$, i.e.,

$$[E] \cdot = \frac{[P]_{threshold}}{k} = C. \quad (3)$$

Eq. (3) shows that the laser onset time is inversely proportional to the enzyme concentration and the overall reaction rate (defined as $1/\tau$), is directly proportional to the enzyme concentration. By measuring the laser onset time, the enzyme concentration and hence the analyte concentration can be obtained.

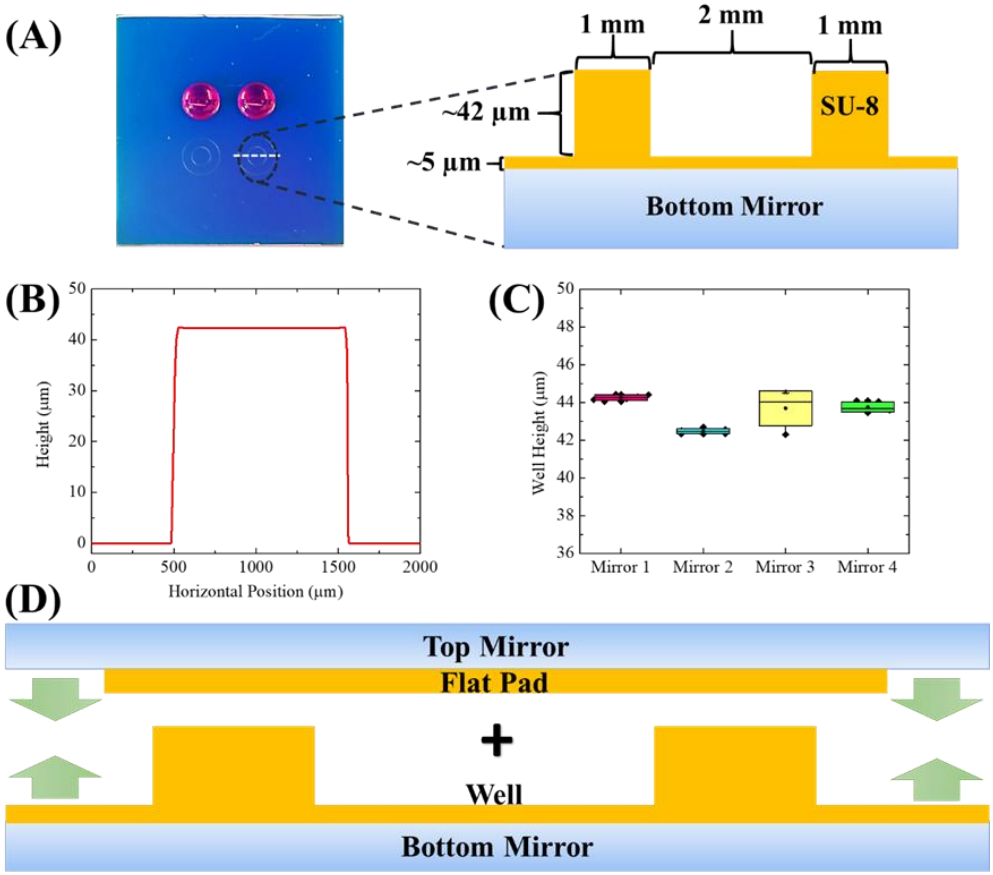

Figure 4.2. Bottom mirror fabrication. (A) Photo and illustration of the reaction well array on the bottom mirror. The wells were fabricated with SU-8 through multi-layer photolithography. The sub-figure on the left is a photo of the bottom mirror with four reaction wells on it. The red droplets in the photo indicate that liquid droplets can be stably placed inside the reaction wells during incubation steps. The sub-figure on the right is the cross-section of a reaction well along the position marked by the white dashed line in the left sub-figure. A typical reaction well had a 5 µm thick bottom layer and an SU-8 wall of approximately 42 µm in height. (B) Cross-section of the wall of a reaction well measured by a stylus profilometer. (C) The wall height was highly consistent among different bottom mirrors. The black dots are the well height measured at 6 different locations on each mirror, showing that the wall height was within the range between 42 µm and 45 µm. (D) Illustration of the structure consisting of a pair of the well on the bottom mirror and flat pad on the top mirror. Four pairs of such wells and pads can be found on one set of mirrors.

4.4. Materials and Methods

4.4.1. FP cavity and microwell fabrication

FP cavities with integrated reaction wells were used to provide optical feedback for the ELISA laser. FP cavities were formed by sandwiching a top mirror and a bottom mirror. These mirrors were purchased from Evaporated Coatings Inc. (Willow Grove, PA, USA). They were designed to have high reflectivity (99.5% according to manufacturer's specifications) in the spectral range of 580–640 nm to provide optimal optical feedback and high transmission (>50%) in the spectral range of 520-540 nm to allow for external 532 nm laser excitation. The Q-factor of the FP cavity was on the order of 10^4 at a cavity length of 40 μm.

As illustrated in Figs. 4.1 and 4.2, the SU-8 reaction well structures for the ELISA laser experiment were fabricated on the mirrors by standard soft-lithography based on a method developed previously[13]. Two masks were used to fabricate the bottom piece with reaction wells and the top piece with flat pads, respectively. The mirrors were first plasma cleaned and dehydrated at 175 ℃ for 15 minutes. For the bottom piece, a 5 μm thick SU-8 2005 was first spin-coated on the mirror surface for better adhesion of successive SU-8 layers. This thin SU-8 adhesion layer was flood exposed and developed before a ~42 μm thick SU-8 2010 layer was added on top. The mask containing microwells was used to expose the 42 μm SU-8 2010 layer (the height of the well is adjustable between 10-50 μm, depending on the fabrication protocols). After post-exposure baking, the bottom mirror was developed and rinsed with isopropyl alcohol (IPA) and deionized (DI) water. The illustration for bottom mirror fabrication and the corresponding well structure can be found in Fig. 4.2 (A)-(B). The wells such made had a diameter of 2 mm and a depth of ~42 μm. The microfabricated bottom mirrors and wells have high intra- and inter-mirror consistency (see Fig. 4.2(C)).

For the top mirror, a 5 μm SU-8 2005 layer was spin-coated on the substrate mirror, exposed with the mask containing the flat pad pattern, developed, and cleaned. Since the thermal conductivity of the glass-based substrate is lower than a standard silicon wafer, we found that elongated baking time and buffered cool down process would promote the adhesion of the SU-8 structure to the mirror. The photos of the microfabricated top and bottom mirrors can be found in Fig. 4.1(B). The microfabrication of both the top and the bottom mirrors can be processed in batches, with high reproducibility. In the current work, up to 10 pieces of the top and bottom mirrors can be fabricated in each batch. Both the top and the bottom mirrors can be reused after the ELISA laser reactions and measurements. The SU-8 structures can be removed with stainless steel blades. The mirrors were then sequentially rinsed with acetone, IPA, and DI water before starting the next round of SU-8 fabrication. The mirrors were reused 6 times without significant defects.

4.4.2. Top mirror silanization

SU-8 naturally has a medium-level affinity toward proteins[19]. In order to achieve optimal sensitivity (maximum protein affinity), we performed surface silanization to the microfabricated SU-8 structures on the top mirrors through the vapor phase deposition method[20]. The reagent used for surface silanization, 3-APTES ((3-Aminopropyl)triethoxysilane), was purchased from Sigma-Aldrich (440140-100ML). As illustrated in Fig. 4.3(A), the silanization process has two steps: (1) Treatment with air plasma for 30 seconds in a plasma etching machine for hydroxylation. (2) Vapor phase 3-APTES deposition, which was carried out in a vacuum reactor with five drops of liquid 3-ATPES (~100 μL) at 60 ^{o}C. The deposition process lasted for three hours in a constant temperature oven. After the silanization treatment, both the SU-8 regions and the glass regions on the top mirror were coated with a layer of 3-ATPES, which has a primary amino group on one end of the chain.

This amino group has a relatively high affinity for the free carboxyl groups found on aspartic acid, glutamic acid, and the C-terminus of proteins. The silanized top mirrors were ready to use after rinsing with DI water. Note that due to the relatively low chemical stability of SU-8 2010 used for reaction wells on the bottom mirror (*i.e.*, SU-8 2010 structures will be damaged during the vapor phase 3-ATPES deposition at elevated temperature), the bottom mirror was not silanized.

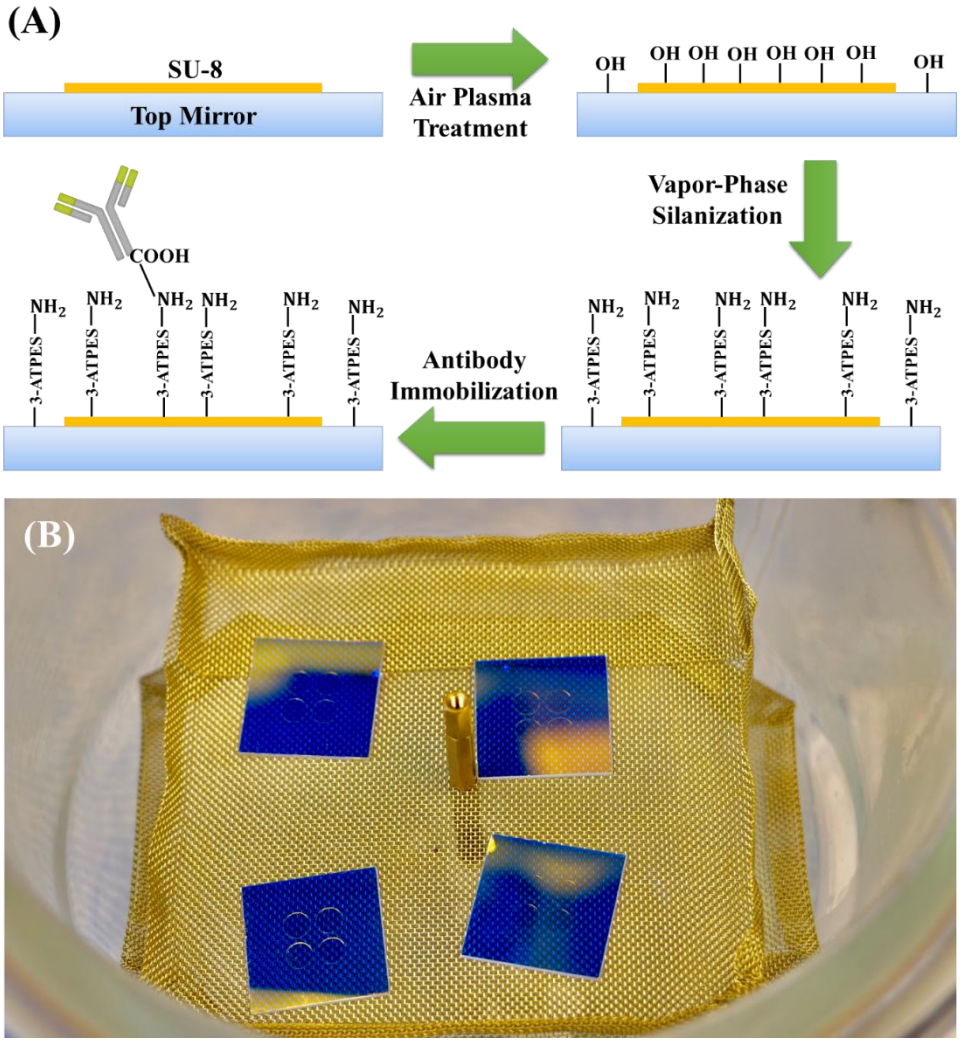

Figure 4.3. Top mirror silanization. (A) Illustration of functionalization for the top mirror. The top mirror was first treated with air plasma to generate hydroxyl groups on the surface. Then it was silanized with 3-ATPES through vapor-phase deposition at 60 ºC before incubation with monoclonal antibodies for capture antibody immobilization. The 3-ATPES layer has a primary amino group on the free-end, which is reactive with the free carboxyl group found on aspartic acid, glutamic acid, and the C-terminus of a protein. (B) The vapor phase silanization of the top mirrors can also be processed in batches with a metal steamer. Up to 10 pieces the top mirrors can be simutaneously silanized in each batch.

As presented in Fig. 4.3(B), the vapor phase silanization of the top mirrors can also be processed in batches with a metal steamer. Up to 10 pieces the top mirrors can be simultaneously silanized in each batch.

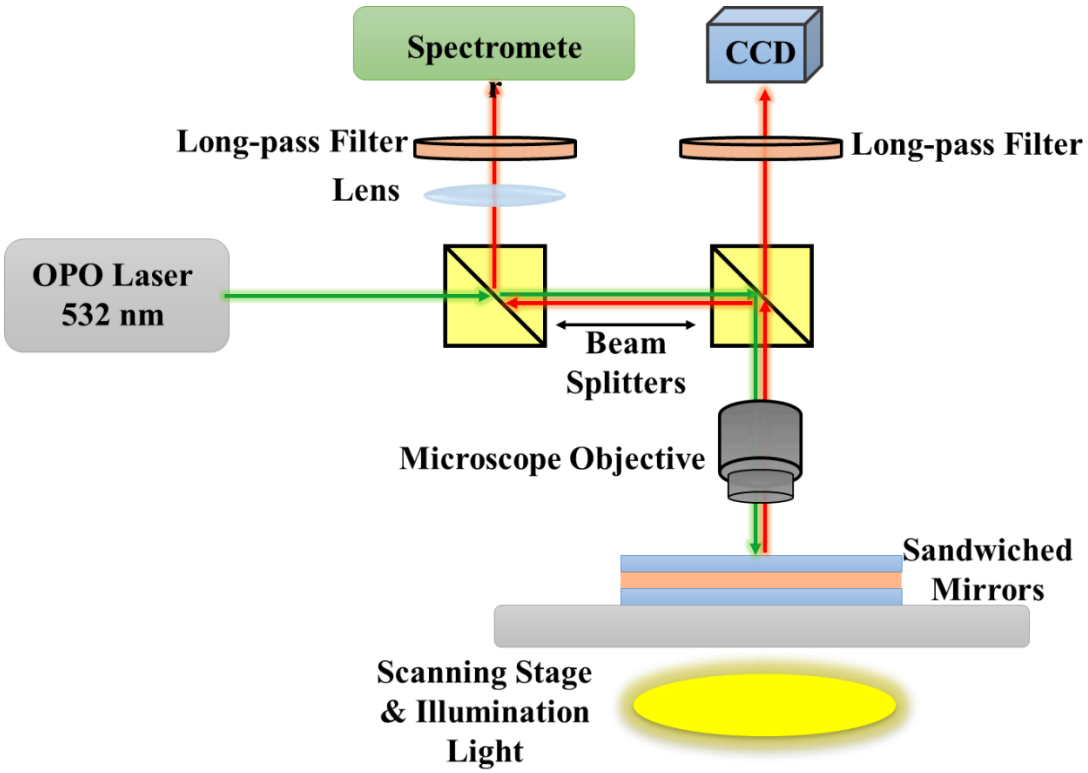

Figure 4.4. Schematic of the optical setup for the ELISA laser experiments, the emission laser signals were collected with the spectrometer. The imaging CCD was used to facilitate focusing procedures and aid to locate designated regions for laser examinations.

4.4.3. Optical system setup

A typical confocal microscopy setup was used to excite the sample and collect emission light from the FP cavity. A schematic of our optical setup can be found in Fig. 4.4. A pulsed optical parametric oscillator (OPO) laser (pulse width: 5 ns, repetition rate: 20 Hz) at 532 nm was used as the excitation source. In ELISA laser measurements, the pump intensity was fixed at approximately 210 μJ/mm^2. The emission light was collected through the same lens and sent to a

spectrometer (Horiba iHR550, spectral resolution ~0.2 nm) for analysis. An imaging CCD was used to facilitate focusing procedures and locate designated regions for laser examinations.

4.4.4. ELISA reagents

The chemifluorescent substrate (QuantaRed Enhanced Chemifluorescent HRP Substrate Kit) was purchased from Thermo Fisher Scientific (15159). For IgG-HRP immobilization experiments, goat anti-mouse IgG (H+L) Superclonal™ antibody with HRP conjugation was purchased from Thermo Fisher Scientific (A28177). For interleukin-6 (IL-6) ELISA laser experiments, human IL-6 DuoSet ELISA Kit (DY206), ELISA plate-coating buffer (1× PBS, DY006), wash buffer (WA126), and reagent diluent (10% BSA in 10× PBS, DY995) were purchased from R&D Systems. The SuperBlock (PBS) Blocking Buffer (37515) and streptavidin poly-HRP (21140) was purchased from Thermo Fisher Scientific. Heat deactivated human serum (H3667) was purchased from MilliporeSigma.

The stock solutions of the capture antibody, detection antibody, and human IL-6 standard were prepared according to the procedures described in the kits' user manuals. The working solution of wash buffer and reagent diluent were diluted with Milli-Q water (R = 18.2 Ω) to achieve 1× working concentration. The 1× reagent dilute solution (1% BSA in PBS) and SuperBlock Blocking Buffer were both used as the blocking buffers. The capture antibody stock solution was diluted with PBS buffer and finally achieved a concentration of 24 μg/mL (working concentration). The working solution of the biotinylated detection antibody was prepared by diluting the stock solution with the 1× reagent diluent and finally achieved an antibody concentration of 0.5 μg/mL (the detection antibody was biotinylated by the manufacturer). The concentrated human IL-6 standard was diluted to the desired concentration with the 1× reagent diluent. Streptavidin poly-HRP was employed to maximize ELISA signal[21]. The working solution of streptavidin poly-HRP

was produced by diluting the stock solution 1000 times in a customized dilution buffer (0.01% Tween 20 in 1% BSA).

4.4.5. IgG-HRP binding assay on mirror

First, 15 μL of the HRP-conjugated IgG antibody solution (with various concentrations) was added to the designated reaction sites on the bottom and top mirrors (reaction wells on the bottom mirror and flat pads on the top mirror). IgG-HRP molecules contained in the solution were immobilized on the reaction sites through 90 minutes of incubation. Then the reaction sites were rinsed with an excessive amount of washing buffer. A few polystyrene beads of 30 μm in diameter (purchased from Sigma-Aldrich (84135-5ML-F)) were placed into the reaction wells on the bottom mirror. Finally, 10 μL of QuantaRed fluorescent ELISA substrate solution was added into the reaction wells on the bottom mirror (no substrate was added to the pads on the top mirror). Then the top mirror was placed up-side-down on top of the bottom mirror immediately so that the flat pads on the top mirror, which serve as caps of the ELISA reactors see Fig. 4.2(D) for illustration), cover the reaction wells on the bottom mirror. The sandwiched mirrors (along with the substrate solution between them) were then placed on the translation stage for measurement with the optical setup. An illustration for the structure of a pair of sandwiched mirrors can be found in Fig. 4.2(D).

4.4.6. IL-6 ELISA on the mirrors

Before adding analyte (sample) solutions, capture antibodies were first immobilized on the designated reaction sites through 90 minutes of incubation. Then the reaction sites on the top and bottom mirrors were both sequentially incubated with 1× reagent diluent and SuperBlock Blocking Buffer for 30 minutes and 10 minutes. These steps were used to prevent non-specific protein binding on the SU-8 structures. Then the analyte solution (with different IL-6 concentrations) was added to the reaction sites and incubated for 30 minutes. After that, the detection antibody solution

was added to the reaction sites and incubated for another 20 minutes. Finally, the streptavidin poly-HRP solution was introduced to the reaction sites and incubated for an additional 10 minutes. At the beginning of all incubation steps, 15 μL of solution was added to each of the reaction sites on both the bottom and the top mirrors. To avoid contamination by residual reagents, at the end of all incubation steps, the remaining liquid on the mirrors was carefully and gently removed by placing water absorption tissues (KimWipes, Kimtech Science) on top of the reaction sites. Then the mirrors were rinsed with an excessive amount of washing buffer before a few polystyrene beads of 30 μm in diameter were placed into the reaction wells on the bottom mirror. Finally, 10 μL of substrates solution was added into the reaction wells on the bottom mirror (no liquid was added to the flat pads on the top mirror). Then the top mirror was placed up-side-down on top of the bottom mirror immediately. The sandwiched mirrors (along with the substrate solution between them) were then placed on the translation stage for measurement with the optical setup.

4.5. Results

As presented in Fig 4.1(A) and (B), in this work microfabricated SU-8 reaction wells and flat pads were designed to perform solid-phase immunoassay and ELISA laser detection. A typical ELISA laser reactor setup contains two pieces of dielectric mirrors, one serving as the bottom mirror and the other as the top mirror. Four reaction sites were microfabricated in SU-8 on homologous locations on both mirrors. For the bottom mirror, the reaction sites were designed to have shallow well structures (approximately 42 μm in depth and 2 mm in diameter). In contrast, the reaction sites for the top mirror were simply SU-8 flat pads. When sandwiching the two mirrors together, a hollow reactor with a high surface-to-volume ratio (52 mm^{-1}) formed between the aligned reaction sites.

4.5.1. Lateral optical confinement with polystyrene microbeads

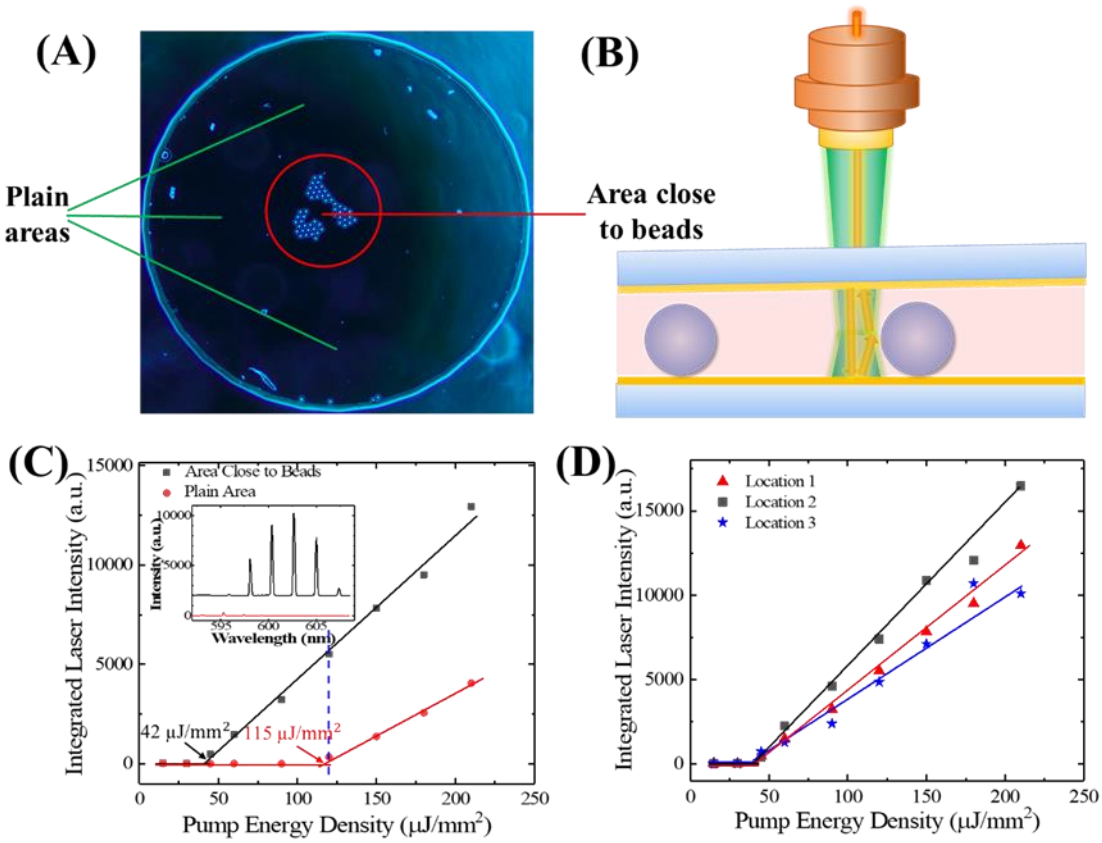

Figure 4.5. Demonstration of lateral optical confinement with polystyrene microbeads. (A) Photo of polystyrene microbeads in a reaction well. The circled area indicates the location close to microbeads. (B) Illustration of the optical confinement and Q-factor improvement with a polystyrene bead. The light can be reflected by the boundaries of the beads, resulting in a lateral confinement of the optical mode, thus increasing the cavity Q-factor. (C) Laser characteristics comparison between the areas with beads and far away from the beads (plain area). The solid lines are the linear fit above the lasing thresholds. The lasing threshold was significantly reduced at the location close to beads (42 μJ/mm^2 vs. 115 μJ/mm^2). (D) The lasing signals obtained at three different locations within the same well that were close to beads. Although the emission signals had different intensities, their thresholds were very close to each other (42 ± 3 μJ/mm^2).

We first investigated the optical characteristics of the FP ELISA laser cavity. As a non-crystal material, the borosilicate glass substrate that was used to fabricate dielectric mirrors has non-negligible elasticity under room temperature[22]. Due to the surface tension of water, when sandwiching the bottom and top mirrors together (with a proper amount of liquid in between), the inter-mirror distance at the center of the mirrors is slightly (~2-3 μm) shorter than the distance at

the edges of the mirrors. In such a pair of mirrors, the resulting FP cavity with the highest Q-factor is typically located in the central region of the mirrors (between the four pairs of reaction sites). In other words, the region of the top mirror that directly cover the ELISA reaction wells is slightly tilted, leading to a deteriorated and not-well-controlled Q-factor. To achieve an acceptable Q-factor (approximately on the order of 10^4) for ELISA laser detection under non-perfect alignment conditions, polystyrene microbeads were added into the reactors, as illustrated in Figs. 4.5(A) and (B)[23]. Due to the reflection effect at the boundary of a microbead, the lateral confinement in the lasing mode and significant improvement in the Q-factor can be achieved. This optical phenomenon is well explained in our recent publication[23].

The performance of the bead-incorporated ELISA laser reactor was evaluated through a simple experiment. Before taking measurements, a few polystyrene microbeads ($d \approx 30$ μm) were placed in each reaction well on the bottom mirror. Then, 10 μL of fully reacted (the enzymatic reaction reaches equilibrium and the fluorescent molecule reaches maximum concentration) fluorescent substrate (4 × recommended concentration) were added to the four wells on the bottom mirror. Then a top mirror was placed on top of the bottom mirror with up-side-down orientation (so the SU-8 structures on both mirrors touched each other). The laser emission from locations that were close to or far away from beads were then collected. As shown in Fig. 4.5(C), the laser signal differs significantly between the areas close to beads and the areas far away from beads. The lasing threshold was significantly reduced, from 115 μJ/mm^2 at locations far away from any beads to approximately 42 μJ/mm^2 at locations close to the beads. In addition, as shown in Fig. 4.5(D), the lasing thresholds for the locations filled with beads are nearly identical, despite different lasing intensities. Therefore, the ELISA laser measurement can be carried out at any location filled with beads, which make the experimental much easier and more consistent. For this reason, all data in

the following experiments were collected from the regions that were filled with beads. Note that the total volume of the beads is typically smaller than 0.5% of a well's total volume and thus does not significantly alter the enzymatic reaction rate. Finally, Fig. 4.6. shows the typical lasing spectrum, whose free spectral range is measured to be approximately 2.3 nm, which corresponds to a cavity length of approximately 55 μm, in good agreement with our laser cavity design (5 μm of SU-8 layers on both mirrors, 42 μm of ELISA micro reactor and 3 μm of water layer between the top and bottom mirror).

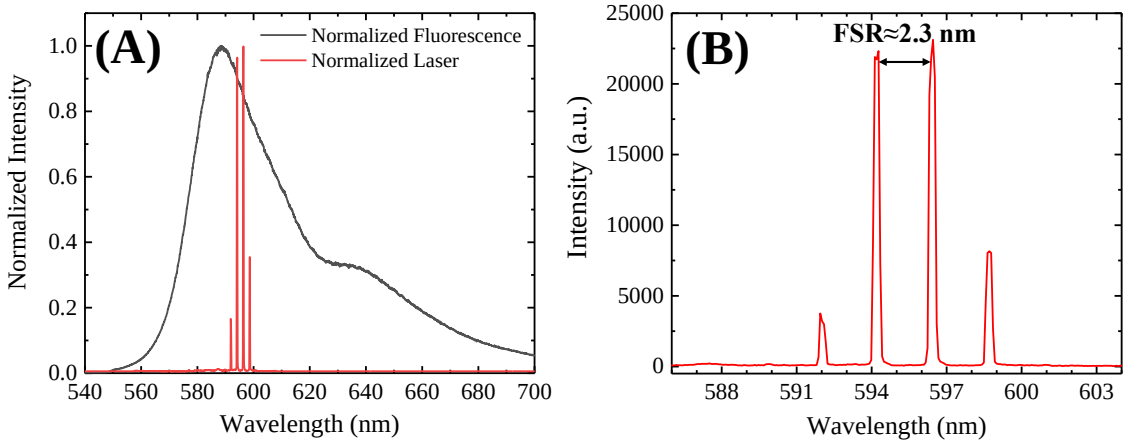

Figure 4.6. Lasing and fluorescent spectrums. (A) Comparison between the fluorescence spectrum and the laser spectrum. Both spectra were obtained at 4X recommended substrate concentration and normalized to their respective peak intensity. (B) Zoomed-in laser spectrum showing a free spectral range of approximately 2.3 nm, corresponding to a cavity length of approximately 55 μm, assuming the refractive index of the substrate liquid inside the cavity is 1.33 and the effective overall refractive index for the entire cavity is 1.38.

4.5.2. Substrate concentration optimization

The concentration of fluorescent substrate (i.e., Thermo Fisher's QuantaRed) was optimized by monitoring the corresponding ELISA laser threshold. Since the absolute concentration of the substrate was not provided by the vendor, we used only the relative concentration. In this test, the substrate was prepared at 4 ×, 2 ×, 1 × and 0.5 × recommended concentrations. Higher substrate concentrations are not suitable for ELISA detection because of

the strong non-specific auto-reaction. 0.5 μL of high concentration free HRP was added into the substrates to artificially generate a saturated (fully reacted) condition before adding the HRP-substrate samples into the reaction wells. The laser thresholds for these four concentrations were measured at regions close to microbeads inside the ELISA laser reactors.

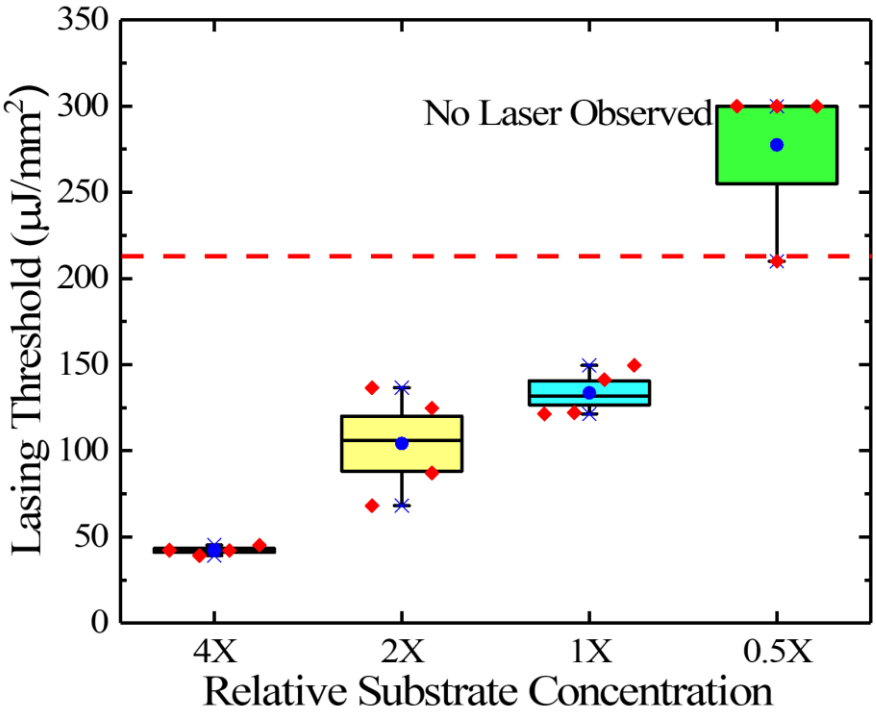

Figure 4.7. Lasing threshold for different substrate concentrations (fully reacted). All data were obtained at the locations close to the beads. The dashed red line represents the intensity, 210 μJ/mm^2, which was used as the pump for actual ELISA laser measurements. The red diamond dots represent the laser thresholds observed at different locations. For low substrate concentration (0.5X), almost no laser signal would be observed with the pump of 210 μJ/mm^2.

As shown in Fig. 4.7, although laser signals are observed for all substrate concentrations, the lasing threshold for the 4 × recommended substrate concentration appears to be the lowest and most reproducible. Furthermore, according to the 1 × concentration result, we can conclude that the lasing can be observed with 4 × substrate concentration when the reaction reaches ¼ saturation. Therefore, the 4 × recommended substrate concentration was selected as the experimental condition for all following ELISA laser experiments, as it meets the requirements for low non-

specific auto-fluorescence (concentration not high), relatively easy to generate laser emission (low lasing threshold), and no need to wait for full saturation (1/4 saturation) when pumped at 210 $\mu J/mm^2$.

4.5.3. IgG-HRP immobilization experiments

To examine the stability of protein immobilization and the reliability for performing actual ELISA tests with this setup, we conducted a simplified protein immobilization test, which is the IgG-HRP immobilization experiment. In this set of experiments, HRP-conjugated IgG solutions (IgG-HRP dissolved in 1 × PBS) with different concentrations were added into the microfabricated reaction wells on the bottom mirror and the flat pads on the top mirror. The detailed protocol can be found in "IgG-HRP binding assay on mirror" of the Materials and Methods section.

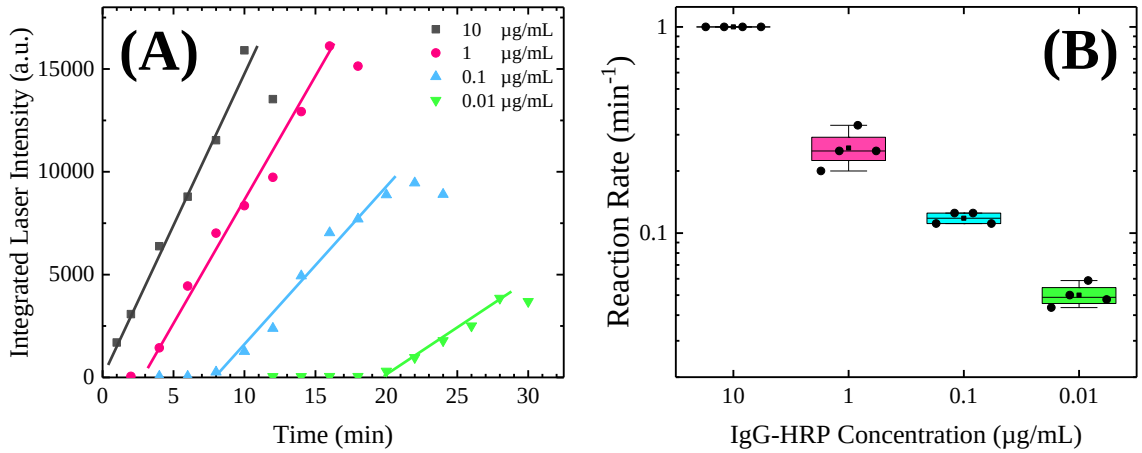

Figure 4.8. Results for IgG-HRP immobilization experiments. (A) The laser intensities vs time for four different IgG-HRP concentrations. The intensities are labeled as points with different colors. The solid lines are the linear about the threshold. An exemplary lasing spectrum are given in Fig. 4.9. (B) Reaction rates (defined as the inverse of the laser onset time) are measured for four different IgG-HRP concentrations.

After 90 minutes of incubation, a portion of the IgG-HRP proteins was immobilized on the microfabricated SU-8 structures through hydrophobic interaction (physical adsorption). After

adding QuantaRed ELISA substrate onto the wash buffer rinsed mirrors, the amount of immobilized IgG-HRP can be quantified through measuring the laser onset time (the reaction time used to generate the first laser emission.). The time counting started immediately after sandwiching the top and bottom mirrors. Based on the reasons described in the previous sub-chapters, 210 $\mu J/mm^2$ was selected to be the intensity of the pump laser and polystyrene microbeads were used to facilitate the generation of laser emission.

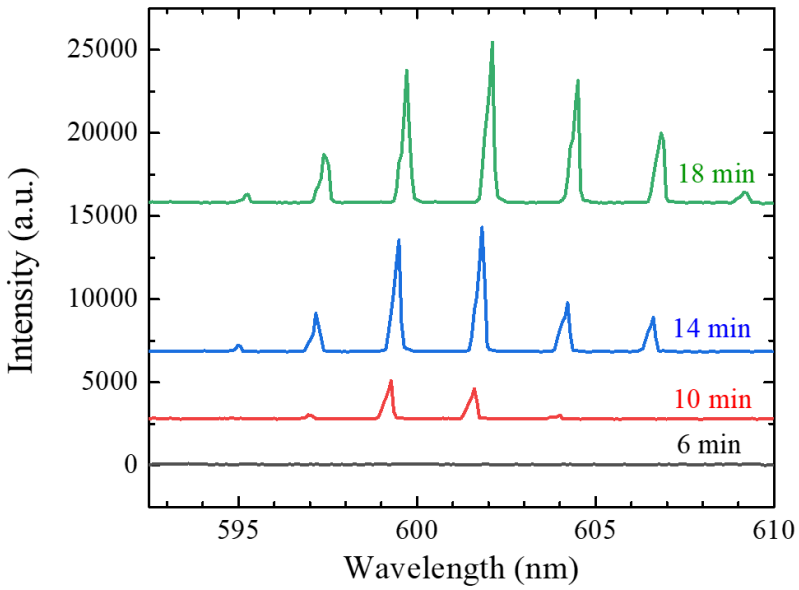

Figure 4.9. An example of the laser signal obtained at different time points in the IgG-HRP immobilization experiment (IgG-HRP concentration: 0.1 μg/mL). As the result of enzymatic reaction, the signal intensity increases over time. A slight red shift in the lasing peaks is caused by the increase in the concentration of fluorescent molecules during the enzymatic reaction.

The result presented in Fig. 4.8 (A) shows the change in laser emission intensities over time for four different IgG-HRP concentrations over time. The intensities for each IgG-HRP concentration were presented with a time interval of two minutes, at a single location. As the result shown, the laser signal emerges at different time points for different IgG-HRP concentrations. For IgG-HRP concentration at 10 μg/mL, the laser signal appears at the first minute (almost instantaneously) after adding substrate. For the other three IgG-HPR concentrations (1, 0.1, and

0.01 μg/mL), the laser signal first appears at 4, 8, and 20 minutes, respectively. As described in the theoretical analysis section, the difference in the laser onset time was caused by the difference in the quantity of HRP (as a subunit of the IgG-HRP molecule) that was immobilized on the mirrors. The wells with a higher amount of immobilized HRP will have a faster enzymatic reaction rate (positively correlation), thus requires a shorter time to reach the threshold fluorescent molecule concentration for laser emission. The corresponding overall reaction rate (defined as the inverse of the laser onset time, $1/\tau$) for all four IgG-HRP concentrations can be found in Fig. 4.8(B). This set of experiments clearly demonstrate the ELISA laser is able to reliably distinguish IgG-HRP of different concentrations.

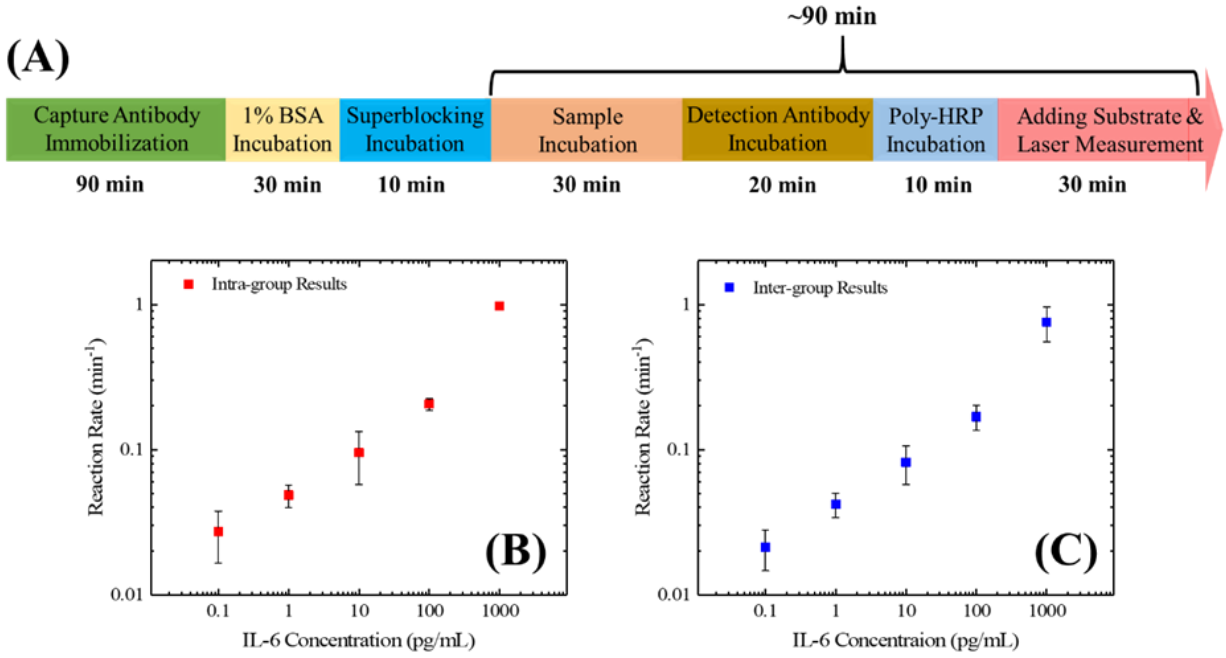

Figure 4.10. IL-6 ELISA laser results. (A) A brief protocol for human IL-6 ELISA with our on-chip ELISA laser system (B) Intra-group results for the IL-6 ELISA laser experiment. The reaction rate is defined as the inverse of the laser onset time. The error bars are the standard deviations measured with three reaction wells on the same set of mirrors. (C) Inter-group results for the IL-6 ELISA laser experiments. The data point on each concentration represent the overall averaged reaction rates that were measured from three sets of mirrors. The error bars are the standard deviations measured with three different sets of mirrors.

4.5.4. IL-6 ELISA laser experiments

The feasibility for performing real-world quantification of a specific protein with this setup was evaluated with a human IL-6 ELISA laser assay. Same as any other sandwich ELISA assay, the human IL-6 sandwich ELISA employs two antibodies that can recognize different epitopes on a single analyte (in our case, human IL-6) molecule. As illustrated in Fig. 4.10(A), in this experiment, the capture antibody was first immobilized (through physical adsorption) on the reaction sites on both the top and the bottom mirrors. Then, after blocking with 1% BSA and SuperBlock Blocking Buffer, the solution containing analyte was added to and incubated with the mirrors. After the analyte was immobilized by the capture antibody, the biotinylated detection antibody solution and streptavidin poly-HRP solution was added and incubated with the reaction sites on the mirrors sequentially. One step of rinsing with 0.05% Tween-20 was performed between each of the incubation steps. By the end of the entire immunoassay, both the top and the bottom mirrors were rinsed three times with ELISA wash buffer (0.05% Tween-20), then, tens of polystyrene microbeads (typically between 25-60 beads per well) were placed into the micro reaction-wells on the bottom mirrors (by dipping with dry pipet tips). Afterward, 10 μL of substrates solution (4× recommended concentration) was added into the reaction wells on the bottom mirror. Finally, the top mirror was placed on top of the bottom mirror with the substrate solution filled up all gaps in-between. Then the sandwiched ELISA laser cavity was taken to the optical setup for laser measurements. The total assay time was approximately 90 minutes, which was still considerably shorter than traditional plate-based ELISA (about 6 hours)[6].

In this experiment, the laser onset time in each reaction well was first recorded and then converted to reaction rates (inverse of the laser onset time). Fig. 4.10(B) presents the intra-group results for five different IL-6 concentrations (0.1, 1, 10, 100, 1000 pg/mL, respectively). The data

was collected from the wells on one set of mirrors, for each concentration. For all these five concentrations, the averaged reaction rate that was measured and calculated by subtracting the background reaction rate of 0.0246 min^{-1} from the background (*i.e.*, 1% BSA in PBS serves as the blank sample, and the averaged laser onset time was 40.6 minutes). The inter-group measurements by using multiple sets of mirrors are given in Fig. 4.10(C) (three sets of mirrors for each concentration), showing that the sensing capability is reproducible across different sets of devices that were fabricated separately, which was significant improvement over our previous ELISA laser prototype.

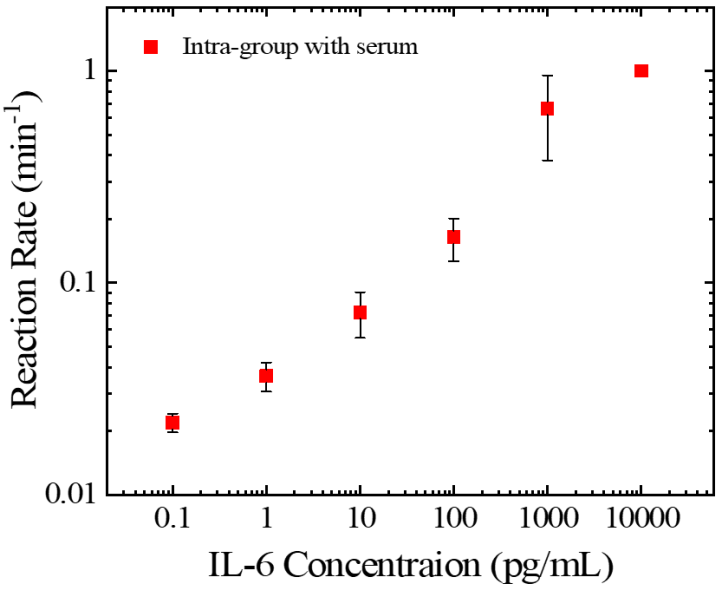

Figure 4.11. IL-6 ELISA laser results with human serum as analyte solvent. The error bars are the standard deviations measured with three reaction wells on the same set of mirrors. No laser was observed with the blank control.

To validate the ability of the ELISA laser to analyze complex samples, we also performed a set of experiments with IL-6 in human sera. The procedures were exactly the same as previously described, except that human serum was used. Fig. 4.11 presents the results for six different IL-6 concentrations that were spiked into human serum (0.1, 1, 10, 100, 1000, and 10000 pg/mL, respectively). In this set of experiments, no laser was observed with the blank control (i.e., serum with no spiked IL-6) over the 60 minutes. Therefore, no background reaction rate was subtracted.

Similar to the results obtained with BSA buffer, the reaction rates for different concentrations generally follow a linear trend in the log-log scale between IL-6 concentration of 0.1 and 1000 pg/ml, which indicates our technique has a dynamic range of four orders of magnitude and a limit of detection (LOD) of 0.1 pg/mL. The IL-6 ELISA results shown above indicate while the ELISA laser technique still needs refinement, it has great potential to achieve high sensitivity (0.1 pg/mL) in a short amount of time (<1.5 hours) with a small sample volume (30 μL) and a large dynamic range (4 orders of magnitude).

4.6. Discussion and conclusion

In this work, we have successfully developed a new generation of ELISA laser platform able to carry out ultra-sensitive quantification for specific proteins on a wide dynamic range in a short amount of time. This achievement is facilitated by the mass-production possibility of the micro-reaction wells on-chip, SU-8 micro-lithography technique, surface chemical modification, and lateral optical confinement. The new platform has significantly improved reproducibility over the previous ELISA laser prototypes and takes the ELISA laser a step closer towards real-world applications. Since sandwich ELISA itself is a widely used technology for analyte quantification, our technology should have similar or more potential application scenarios than other optofluidic immunoassays (e.g., turbidimetric immunoassays)[24]. The micro-reaction wells also have the potential to be used as the reactors in liquid-phase laser-based biosensing experiments[25].

However, due to the uncertainties in reactor fabrication and manual ELISA operations, the repeatability and inter/intra-assay variances of this ELISA laser technology is still not as good as the microfluidic chemiluminescent ELISA prototype that was described in Chapter 3. For this reason, the microfluidic chemiluminescent ELISA prototype will be used as the cornerstone for future development of optofluidic ELISA.

4.7. References

1. E. Vanmechelen, H. Vanderstichele, P. Davidsson, E. Van Kerschaver, B. Van Der Perre, M. Sjögren, N. Andreasen and K. Blennow, *Neurosci. Lett.*, 2000, **285**, 49-52.
2. J. P. O'Callaghan, *Neurotoxicol. Teratol.*, 1991, **13**, 275-281.
3. A. Konijn, R. Levy, G. Link and C. Hershko, *J. Immunol. Methods.*, 1982, **54**, 297-307.
4. J. E. Noble, L. Wang, E. Cerasoli, A. E. Knight, R. A. Porter, E. Gray, C. Howe, E. Hannes, P. Corbisier and J. Wang, *Clin. Chem. Lab. Med.*, 2008, **46**, 1033-1045.
5. S. Zhang, Z. Zhang, W. Shi, S. A. Eremin and J. Shen, *J. Agric. Food Chem.*, 2006, **54**, 5718-5722.
6. X. Tan, M. K. Khaing Oo, Y. Gong, Y. Li, H. Zhu and X. Fan, *Analyst*, 2017, **142**, 2378-2385.
7. X. Tan, A. David, J. Day, H. Tang, E. R. Dixon, H. Zhu, Y.-C. Chen, M. K. Khaing Oo, A. Shikanov and X. Fan, *ACS Sens.*, 2018, **3**, 2327-2334.
8. M. Hou, X. Liang, T. Zhang, C. Qiu, J. Chen, S. Liu, W. Wang and X. Fan, *ACS Sens.*, 2018, **3**, 1750-1755.
9. W. Lee, Q. Chen, X. Fan and D. K. Yoon, *Lab Chip*, 2016, **16**, 4770-4776.
10. C. Gong, Y. Gong, M. K. K. Oo, Y. Wu, Y. Rao, X. Tan and X. Fan, *Biosens. Bioelectron.*, 2017, **96**, 351-357.
11. Y.-C. Chen, X. Tan, Q. Sun, Q. Chen, W. Wang and X. Fan, *Nat. Biomed. Eng.*, 2017, **1**, 724.
12. Y.-C. Chen, Q. Chen, X. Wu, X. Tan, J. Wang and X. Fan, *Lab Chip*, 2018, **18**, 1057-1065.
13. Q. Chen, Y.-C. Chen, Z. Zhang, B. Wu, R. Coleman and X. Fan, *Lab Chip*, 2017, **17**, 2814-2820.
14. Y.-C. Chen, Q. Chen, X. Tan, G. Chen, I. Bergin, M. N. Aslam and X. Fan, *Biomed. Opt. Express*, 2019, **10**, 838-854.
15. X. Fan, I. M. White, S. I. Shopova, H. Zhu, J. D. Suter and Y. Sun, *Anal. Chim. Acta*, 2008, **620**, 8-26.
16. X. Fan and I. M. White, *Nat. Photonics*, 2011, **5**, 591.
17. X. Wu, M. K. Khaing Oo, K. Reddy, Q. Chen, Y. Sun and X. Fan, *Nat. Commun.*, 2014, **5**, 4779.
18. A. Cornish-Bowden and A. Cornish-Bowden, *Fundamentals of enzyme kinetics*, Wiley-Blackwell Weinheim, Germany, 2012.
19. G. Blagoi, S. Keller, A. Johansson, A. Boisen and M. Dufva, *Appl. Surf. Sci.*, 2008, **255**, 2896-2902.
20. S. H. North, E. H. Lock, C. J. Cooper, J. B. Franek, C. R. Taitt and S. G. Walton, *ACS Appl. Mater. Interfaces*, 2010, **2**, 2884-2891.
21. I. Ojeda, M. Moreno-Guzmán, A. González-Cortés, P. Yáñez-Sedeño and J. Pingarrón, *Anal. Bioanal. Chem.*, 2014, **406**, 6363-6371.
22. N. P. Bansal and R. H. Doremus, *Handbook of glass properties*, Elsevier, 2013.
23. X. Wu, Q. Chen, Y. Wang, X. Tan and X. Fan, *ACS Photonics*, 2019, DOI: 10.1021/acsphotonics.9b00726.
24. X. Yang, W. Shu, Y. Wang, Y. Gong, C. Gong, Q. Chen, X. Tan, G.-D. Peng, X. Fan and Y.-J. Rao, *Biosens. Bioelectron.*, 2019, **131**, 60-66.
25. J. Wu, M. Fan, G. Deng, C. Gong, K. Chen, J. Luo, K. S. Chiang, Y.-J. Rao and Y. Gong, *Sens. Actuator B-Chem.*, 2019, **298**, 126830.

26. A. Di Iorio, L. Ferrucci, E. Sparvieri, A. Cherubini, S. Volpato, A. Corsi, M. Bonafè, C. Franceschi, G. Abate and R. Paganelli, *Cytokine*, 2003, **22**, 198-205.
27. I. F. Amado, J. Berges, R. J. Luther, M.-P. Mailhé, S. Garcia, A. Bandeira, C. Weaver, A. Liston and A. A. Freitas, *J. Exp. Med.*, 2013, **210**, 2707-2720.

Chapter 5

Rapid Mouse FSH Quantification and Estrus Cycle Analysis Using an Automated Microfluidic Chemiluminescent ELISA System

5.1. Introductory remarks

In this chapter, we will introduce the design and development of an automated microfluidic chemiluminescent ELISA system (along with the disposal sensor array) based on the manually operated prototype (described in chapter 3). We also applied this technology to the detection and quantification of a pituitary hormone, follicle stimulating hormone (FSH), which plays a critical role in female reproductive development and homeostasis. The performance of this technology was evaluated with blood samples collected from ovariectomized animals and animals with re-implanted ovarian tissues, which restored ovarian endocrine function and correlated with estrus cycle analysis study. Note that the materials in this chapter was published on *ACS Sensors* in 2018.

5.2. Motivations

Follicle stimulating hormone (FSH) is one of the two gonadotropic hormones (along with Luteinizing Hormone, LH) that is released by the anterior lobe of pituitary gland[1]. It plays a key role in female reproductive development and homeostasis through stimulating the maturation of germ cells and initiating the follicular growth[2-3]. The blood/serum concentration of FSH is an important marker for reporting the function of the hypothalamic–pituitary–gonadal axis (HPG

axis)[4-5], the stages of puberty and stages in estrus cycle in mammals, as well as the stages in human menstruation cycle[6]. In each estrus cycle, the concentration of FSH in circulating blood can change dramatically in a very short period of time[7-8]. In order to rapidly monitor the FSH concentrations in such events, a fast, reliable, sensitive, and on-site measurement with small sample consumption is highly desired.

The endocrine system of a mouse has been extensively studied for several decades and serves as one of the well-established model animals. The quantitative measurements of the serum FSH concentration is an important component of these studies. Currently, the blood/serum concentration of mouse FSH (mFSH) is most commonly quantified via radioimmunoassay (RIA). The antibody used in RIA (guinea pig polyclonal antibody in the form of antiserum) is designed for competitive immunoassay, thus having very good specificity. Consequently, RIA has been viewed as the "gold standard" for quantifying FSH concentration in serum[9]. However, RIA assay for quantification of mFSH via RIA presents several challenges, such as relatively low sensitivity, large measurement uncertainty and a small dynamic range (which varies around 2–60 ng/mL), and requires 60 μL of sample for a single reading[10]. More importantly, the entire assay takes on the time-scale of days to complete. Such limitations make high power dilution of precious samples (such as mouse-tail-vein sera) unavoidable. Moreover, the high-power dilution will probably bring some samples (e.g., serum from mice that are in the estrus stage of the estrus cycles) out of their dynamic range. Because of these reasons, RIA approach is insufficient for monitoring fast developing events with relatively small mFSH fluctuations, such as the estrous cycle of a mouse, especially in real-time or quasi-real-time.

ELISA (enzyme-linked immunosorbent assay), specifically sandwich ELISA, provides an alternative approach to RIA for FSH quantification. Benefitting from the use of antibody pair,

sandwich ELISA usually has high specificity towards target antigens. This technique indeed improves the efficiency of human FSH quantification (from 2 days to ~5 hours)[11-12]. However, due to structural complexity, there is still no reliable commercial ELISA kit available for mFSH detection (most of the commercial kits could not generate the results comparable to those obtained with the gold standard RIA method). Furthermore, ELISA using a traditional 96-well plate suffers from other technical drawbacks, such as large sample/reagent consumption (~100 μL) and relatively long assay time (~5 hours).

In the past decade, various types of microfluidic ELISA devices have been developed to resolve the aforementioned problems of traditional ELISA [13-18]. However, most of them involve sophisticated fluidic designs and usually suffer from insufficient rinsing (due to residual liquids), low repeatability, strong background, small dynamic range, and large inter/intra group variance[14-17]. In particular, no device or the protocol exists for the rapid quantification of mFSH using small sample volumes. Here we developed a fully automated and robust microfluidic chemiluminescent ELISA device, the disposable polystyrene capillary sensor array, and the corresponding assay protocol for rapid and quantitative analysis of mFSH from mouse tail sera. It is shown that the sensitive quantification of mFSH can be completed within 30 minutes using only 8 μL of serum sample. It is further shown that our method is able to generate results comparable to RIA but has a significantly improved dynamic range (0.5–250 ng/mL). Due to the simplicity of the capillary structure and automation, the results exhibited low background noise and small inter-/intra-group variances. Finally, we applied the ELISA system in monitoring of the mFSH level across dramatic endocrine events, such as ovariectomy and transplantation of ovarian tissue, as well as moderate fluctuations during regular estrus cycles. Our work will lead to the development of an automated

system that can be used for continuous monitoring and rapid analysis of mFSH and other analytes in research laboratories (especially for small animal researches) and clinical settings.

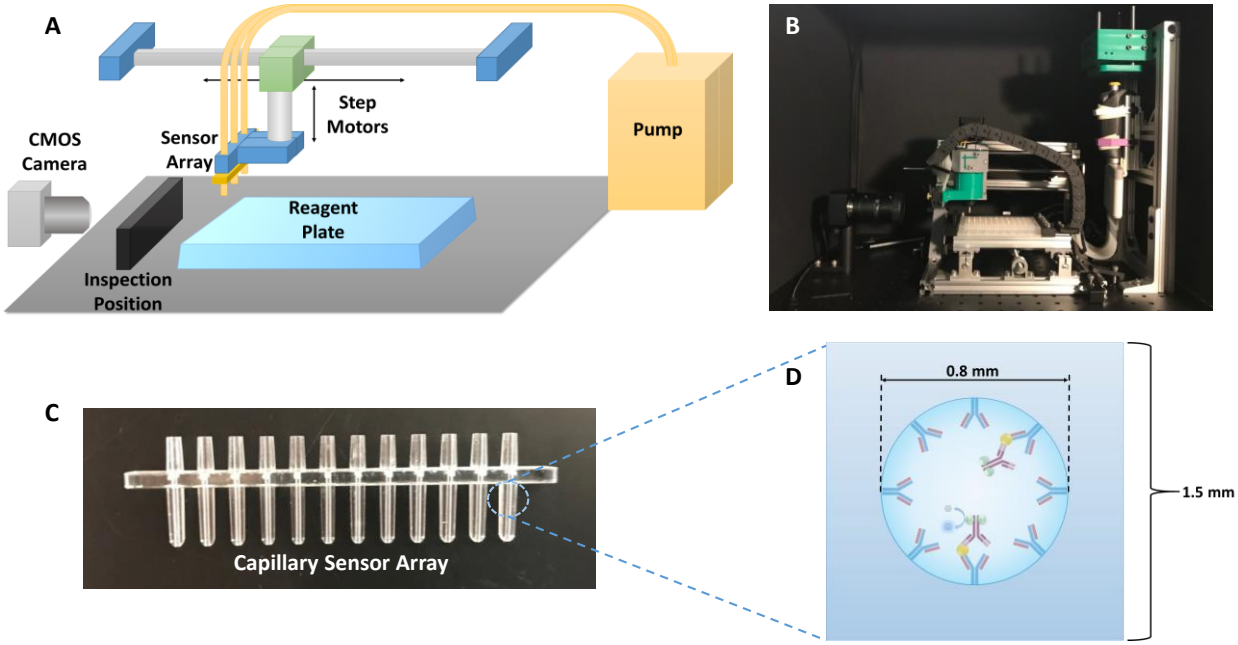

Figure 5.1. Layout, structure, and components of the automated ELISA device. (A) Illustration and (B) picture of the entire system. (C) Picture of a capillary sensor array. Each array contained 12 capillary units. The top portion of the array was connected to a liquid pump and the bottom portion was used to withdraw samples/reagents stored in the regent plate. (D) Cross-sectional view of a capillary with the inner diameter of 0.8 mm and the outer lateral size of 1.5 mm.

5.3. Materials and methods

5.3.1. Automated ELISA system

The automated ELISA system was designed, developed, assembled, and provided by Optofluidic Bioassay, LLC (Ann Arbor, MI), in collaboration with University of Michigan. As illustrated in Fig. 5.1, it consisted of a capillary sensor array, a liquid pump, a sample/reagent reservoir plate, a digital CMOS camera, and robotic arms, as well as a control/communication modules and software.

Unlike conventional plate-based ELISA techniques that perform ELISA reaction in centimeter-scale reaction wells, our automated chemiluminescent ELISA was performed in polystyrene capillary sensor arrays. The sensor arrays (Fig. 5.1(C)) were manufactured with the injection molding method. Each array contained 12 individual capillaries, each of which served as an ELISA reactor as well as a microfluidic channel. Benefited from this industrial-grade fabrication technique, the sensor arrays had tight quality control, thus significantly improving inter-/intra-assay variations. As shown in Fig. 5.1(D), the cross section of each capillary was designed to be circular to achieve better rinse and avoid the potential liquid residuals at the channel corners. Each capillary had the inner diameter of 0.8 mm and the total length of 16 mm. Therefore, the maximal ELISA reactor volume was only 8 μL. The capillary had a surface-to-volume ratio of 5 mm^{-1}, about 7 times higher than that for a traditional flat-bottom 96-well plate (0.73 mm^{-1}), which significantly increases the analyte capture efficiency and shortens the incubation time, as we demonstrated previously[19].

The top portion of each capillary was connected to a liquid pump to control the liquid into and out of the capillary. As illustrated in Fig. 5.1(A), during the operation, the samples and reagents were first placed in the different wells on a reservoir plate (Thermo Fisher 384-well plate, part no 12-566-213). Robotic arms moved the sensor array to the corresponding wells and sequentially withdraw samples/reagents from the wells into the capillaries, incubate, and then eject the wastes out of the capillaries. Finally, the sensor array was placed in front of a CMOS camera and the chemiluminescence signal from each capillary was recorded for post-experiment analysis. The details of the operation for mFSH detection is presented later in the Section “Procedures of mFSH analysis”.

5.3.2. Chemical reagents

The chemiluminescent substrate (SuperSignal™ ELISA Femto Substrate) was purchased from Thermo Fisher. The substrate kit (product no. 37075) contains a bottle of 50 mL Luminol + Enhancer Solution and a bottle of 50 mL Stable Peroxide Solution. The working substrate solution was prepared by equal-volumetrically mixing the Luminol + Enhancer Solution and the Stable Peroxide Solution at room temperature. The ELISA coating buffer (1× PBS, DY006), concentrated wash buffer (WA126), and concentrated reagent diluent (10% BSA in 10× PBS, DY995) were purchased from R&D Systems.

The mFSH standard used in this experiment was purchased from National Hormone and Peptide Program (NHPP, AFP5308D). A mouse monoclonal antibody that purchased from Thermo Fisher (P4G2, MIF2709) was used as capture antibody. The detection antibody was purified from National Hormone and Peptide Program's guinea pig anti-mFSH antiserum (AFP-1760191). Since the purified detection antibody did not come with any reporter enzyme, it was modified by conjugating with horseradish peroxidase (HRP) in a molar ratio of antibody : HRP = 1 : 4. The conjugation reaction was carried out with Abcam's HRP conjugation kit (ab102890).

The working solution of the wash buffer and reagent diluent were diluted with Milli-Q water (R = 18.2 Ω) to achieve 1× working concentration. In order to simulate the properties (e.g., viscosity) of real mouse serum, the antigen solvent, as well as the blocking buffer, used in this experiment was prepared by mixing fetal bovine serum (FBS) and 1× reagent diluent (1% BSA in PBS) in a volumetric ratio of 1 : 1.

The working solution of the capture antibody was prepared by diluting the stock solution with PBS buffer (pH = 7.4) to achieve a final concentration of 12 μg/mL. The concentrated mFSH standard was diluted to a desired concentration with the pre-mixed antigen solvent (i.e., 0.5× FBS).

The working solution of the detection antibody was prepared by diluting the HRP-labeled detection antibody 400 times (with 1× reagent diluent) to its final working concentration.

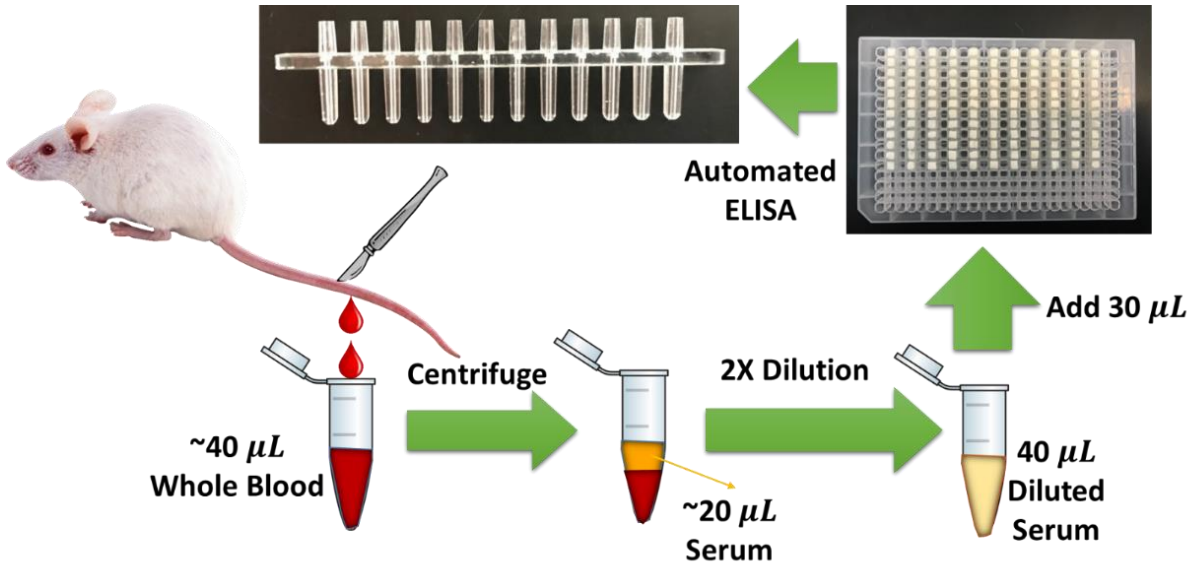

Figure 5.2. Illustration for the procedure of the entire mFSH assay. Briefly, ~40 μL of blood was collected from mouse tail vein for each measurement. ~20 μL of serum could be collected after centrifugation and subsequently diluted to 40 μL with 50% FBS in 1% BSA. 30 μL of the diluted sample was added to a well in the reagent reservoir plate. Finally, the mFSH was analyzed using the automated ELISA system.

5.3.3. Procedures of mFSH analysis

All experiments were performed at the University of Michigan, Ann Arbor. An illustration of the entire assay (from blood collection to final optical measurement) can be found in Fig. 5.2. In each test, 6 capillaries were used as calibration references to generate a calibration curve. The remaining 6 capillaries were dedicated to samples under test. Depending on the number of samples, single, duplicate, and triplicate measurements could be performed on each sample.

Before starting a test, all reagents and samples were added into the corresponding wells on the reagent reservoir plate (Thermo Fisher square well 384 well plate, part number 12-566-213). In order to make the liquid easily accessible by the capillaries, 30 µL of reagents/samples were added in each well, although less than 10 µL of reagents/samples were needed for each well (and

each capillary sensor). Since each capillary sensor needed only ~8 µL of reagents/samples in each test, the remaining volume (~22 µL) can be collected and reused in further experiments. In the near future, customized regent reservoir plates will be used to accommodate the capillary sensor array, so that only 10 µL for sample/reagent is needed to fill each well in the reservoir plate.

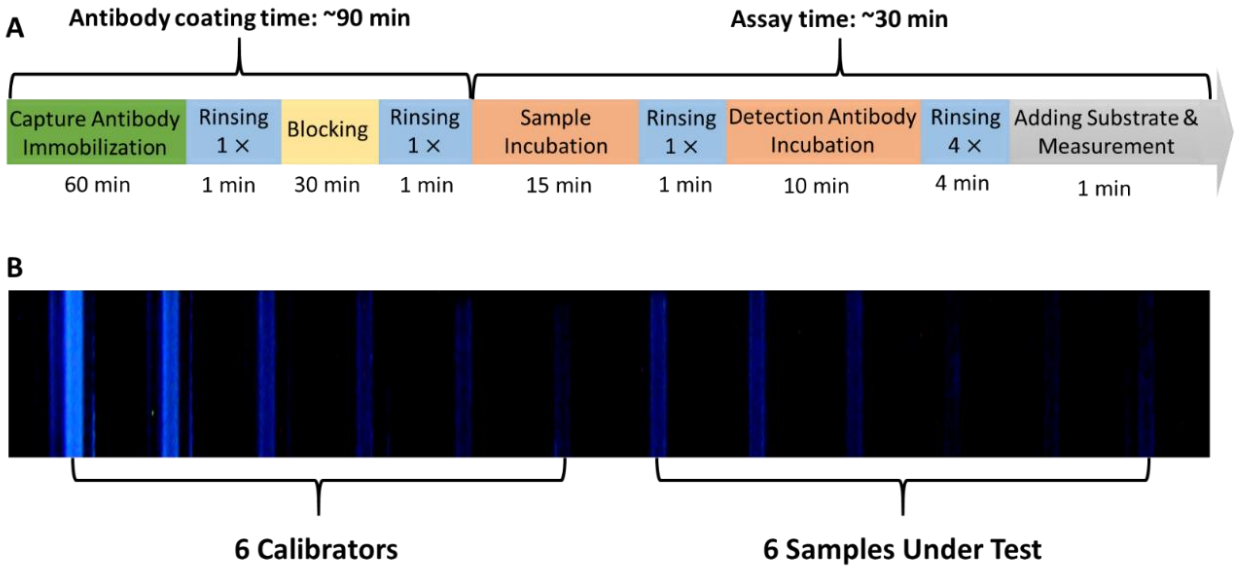

Figure 5.3. Illustration of the mouse FSH ELISA assay. (A) Protocol for mouse FSH measurement with the automated ELISA system. (B) Capillary arrangement within a sensor array. Six capillaries on the left side were used as calibrators to generate a calibration curve. The remaining six capillaries were used for measuring actual samples.

The capillary sensors needed to go through capture antibody coating and surface blocking before actual sample measurement (see Fig. 5.3(A)). The capture antibody immobilization (through physical adsorption) was performed by incubating the capture antibody working solution at room temperature in the capillary for one hour. After rinse with wash buffer, the blocking buffer was added and incubated for another 30 minutes.

The actual assay included three steps, sample incubation, detection antibody incubation, and chemiluminescent intensity measurement, as illustrated in Fig. 5.3(A). The sample incubation and detection antibody incubation took 15 minutes and 10 minutes, respectively. The

chemiluminescent intensity measurement was performed immediately after adding the substrate into the capillary reactors. (According to the user's manual, the emission intensity of the SuperSignal™ substrate remains steady for first few minutes of incubation). The total assay time was approximately 30 minutes, including ~5 minutes of rinsing, the time for robotic arms' movements, and optical detection, which is about 100 times faster than the standard mFSH RIA test (which usually takes about two days[10, 20]), 10 times faster than a typical sandwich ELISA assay (For example, according to the user's manual of a typical sandwich ELISA kit from R&D Systems, the total assay time is approximately 320 minutes), and similar to most of the microfluidic ELISA techniques that designed for protein quantification [14, 17, 21].

The results of the capillary chemiluminescent ELISA experiments were recorded with the CMOS camera and subsequently quantified through a previously established chemiluminescent imaging method[19]. Briefly speaking, signal from the blue channel was extracted from the image. Then, the intensity along the central axis of each capillary was recorded and then averaged along the capillary longitudinal direction with Image J software. More details can be found in chapter 4[19].

5.3.4. Animal experiments

The IACUC guidelines for survival surgery in rodents and the IACUC Policy on Analgesic Use in Animals Undergoing Surgery were followed for all the procedures (PRO00007716).

In each collection, approximately 40 μL of blood was collected from the lateral tail vein at designated time points with a 53/4 in. glass Pasteur pipette up to the time of sacrifice. After collection, all samples were stored at 4 °C overnight, then centrifuged for 10 min at 10,000 rpm and the collected serum was stored at −20 °C.

To assess estrus cycle, vaginal cytology was performed in mice. Vaginal cytology was resumed after 7 days following all procedures (ovariectomies and subcutaneous implantations of ovarian tissue) and was performed daily until sacrifice. The transition from leukocytes to cornified cells at least once a week was considered as a resumed or continued cycle.

Following sacrifice, the implanted ovaries were retrieved from mice and fixed in Bouin's fixative at 4 ^{o}C overnight. The fixed ovaries were then transferred and stored in 70% ethanol at 4 ^{o}C. After processing, samples were embedded in paraffin, serially sectioned at 5 μm thickness, and stained with hematoxylin and eosin.

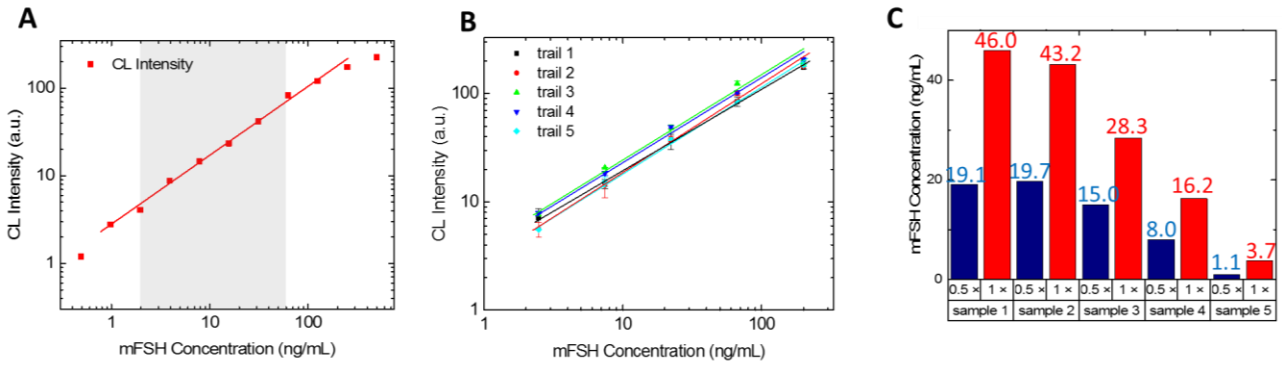

Figure 5.4. Calibration results of the mFSH assay. (A) Dynamic range of the FSH assay. The linear response range is between 1 ng/mL and 250 ng/mL. The red line is the linear regression between 1 and 250 ng/mL in the log-log scale. The shaded area denotes the dynamic range of mFSH RIA. (B) The inter-group performance of the automated ELISA system for mFSH assay. The inter-group variances at 200, 66.67, 22.22, 7.41, and 2.47 ng/mL are 1.27%, 3.50%, 3.93%, 5.80%, and 9.08%, respectively. The error bars are the standard deviations calculated from duplicate measurements. The solid lines are linear regressions in the log-log scale. (C) The measurement results before and after 2X dilution.

5.4. Results

5.4.1. Assay performance evaluation

The calibration measurement results using the mFSH standards (500, 250, 125, 62.5, 31.25, 15.63, 7.81, 3.91, 1.95, 0.98, 0.49, and 0 ng/mL) with the automated ELISA system are shown in Fig. 5.4(A). The data point at 0 ng/mL serves as the background of the assay and is subtracted from the readings of other concentrations. The linear dynamic range of the mFSH assay is between 1 ng/mL

and 250 ng/mL, which is significantly broader than the dynamic range in conventional RIA (shown as the shaded area in Fig. 5.4(A)). The limit of detection is 0.5 ng/mL. The calibration curve (between 1 and 250 ng/mL) has a slope of 0.77 in the log-log scale. Since the detection antibody used in our work is the same as the one used in conventional RIA[10, 20], our technique should has same or improved specificity due to the employment of the additional monoclonal capture antibody[22]. A comparison between the RIA's calibration curve (dynamic range varies between 1.6-37 ng/mL and 3-75 ng/mL) and the calibration curve obtained with our ELISA system can be found in Fig. 5.5.

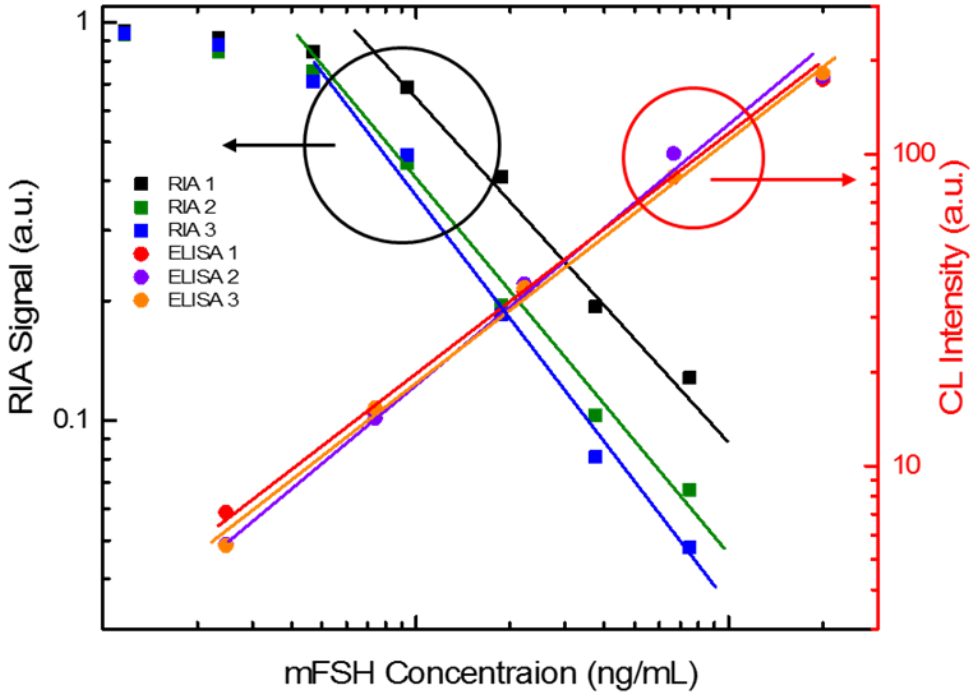

Figure 5.5. Comparison between microfluidic chemiluminescent ELISA and RIA. The typical dynamic ranges for mFSH RIA varies between 1.6-35 ng/mL and 3-75 ng/mL with logistic regression. When plotting the calibration points in the log-log scale, they become mostly linear within 5-75 ng/mL (10-75 ng/mL in some cases) with a slope of approximately -0.84. Both of them are much smaller than the dynamic range of the microfluidic chemiluminescent ELISA technique, which is 1-250 ng/mL with a linear regression model in the log-log scale (a slope around 0.77 with ~5 % inter-assay variance).

In practice, 6 capillaries were used for calibrators and the rest 6 capillaries were for actual samples. Therefore, we selected five different mFSH concentrations within the linear response range in Fig. 5.4(A) (200, 66.67, 22.22, 7.41, and 2.47 ng/mL), as well as a zero background (50% FBS in 1% BSA) to generate the calibration curve. In order to examine the inter-group consistency of our ELISA system, multiple mFSH assays with these calibration concentrations were performed on different days. The results are presented in Fig. 5.4(B). The background reading was subtracted from those of non-zero mFSH concentrations. The slopes of these five calibration curves were very close to each other. The average slope (in the log-log scale) was 0.77 and the standard deviation for the slopes was 0.03. The inter-group variances at 200, 66.67, 22.22, 7.41, and 2.47 ng/mL are 1.27%, 3.50%, 3.93%, 5.80%, and 9.08%, respectively. These data indicate the stability of our system is better than mFSH RIA (Fig. 5.5.) and on par with (or even better than) most of the conventional ELISA techniques[23] and competing microfluidic ELISA devices[17, 24-25].

Since the amount of serum is limited and usually less than our desired volume (30 μL), two times dilution became necessary for most of the samples. In order to explore the impact on measurement caused by dilution, we performed a comparison experiment on five samples. As the results shown in Fig. 3C, the measurement results obtained with two times diluted samples were close to 0.5 times of the results generated with original serum. These results indicate that the dilution does not cause significant errors that affect further analysis. In the future, a smaller reservoir plate will be used with only 15 μL for each well so that dilution of serum sample will become unnecessary. In addition, the measurement results generated with our microfluidic chemiluminescent ELISA are generally comparable to those generated with RIA (as presented in Fig. 5.6).

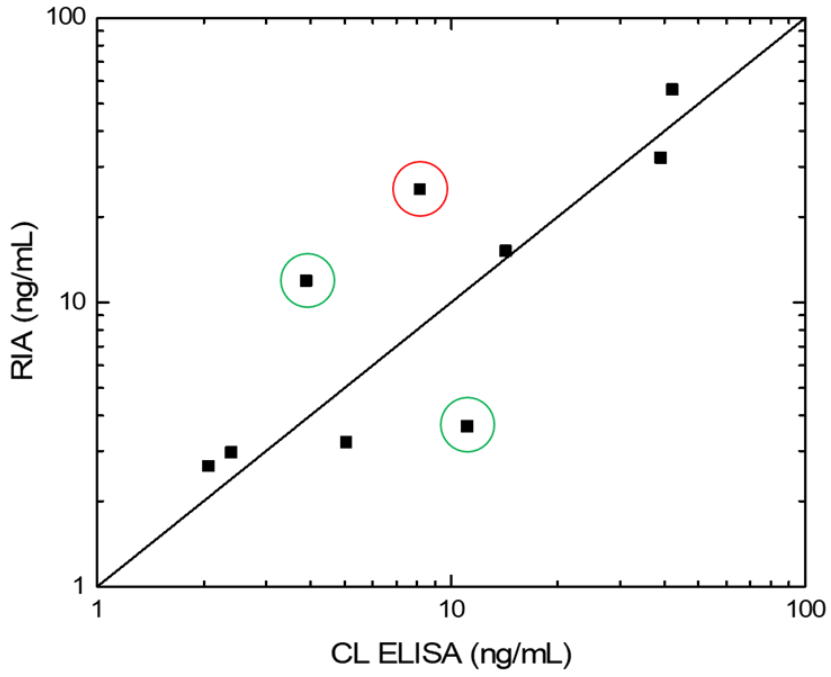

Figure 5.6. Comparison between the readings measured with our ELISA system and the traditional RIA done at the University of Virginia. The results generated with these two methods generally have the same trends and most of them appears to be comparable. However, three of the data points do not correlate very well. The outliers are labeled with circles. The RIA result for one of the outliers (indicated by the red circle) is believed to have low reliability, because 25 ng/mL does not appear to be a correct serum mFSH concentration for a healthy adult mouse, which normally has an mFSH level lower than 20 ng/mL.

5.4.2. Tracking mFSH level in post-ovariectomized mice

In order to verify the practicality of this technique in real-world animal research, we designed a long-term study for tracking the mFSH level in mouse serum over dramatic endocrine events using a group of healthy wild type mice (n=4). Briefly, on Day 0 of this study, we performed ovariectomy (removal of ovaries) in all four mice within this group. On Day 35 of this study, we transplanted a functional ovary into two of the four mice. In order to reduce organ rejection effect, the ovaries were collected from two donors that have same genotype with the experiment subject[26-

[27]. All four mice were sacrificed on Day 98, which corresponds to the end of this study. As described in the "Materials and methods" section, in order to closely monitor the blood mFSH level without overly interference with the animal's regular physiological function, ~40 µL of blood was collected from the tail vein of each mouse every 7 days, which means that ~20 µL of serum could be obtained after centrifugation.

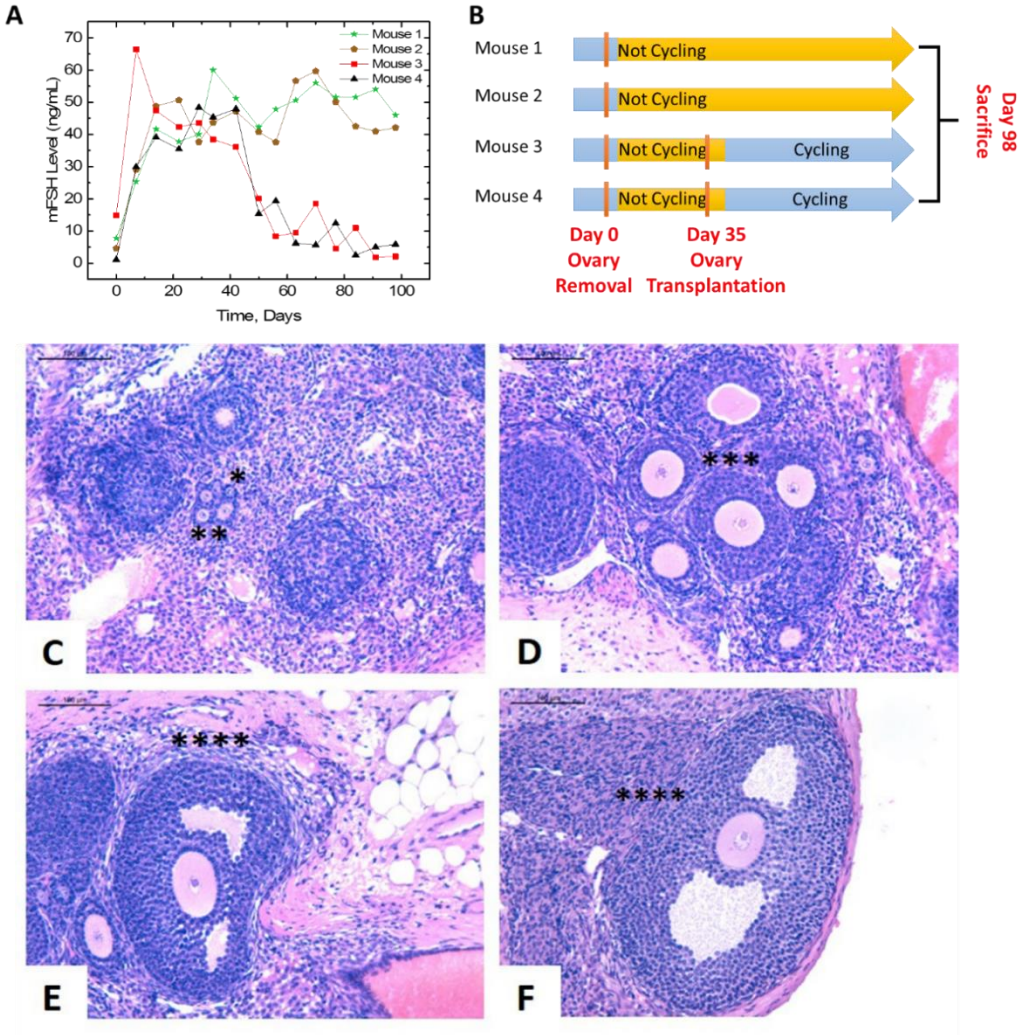

Figure 5.7. Surgery related mFSH results. (A) The mFSH measurement results for Mice 1-4. The ovariectomy surgeries were performed on Day 0 (for all four mice), and ovary implantation surgeries were performed on Day 35 (for Mice 3 and 4). (B) A qualitative summary of vaginal cytology results. Mice 3 and 4 started to cycle again after Day 44 (9 days after ovary transplantation). (C-F) Histological images of syngeneic ovarian tissue subcutaneously implanted in ovariectomized mice showing (C) primordial (*) and primary follicles (**), (D) secondary follicles (***), and (E, F) antral follicles (****), which indicates the implanted ovaries were still functioning normally by Day 98 (in Mice 3 and 4). Magnification = 20X.

Ovaries are hormone-secreting organs and their removal causes a dramatic decrease in serum estrogen concentration (estrogen serves as a signaling molecule for the negative feedback), thus terminating the feedback control loop (hypothalamus-pituitary-gonadal axis) for mFSH stabilization. As a result, the anterior pituitary releases more mFSH to stimulate the ovaries that are not there to respond. Without the negative feedback of estradiol, the pituitary continues to release mFSH resulting in increasing blood levels of the unregulated gonadotrophic factor.[28]. To reverse the effects of ovariectomy, the ovary transplantation surgery restores the estrogen production and elevates concentrations in circulating blood. The restored feedback control system eventually lowers the mFSH concentration back to the normal range through the restoration of hypothalamus-pituitary-gonadal axis. If our methodology and device are sensitive enough, we should be able to observe the fluctuations in mFSH concentration that are directly related to these two surgical events (i.e., removal and transplantation of ovary).

As shown in Fig. 5.7, the serum mFSH concentration for all four mice increased dramatically to >35 ng/mL within two weeks after ovariectomy. Starting from Day 21 post-ovariectomy, the serum mFSH level of all four mice became steady at ~40 ng/mL, which indicates that the anterior pituitary glands reach their maximal mFSH productivity. On Day 35, ovary transplantation surgeries were performed on Mice 3 and 4. However, the mFSH level one week post-transplantation (Day 42) remains mostly unchanged, indicating that the restoration of the feedback control loop takes more than one week to complete, which is consistent with other reports [29-30]. After that, the mFSH level in the two implanted mice started to drop back to the normal physiological range (<20 ng/mL). This significant decrease occurred between Day 42 and Day 63. After four weeks post-transplantation, the mFSH level in Mice 3 and 4 became mostly steady (averaged mFSH concentration less than 10 ng/mL) with an obvious periodic fluctuation. In

contrast, the mFSH level for Mice 1 and 2 remained above 35 ng/mL. This phenomenon suggests that the implanted ovary tissue had successfully restored the estrus cycle in Mice 3 and 4. As presented in Fig. 4B, the restoration of hypothalamus-pituitary-gonadal axis (shown as cellular cyclicity) for the ovary-implanted mice has been verified through vaginal cytology during the monitoring period. Histological analysis of the implanted ovaries (Figs. 5.7 (C)-(F)) correlated with our FSH serum levels and vaginal cytology measurements. Presence of postovulatory structures in the implanted ovarian tissue was confirmed by the presence of estrous cycles identified using vaginal cytology. In addition, there are still multiple early-stage follicles in the transplanted ovary by the day of sacrifice (Day 98). These pieces of evidence indicate that the implanted ovaries were still functioning by Day 98. The results also proved that Mice 3 and 4 could be deemed as heathy adult mice after Day 63 of this study.

The results presented in Fig. 5.7(A) clearly demonstrates the capability of our microfluidic chemiluminescent ELISA device to quantitatively differentiate the mFSH level before and after ovariectomy surgery, as well as the change caused by ovary transplantation, with only 20 μL of mouse tail serum. More importantly, the periodic fluctuation that we observed in the ovary-transplanted mice indicates that our technique can possibly differentiate the stages in a mouse's estrus cycle that usually has low mFSH levels (1-20 ng/mL).

5.4.3. Tracking mFSH level over estrus cycles

In order to verify the ability of our ELISA system to quantitatively differentiate the stages in a mouse's estrus cycle through serum mFSH concentration, we designed another mid-term in-vivo study. Since mice have very small total blood volume (~2.5 ml), we are unable to collect 40 μL of blood on a daily basis. Previous research has shown that the duration of an estrus cycle in mice is approximately 4-5 days and the duration of one stage in a single cycle is approximately

one day. Therefore, if we collect blood every 7 days, the collected serum samples will fall into different stages for at least every three collections. In order to verify this claim, we performed a five-week-long tail vein blood study with six healthy female mice (including the two ovary transplanted mice after Day 63, Mice 3 and 4).

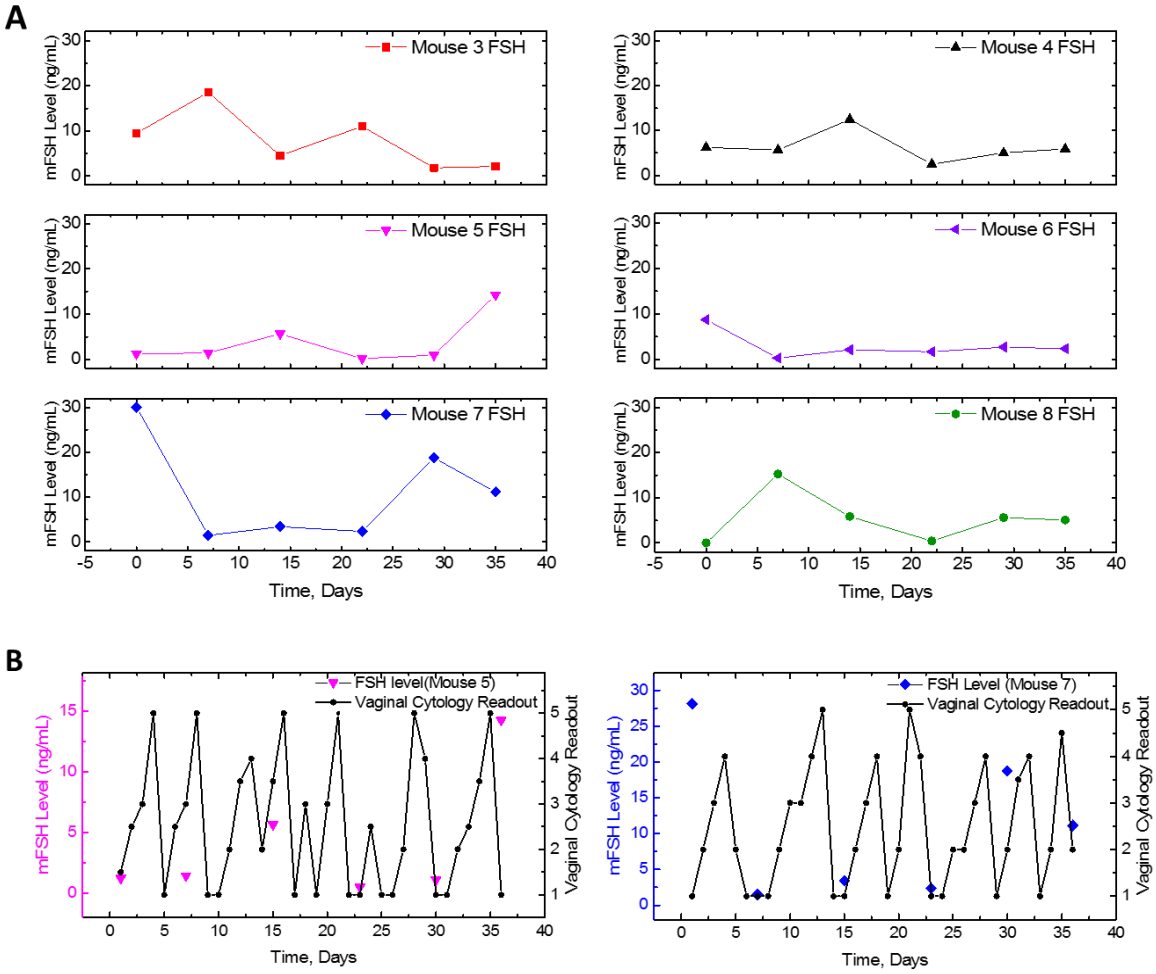

Figure 5.8. Estrus cycle analysis results. (A) mFSH measurements for six individual mice during a 36-day monitoring period. Clear fluctuations can be observed in all of them. The peak mFSH levels vary significantly among mice, whereas the valley mFSH levels remain quite similar. (B) Comparison between the cyclicity observed from vaginal cytology and mFSH measurements for Mouse 5 and Mouse 7. Both sets of the comparison show that the mFSH measurement lags the vaginal cytology readouts by 1-1.5 days.

Significant mFSH fluctuations in all mice in the study corresponded with the expected outcomes (Fig. 5.8(A)). For each individual mouse, the difference between the peak mFSH and the valley mFSH values can be easily distinguished, suggesting that our technology is able to

differentiate stages in an estrus cycle through mFSH concentrations. It is seen that the peak mFSH concentration varies significantly among all mice and falls into a wide range between 6 and 28 ng/mL. The valley mFSH concentration, however, is quite similar for all six mice, between 0.5 and 2.5 ng/mL.

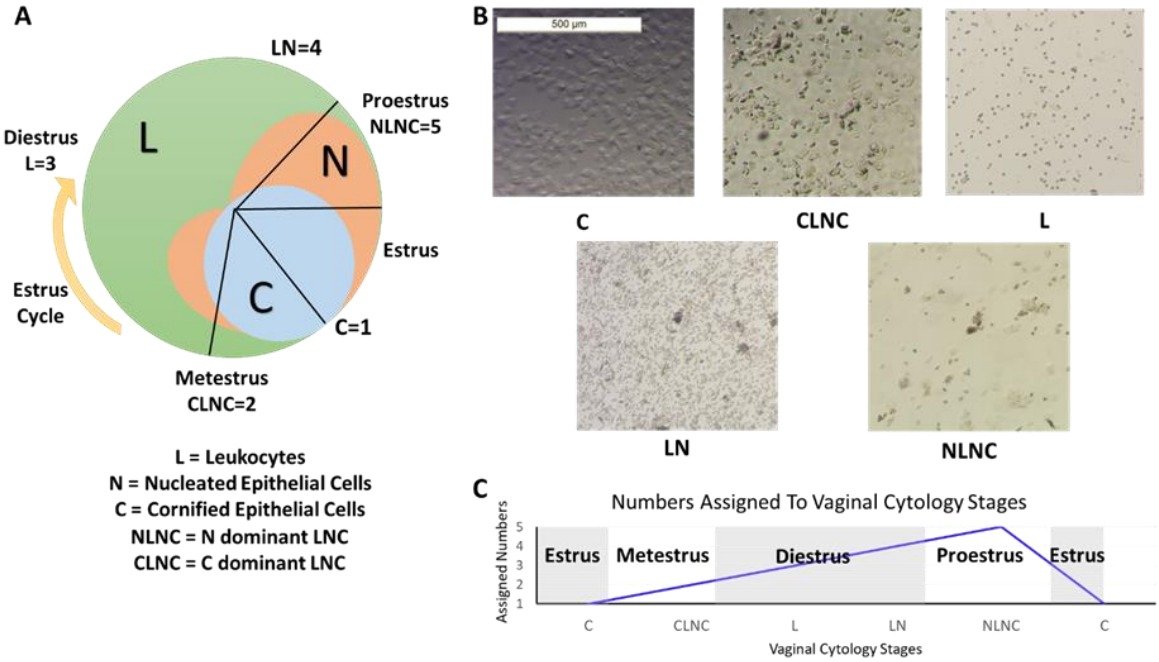

Figure 5.9. The rule for assigning values to different stages in an estrus cycle. (A) The structure of a typical mice estrus cycle (from vaginal cytology) and the corresponding assigned values for each stages. (B) Exemplary vaginal cytology images for each stage. (C) A graphical illustration of value assigning strategy and the correlation between vaginal cytology readout and the stages in an estrus cycle.

The results collected with the mFSH chemiluminescent ELISA measurement were also compared with those obtained with daily vaginal cytology. Since the vaginal epithelial condition is directly regulated by the estrogen level, from vaginal cytology readouts we are able to estimate the corresponding estrogen level at that time point. In order to intuitively compare the vaginal cytology results and FSH measurements, we assigned numerical values to each stages in a vaginal epithelial cycle[31-32]. For example, the value for C phase (later estrus stage) was assigned to be 1 and the value for NLNC phase (later diestrus stage and early proestrus stage) was assigned to be 5

because the estrogen level usually reaches its peak level in this phase. Beside these two, CLNC phase, L phase, and LN phase were assigned to be 2, 3, and 4, respectively. The intermediate situations were assigned to be the average between two neighboring stages (such as 2.5 and 3.5, etc.). The rule for assigning numerical values and the exemplary vaginal cytology readouts are shown in Fig. 5.9.

With these numerically values, we can directly compare the vaginal cytology readouts and mFSH readout on the same plot. Mice 5 and 7 were selected as two representatives because they have the most obvious and stable cycling pattern. The results are shown in Fig. 5B. The readouts from these two mice during the 35 days of experiment presented a lagging period between the vaginal cytology pattern and the measured mFSH pattern. Based on the results generated from these two mice, the lagging time is estimated to be approximately one day, which agrees well with the pattern reported in literatures[32-34].

5.4. Discussion

In the mice experiments, we observed a few interesting phenomena. For the ovary transplantation experiment, based on vaginal cytology measurements, the estrus cycle started to appear 9 days after implantation (Day 44 from the start date of the study) and the serum mFSH concentration started to decrease on Day 14 after implantation. This agrees with the theory that serum mFSH is a downstream marker during the restoration of the sex hormone feedback loop (hypothalamus-pituitary-gonadal axis). Previous research using RIA based mFSH quantification technique also observed the same phenomena (REF). However, since the required blood volume was relatively large (~90 μL) and the time interval between two consecutive blood collections had to be14 days for the well-being of the animals, it was difficult to quantify the lagging time between

the restoration of gonad endocrine function and the restoration of the feedback loop[29, 35]. With the described ELISA system, we were able to shorten this time interval down to one week (with only ~40 μL of blood). Based on the results shown in Figs. 4A and B, we can see clearly that the delay between vaginal epithelial response (gonad endocrine function) and serum mFSH response (restoration of feedback loop) should be between 1 and 5 days. More accurate result can be generated if we can further reduce the time interval between two blood collections, which will also be our research direction in the near future.

In the estrus cycle study, we observed a very stable 1-1.5 days of lagging between the vaginal cytology readouts and serum mFSH readouts, which agrees with other researchers' opinions regarding inter-hormone correlation in mice estrus cycle[33]. However, previous studies show that the peak mFSH level is hard to capture because it only lasts for a short period of time (~12 hours)[36]. Based on our current work, we can either predict the mFSH level from the non-invasive vaginal cytology readout, or capture or quantify the mFSH peak intensity timely in each estrus cycle. Such capability is very beneficial to pituitary function and activity studies.

5.5. Conclusion and Future Prospects

In this work, we have developed a robust and automated ELISA system and the corresponding protocol for mFSH measurement, in which the mFSH measurement can be completed within 30 minutes by using 8 μL of serum sample (~100 times faster and 7 times lesser of samples than RIA). Benefitted from the programmable automated operation, the inter assay variance could reduce to <10 %, thus achieving comparable results with RIA but having a significantly larger dynamic range (1-250 ng/mL), which is very beneficial for analyzing samples in extreme conditions, such as serum from post-ovariectomized mice and regular mice in the

estrus/metestrus stages of their estrus cycles. The results presented in in this work reveal that our technology has the ability to quantitatively differentiate the mFSH level before and after overiectomy surgery, as well as the changes caused by ovary transplantation surgery. In addition, our technology is able to differentiate stages in an estrus cycle, even at low mFSH levels (1-20 ng/mL). More significantly, the dynamic range is adjustable through changing the incubation times, which resulted in a detection limit as low as 0.25 ng/mL. (For the targets with well-optimized antibodies, such as human IL-6, the detection limit can be even lower).

Such a feature can certainly benefit studies for different purposes, especially for monitoring estrus cycles with a high sampling frequency. Since the concept of this assay (sandwich immunoassay) is universal, it can easily be adapted for the quantification of any other proteins, hormones, and peptides (the only limitation is the availability of antibodies). In the near future, we envision that this system may have the capability to monitor various types of specific functional proteins in precious animal samples (e.g., urine, saliva, or even whole blood) besides the mFSH levels in mouse serum. Owing to the compact size of the commercial plate reader, the device can be exploit for on-site detection. By reengineering the design of the reagent reservoir plate, the required sample volume is expected to be further reduced to ~10 μL, providing a much more efficient paradigm for quantification and biomedical analysis.

5.6. References

1. Pierce, J. G.; Parsons, T. F., Glycoprotein hormones: structure and function. *Annu. Rev. Biochem* **1981,** *50* (1), 465-495.

2. Le Tissier, P.; Hodson, D.; Lafont, C.; Fontanaud, P.; Schaeffer, M.; Mollard, P., Anterior pituitary cell networks. *Front. Neuroendocrinol.* **2012,** *33* (3), 252-266.

3. Jiang, X.; Liu, H.; Chen, X.; Chen, P.-H.; Fischer, D.; Sriraman, V.; Henry, N. Y.; Arkinstall, S.; He, X., Structure of follicle-stimulating hormone in complex with the entire ectodomain of its receptor. *Proc. Natl. Acad. Sci. U.S.A* **2012,** *109* (31), 12491-12496.

4. Meethal, S. V.; Atwood, C., The role of hypothalamic-pituitary-gonadal hormones in the normal structure and functioning of the brain. *Cell. Mol. Life Sci.* **2005,** *62* (03), 257-270.

5. Marieb, E. N.; Hoehn, K., *Human anatomy & physiology*. Pearson Education: 2007.

6. Nelson, R. J., *An introduction to behavioral endocrinology*. Sinauer Associates: 2011.

7. Butcher, R.; Collins, W.; Fugo, N., Plasma concentration of LH, FSH, prolactin, progesterone and estradiol-17β throughout the 4-day estrous cycle of the rat. *Endocrinology* **1974,** *94* (6), 1704-1708.

8. Sherman, B. M.; Koreman, S. G., Measurement of serum LH, FSH, estradiol and progesterone in disorders of the human menstrual cycle: the inadequate luteal phase. *J. Clin. Endocrinol. Metab* **1974,** *39* (1), 145-149.

9. Pratt, J.; Woldring, M., Radioimmunoassay specificity and the "first-come, first-served effect". *Clin. Chim. Acta* **1976,** *68* (1), 87-90.

10. University of Virginia School of Medicine Assay Methods. https://med.virginia.edu/research-in-reproduction/ligand-assay-analysis-core/assay-methods/.

11. Liew, M.; Groll, M. C.; Thompson, J. E.; Call, S. L.; Moser, J. E.; Hoopes, J. D.; Voelkerding, K.; Wittwer, C.; Spendlove, R. S., Validating a custom multiplex ELISA against individual commercial immunoassays using clinical samples. *Biotechniques* **2007,** *42* (3), 327.

12. Lindau-Shepard, B.; Roth, K. E.; Dias, J. A., Identification of amino acids in the C-terminal region of human follicle-stimulating hormone (FSH) beta-subunit involved in binding to human FSH receptor. *Endocrinology* **1994,** *135* (3), 1235-1240.

13. Madaboosi, N.; Pedrosa, C. R.; Reis, M. F.; Soares, R. R.; Chu, V.; Conde, J. P. In *Microfluidic ELISA for sensing of prostate cancer biomarkers using integrated a-Si: H pin photodiodes*, Sensors, 2014 IEEE, IEEE: 2014; pp 881-884.

14. Giri, B.; Dutta, D., Improvement in the sensitivity of microfluidic ELISA through field amplified stacking of the enzyme reaction product. *Anal. Chim. Acta* **2014,** *810*, 32-38.

15. Hoegger, D.; Morier, P.; Vollet, C.; Heini, D.; Reymond, F.; Rossier, J. S., Disposable microfluidic ELISA for the rapid determination of folic acid content in food products. *Anal. Bioanal. Chem.* **2007,** *387* (1), 267-275.

16. Herrmann, M.; Veres, T.; Tabrizian, M., Enzymatically-generated fluorescent detection in micro-channels with internal magnetic mixing for the development of parallel microfluidic ELISA. *Lab Chip* **2006,** *6* (4), 555-560.

17. Kubo, I.; Kanamatsu, T.; Furutani, S., Microfluidic Device for Enzyme-Linked Immunosorbent Assay (ELISA) and Its Application to Bisphenol A Sensing. *Sens. Mater.* **2014,** *26* (8), 615-621.

18. Proczek, G.; Gassner, A.-L.; Busnel, J.-M.; Girault, H. H., Total serum IgE quantification by microfluidic ELISA using magnetic beads. *Anal. Bioanal. Chem.* **2012,** *402* (8), 2645-2653.

19. Tan, X.; Oo, M. K. K.; Gong, Y.; Li, Y.; Zhu, H.; Fan, X., Glass capillary based microfluidic ELISA for rapid diagnostics. *Analyst* **2017**, 2378.

20. University of Wisconsin WNPRC Assay Service Home. https://www.primate.wisc.edu/?page_id=2231 (accessed 03/14).

21. Mirasoli, M.; Guardigli, M.; Michelini, E.; Roda, A., Recent advancements in chemical luminescence-based lab-on-chip and microfluidic platforms for bioanalysis. *J Pharm Biomed Anal* **2014,** *87*, 36-52.

22. Pei, X.; Zhang, B.; Tang, J.; Liu, B.; Lai, W.; Tang, D., Sandwich-type immunosensors and immunoassays exploiting nanostructure labels: A review. *Anal. Chim. Acta* **2013,** *758*, 1-18.

23. Baines, H.; Nwagwu, M. O.; Hastie, G. R.; Wiles, R. A.; Mayhew, T. M.; Ebling, F. J., Effects of estradiol and FSH on maturation of the testis in the hypogonadal (hpg) mouse. *Reprod. Biol. Endocrinol.* **2008,** *6* (1), 4.

24. Otieno, B. A.; Krause, C. E.; Jones, A. L.; Kremer, R. B.; Rusling, J. F., Cancer diagnostics via ultrasensitive multiplexed detection of parathyroid hormone-related peptides with a microfluidic immunoarray. *Anal. Chem.* **2016,** *88* (18), 9269-9275.

25. Novo, P.; Chu, V.; Conde, J., Integrated optical detection of autonomous capillary microfluidic immunoassays: a hand-held point-of-care prototype. *Biosens. Bioelectron.* **2014,** *57*, 284-291.

26. Wu, T.; Zhao, Y.; Zhao, Y., The roles of myeloid-derived suppressor cells in transplantation. *Expert Rev Clin Immunol* **2014,** *10* (10), 1385-1394.

27. Laffery, K. J.; Prowse, S. J.; Simeonovic, C. J.; Warren, H. S., Immunobiology of tissue transplantation: a return to the passenger leukocyte concept. *Annu. Rev. Immunol.* **1983,** *1* (1), 143-173.

28. Benson, B.; Sorrentino, S.; Evans, J. S., Increase in serum FSH following unilateral ovariectomy in the rat. *Endocrinology* **1969,** *84* (2), 369-374.

29. Kim, J.; Perez, A. S.; Claflin, J.; David, A.; Zhou, H.; Shikanov, A., Synthetic hydrogel supports the function and regeneration of artificial ovarian tissue in mice. *NPJ Regen Med* **2016,** *1*, 16010.

30. Shikanov, A.; Zhang, Z.; Xu, M.; Smith, R. M.; Rajan, A.; Woodruff, T. K.; Shea, L. D., Fibrin encapsulation and vascular endothelial growth factor delivery promotes ovarian graft survival in mice. *Tissue Eng Part A* **2011,** *17* (23-24), 3095-3104.

31. Byers, S. L.; Wiles, M. V.; Dunn, S. L.; Taft, R. A., Mouse estrous cycle identification tool and images. *PloS one* **2012,** *7* (4), e35538.

32. Miller, B. H.; Takahashi, J. S., Central circadian control of female reproductive function. *Front. Neuroendocrinol.* **2014,** *4*, 195.

33. Staley, K.; Scharfman, H., A woman's prerogative. *Nat. Neurosci.* **2005,** *8* (6), 697.

34. Scharfman, H. E.; MacLusky, N. J., Estrogen–growth factor interactions and their contributions to neurological disorders. *Headache* **2008,** *48* (s2), s77.

35. David, A.; Day, J. R.; Cichon, A. L.; Lefferts, A.; Cascalho, M.; Shikanov, A., Restoring ovarian endocrine function with encapsulated ovarian allograft in immune competent mice. *Ann Biomed Eng* **2017,** *45* (7), 1685-1696.

36. Murr, S. M.; Geschwind, I.; Bradford, G., Plasma LH and FSH during different oestrous cycle conditions in mice. *J Reprod Fert* **1973,** *32* (2), 221-230.

Chapter 6

Multiparameter Urine Analysis for Quantitative Bladder Cancer Surveillance of Orthotopic Xenografted Mice

6.1. Introductory Remarks:

In this chapter, we applied the improved (mature) version of the automated microfluidic ELISA platform to the surveillance of bladder cancer in an animal model. We have successfully developed a rapid, multiparameter urine-based biomolecular prognostic technology for orthotopic bladder cancer xenografts. This method consists of two steps. First, the concentrations of a panel of four urinary biomarkers are quantified from the urine of mice bearing orthotopic bladder xenografts. Second, machine learning and principal component analysis (PCA) algorithms are applied to analyze the urinary biomarkers, and subsequently, a score is assigned to indicate the tumor growth. With this methodology, we have quantitatively monitored the orthotopic growth of human bladder cancer that was inoculated with low, medium, and high cancer cell numbers. Note that the materials in this chapter was published on *Lab on a Chip* in 2020.

6.2. Motivations

Bladder cancer is the sixth most common malignant tumor in the United States and is one of the most widespread carcinomas globally [1,2]. To study tumor progression, invasion mechanisms, and therapeutic strategies for invasive bladder cancers in humans, biologically relevant mouse

models of cancer have been developed including carcinogen-based [3,4], genetically engineered [5], and human-derived xenografts [6]. The human-derived orthotopic xenograft model is believed to have high clinical relevance because of its high throughput, low cost, and high similarity to cancer found in patients [6]. In our most-updated approach, bladder cancer cell lines are directly inoculated into the bladder lumen of NSG (NOD *scid* gamma) mice [7] where they rapidly seed into the urothelial lining [6]. Consequently, tumors can develop quickly in the mouse bladder environment.

The surveillance of tumor progression in all human-derived orthotopic bladder xenografts still highly depends on either end-point pathological and immunohistochemical analyses, or *in vivo* imaging technologies such as PET-CT (Positron emission tomography–computed tomography) [8,9], MRI (magnetic resonance imaging)[10], ultrasound imaging[11] and bioluminescence imaging [12,13]. However, end-point histological analyses cannot provide real-time information regarding tumor progression. The real-time *in vivo* imaging approaches, while being able to estimate the tumor size during growth, require expensive equipment, time-consuming steps, imaging agents, hair removal, anesthetics, and limitations in device capacity for the number of mice [14]. More importantly, these *in vivo* imaging approaches generally cannot provide any biomolecular information about the tumor. Even more, as one of the most commonly used approaches for tumor surveillance in animal models, bioluminescence intensity may provide only semi-quantitative information about the tumor size. In addition, since genetically modified-cell lines are needed, it may be difficult to extend bioluminescence imaging approaches to other types of animal models (*e.g.*, carcinogen induced cancer models). Thus, a broadly applicable, convenient, and non-invasive technology is highly desired to quantitatively monitor the progression of orthotopically implanted human tumor xenografts.

Urine carries a vast amount of cellular and biomolecular information related to urinary diseases

[15,16]. It has been found that urinary biomarkers can be used to provide diagnostic and prognostic information for human bladder cancers [16-18]. Therefore, detection of a panel of selected biomarkers in urine may provide a simple, cost-effective, and non-invasive means for tumor progression monitoring. However, the correlation between a panel of multiple urinary biomarkers and tumor progression in the orthotopic bladder cancer xenograft model has not been investigated. This is due in part to the limited analytical capability of the traditional ELISA (enzyme-linked immunosorbent assay) technology that is widely used in analyzing biomarkers in urine, but suffers from low sensitivity, long assay time (typically 4-6 hours), and large sample volumes (typically 50-100 μL per marker) which are difficult for a mouse to produce [19].

Here, we developed a methodology that uses a panel of urinary protein biomarkers to quantitatively monitor tumor growth in live orthotopic xenograft bearing mice. This method consists of a two-step approach. First, the concentrations of urinary biomarkers are quantified. Then, machine learning and principal component analysis (PCA) algorithms [20] are applied to analyze the urinary biomarkers, and subsequently, a score is assigned to indicate the tumor growth. More specifically, in this work, we used three groups of mice injected with low, medium, and high numbers of human-derived bladder cancer cells (UM-UC-5 cell line [21]) as the model system. Four protein bladder cancer biomarkers with high clinical or pathological significance were selected as a panel that included EGFR [22,23], HER2 [24,25], ADAM15 [26,27], and Survivin [18,28]. The biomarkers in the mouse urine were analyzed every week for four weeks using an automated microfluidic ELISA technology and the associated protocols developed in-house, which is able to rapidly and sensitively detect those biomarkers with only 8 μL of sample per marker and a detection limit down to a single-digit pico-gram per mL [29]. Then machine learning and PCA were performed with our 4-marker results, which revealed that the distribution of the PCA data points correlates well

with the bioluminescence imaging readings about the tumor burden. Mice with small tumors can be distinguished easily from those with large tumors. The tumor burden can be further quantified with a "tumor growth score" that is calculated based on the PCA results. Finally, our method was employed to study the *in vivo* therapeutic efficacy of an anti-tumor drug, dacomitinib, in the orthotopic xenograft mouse model.

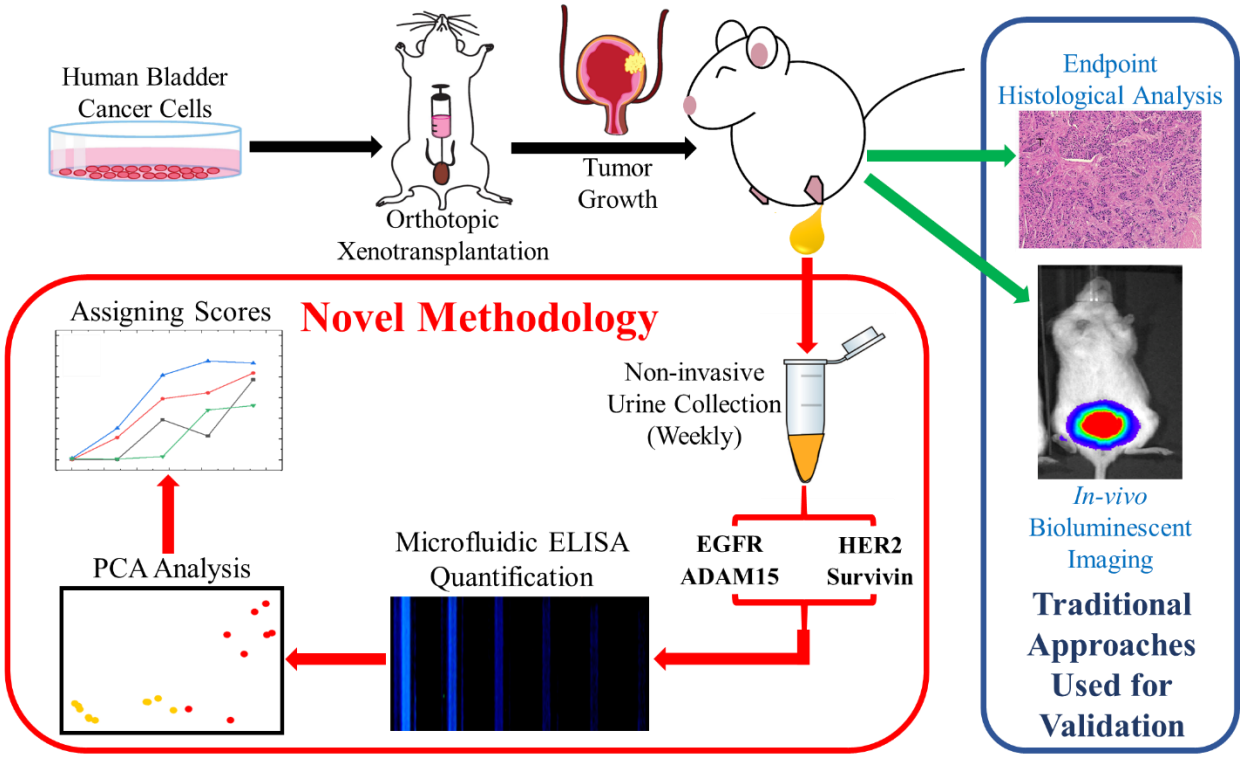

Figure 6.1. Illustration of the workflow. Bladder cancer was induced by injecting human-derived bladder cancer cells (UM-UC-5) into the bladders of immunodeficient mice. The tumor progresses in a 4-week period, during which, at least 50 µL of urine was collected once per week. A panel of four protein bladder cancer biomarkers (EGFR, HER2, ADAM15, and Survivin) in urine were selected to build the tumor growth model. An automated microfluidic chemiluminescent ELISA system and associated detection protocol developed in-house, which could complete an assay in about 45 minutes with only 8 µL of sample (per biomarker) and a detection limit down to a few pico-grams per mL, were employed to quantify the biomarkers' concentrations in urine weekly. Principal component analysis (PCA) was used to analyze the ELISA results for the four biomarkers and subsequently establish a quantitative tumor growth model. Concurrently, endpoint histological analysis and weekly in vivo bioluminescent imaging were performed to validate the effectiveness and accuracy of our methodology.

6.3. Experimental

6.3.1. Workflow

We designed a series of experiments to demonstrate the feasibility and to validate our method of urine-based tumor growth analysis. Various numbers of human-derived bladder cancer cells (UM-UC-5 cell line) were injected into the bladder lumens of NSG mice as previously described in Ref. [6] (see Fig. 6.1 for illustration). The UM-UC-5 cell line was previously engineered to express firefly luciferase and is capable of being used with luciferin-based bioluminescence imaging. The UM-UC-5 bladder tumor progresses gradually over a four-week surveillance period (as previously reported, spontaneous muscle invasion was observed by the end of the study). 50-80 µL of urine per mouse was collected once per week. The urinary concentrations for a panel of bladder cancer biomarkers were quantified via microfluidic ELISA. Using the concentration data of these biomarkers, a PCA analysis and subsequent score assigning was performed. To establish a correlation between the urinary "tumor growth score" and the actual tumor severity, we also performed concurrent tumor surveillance with traditional qualitative or semi-quantitative technologies such as endpoint histological analysis and weekly *in vivo* bioluminescent imaging (technology validation assays).

We selected four urinary biomarkers that are believed to be either strongly involved in tumor growth, muscle invasion or have high clinical relevance for cancer diagnostics. They are EGFR [22,23], HER2 [24,25], ADAM15 [26,27], and Survivin[15,16,28]. As reported in previously, the expression levels of all genes in the UM-UC-5 cell line was evaluated through mRNA sequencing [30]. Based on the mRNA expression data, the UM-UC-5 cell line was determine to has highly amplified expression of EGFR, normal-level expression of HER2 (*ERBB2* gene) and ADAM15, and relatively low expression of Survivin (*BIRC5* gene) [30]. The protein expression of these markers

were verified in the whole cell lysates of several bladder cancer cell lines through western blot. Since the UM-UC-5 cell line was collected from a female patient and has more consistent growth in the bladders of female mice, we chose to conduct this experiment with female NSG mice.

6.3.2. Microfluidic chemiluminescent ELISA

Having an accurate and sensitive biomarker quantification technology is critical to building a reliable tumor growth model that relies solely on urinary biomarker measurements. Although widely used in protein quantification, the traditional 96-well plate based ELISA is not capable of doing such measurements due to its large sample consumption per marker (50-100 μL) and relatively limited sensitivity [19]. The limitation of the traditional ELISA exacerbates for mouse urine (typically only 50-80 μL can be collected each time). Since the urinary concentrations of those bimarkers are expected to be low, a high-power dilution is not practically applicable.

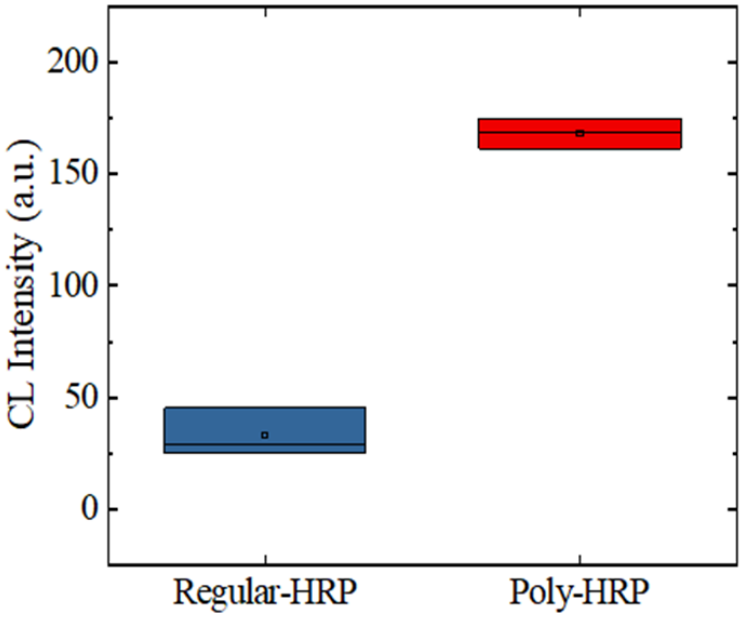

Figure 6.2. Signal amplification with streptavidin poly-HRP. Four groups of results were obtained in this experiment (BSA-biotin/regular-HRP, BSA-biotin/poly-HRP, PBS/regular-HRP and PBS/poly-HRP), each of which contains three capillaries. Both the regular-HRP and poly-HRP groups were observed to have background noise levels lower than 0.1. Therefore, the use of streptavidin poly-HRP can enhance the absolute signal and the signal-to-noise ratio 5-fold compared to those with the regular streptavidin HRP.

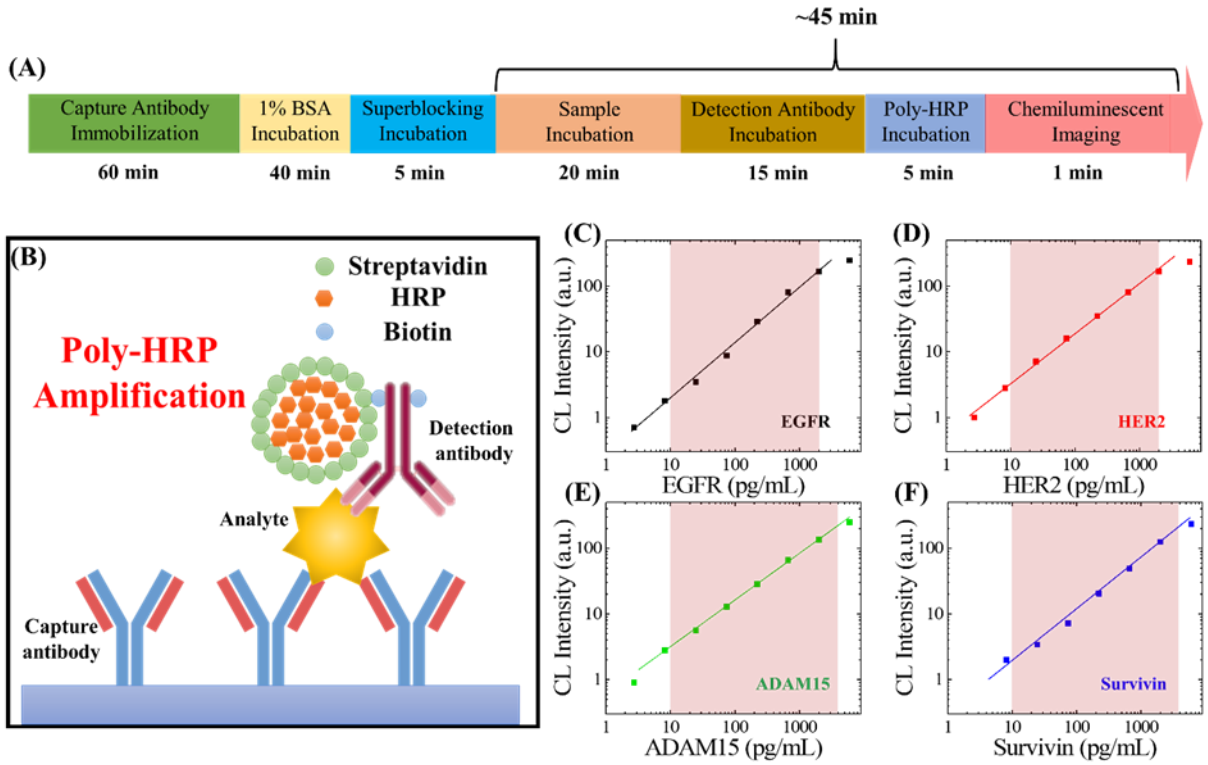

Figure 6.3. The highly-sensitive microfluidic chemiluminescent ELISA. (A) ELISA assay protocol for the four bladder cancer biomarkers. The first 105 minutes were used for ELISA sensor preparation (*i.e.*, capture antibody immobilization), which is usually done well in advance. The actual assay time was about 45 minutes, including a rinsing step (with 0.05% Tween) after each incubation step. (B) Illustration of the sandwich ELISA assay with poly-HRP amplification. The use of poly-HRP enhances the signal approximately five-fold, compared to regular HRP conjugated on the detection antibody. (C)-(F) Calibration curves for the four biomarkers with our microfluidic chemiluminescent ELISA. The dynamic range for all of the four biomarkers covers over three orders of magnitude. The respective LODs were 3 pg/mL for EGFR, 3 pg/mL for HER2, 5 pg/mL for ADAM15, and 8 pg/mL for Survivin (calculated by background +2.5 σ). The shaded areas denote the ranges used in the actual urine measurements, *i.e.*, 10-2000 pg/mL for EGFR, 10-2000 pg/mL for HER2, 10-4000 pg/mL for ADAM15, and 10-4000 pg/mL for Survivin. The solid lines are the linear fit in the log-log scale, within their dynamic ranges.

In this work, we employed microfluidic chemiluminescent ELISA technology developed in-house, which has much higher sensitivities and requires much smaller sample volumes (only 8 μL per biomarker) than the traditional 96-well plate-based ELISA. Detailed description of the microfluidic chemiluminescent ELISA and the disposable 12-channel cartridge can be found in our previous publication [29]. In addition, we employed streptavidin poly-HRP instead of standard

streptavidin-HRP to amplify the chemiluminescent signal [31,32]. Meanwhile, the corresponding blocking protocol was developed to suppress non-specific adsorption of poly-HRP to the sensor surface [33]. As a result, the signal-to-noise ratio was increased 5-fold over the previous protocol (Fig. 6.2). Excluding the sensor preparation (*i.e.*, capture antibody immobilization, which is usually done en-masse well in advance), the total assay time was about 45 minutes (Fig. 6.3(A)), much shorter than 4-5 hours usually used in 96-well-plate based ELISA.

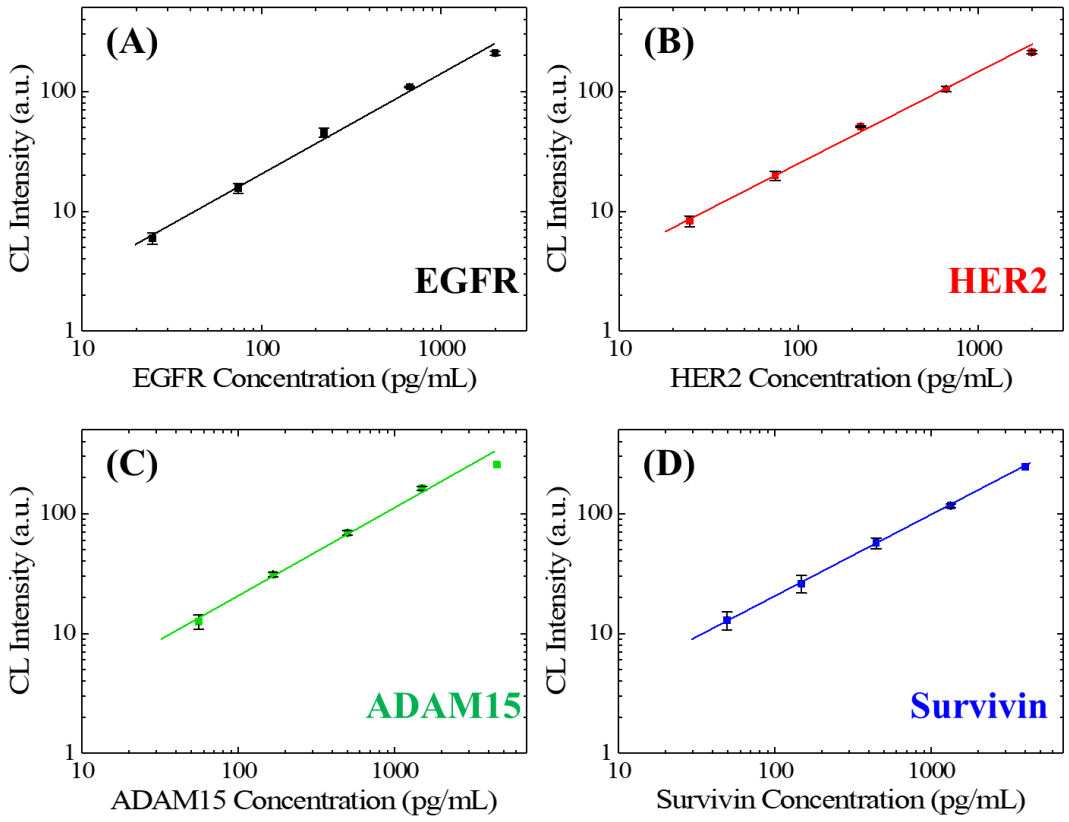

Figure 6.4. Calibration data points for the linear ranges (in the log-log scale) of the four biomarkers. The solid lines are the linear fits in the log-log scale. The error bars represent the intra-assay variances that were obtained from duplicated measurements. All intra-assay variances were close to or smaller than 10%.

We established calibration curves for the four bladder cancer biomarkers (Figs. 6.3(C)-(F)). The linear dynamic ranges in the log-log scale are 3-2000 pg/mL, 3-2000 pg/mL, 5-4000 pg/mL, and 8-6000 pg/mL for EGFR, HER2, ADAM15, and Survivin, respectively (the lower LOD is calculated by background +2.5 σ), which cover approximately three orders of magnitude. The

intra-assay variance is close to or smaller than 10% (Fig. 6.4). In contrast, the dynamic ranges with plate based ELISA (from user's manual of the kits) are 31-2000 pg/mL, 55-3500 pg/mL, 63-4000 pg/mL, and 63-4000 pg/mL for EGFR, HER2, ADAM15, and Survivin, respectively [34-37]. The calibration curves demonstrated significantly improved sensitivity over traditional plate-based ELISA, even with the same antibodies. The performance introduced above can fully support the detection ranges that were used in the actual urine measurements, *i.e.*, 10-2000 pg/mL for EGFR, 10-2000 pg/mL for HER2, 10-4000 pg/mL for ADAM15, and 10-4000 pg/mL for Survivin. To ensure the measurement reliability, the lower ends of the dynamic ranges (below 10 pg/mL) were not used for actual urine measurements and were marked as 0 pg/mL.

6.4. Results

6.4.1. Converting the ELISA measurements to a PCA model

With the microfluidic chemiluminescent ELISA technology described in Section 2, we performed the actual animal studies and converted the biomarker results into a PCA model. We injected a group of mice with a low number of UM-UC-5 cells (marked as low number group), along with a tumor-free control group. Those mice serve as the "training set" for the subsequent studies using medium and high UM-UC-5 cell numbers. To be specific, 0.5 million UM-UC-5 bladder cancer cells were injected into the bladder lumens of the four experimental mice (L1-L4) on Day 0. For the sham (control) mouse, a buffer solution without cells was injected into one sham mouse (Fig. 6.5). The urinary protein concentrations were measured for the four biomarkers at different time points after tumor inoculation (Figs. 6.5(A)-(D)). Note that for EGFR measurements, the urine samples were diluted three times with 1% BSA in PBS. For HER2, ADAM15, and Survivin measurements, the urine samples were diluted two times with 1% BSA in PBS.

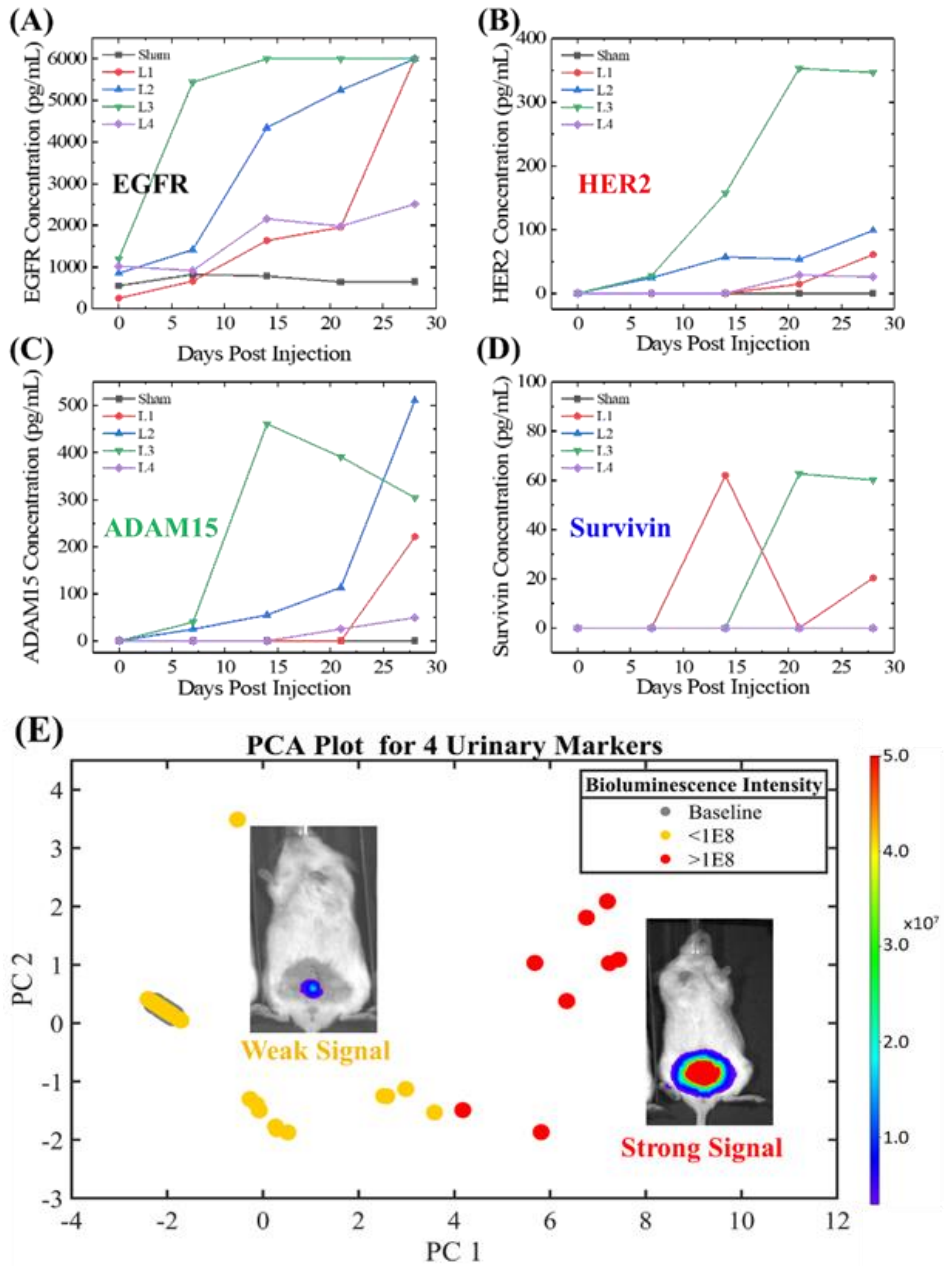

Figure 6.5. Converting urinary biomarker concentrations to a PCA model. (A)-(D) Urinary concentrations of the four biomarkers in five mice over 4 weeks. A low number of 0.5 million UM-UC-5 (luciferase positive) bladder cancer cells were injected into the bladder lumens of the four experimental mice (L1-L4) on day 0. Buffer solution without cells was injected into the sham mice. The "plateau" in the EGFR readouts was caused by the measurement that exceeded the upper limit of the detection range. (E) PCA plot generated based on the urinary biomarker concentrations in (A)-(D). The distribution of the data points correlates well with the bioluminescent imaging readings (see the insets for example) about the tumor size (See the scale bar for the correlation between colors and bioluminescent intensities). The mice used here serve as the training set for all subsequent experiments and PCA analyses. The corresponding calculation algorithms will be used to analyze data in the remaining "testing" sets of experiments. Note that the baseline is clustered around the coordinates (-2, 0.2) on the PCA plot.

As we presented in Figs. 6.5(A)-(D), the urinary concentrations of the biomarkers generally have increasing trends with some fluctuations. Due to 3% cross-reactivity between human EGFR and mouse EGFR (according to the ELISA kit's user manual) there were some background readings for EGFR, even before the tumor inoculation. The typical background readings at Week 0 for EGFR (equivalent human EGFR concentration) were between 200 and 1000 pg/mL. The "plateau" in the EGFR readouts was resultant from measurement that exceeded the upper limit of detection. All measurements that exceeded the detection limit were marked as the upper LOD ($2000 \times 3 = 6000$ pg/mL). For HER2 and ADAM15, no background signal was observed at Week 0 and the urinary concentration readouts increased from nearly 0 pg/mL to 50-400 pg/mL by the end of week 4. For Survivin, no background signal was observed at Week 0, but due to the relatively low protein expression level, low readouts (<100 pg/mL) were observed from two of the four mice in the following weeks. The increase in urinary biomarker concentrations is typically higher than two orders of magnitude (especially for HER2, ADAM15, and Survivin), which suggests that a creatinine-based urine concentration normalization is not necessarily required (the distribution of creatinine levels for all samples is within an order of magnitude).

PCA analysis was performed with the biomarker concentration data collected from the ELISA measurements (Fig. 6.5(E)). The data points from the mice with lower bioluminescence readouts ($< 1 \times 10^8$) were represented by yellow dots and the data points from mice with higher bioluminescence readings ($> 1 \times 10^8$) were represented by red dots. The data points were clustered into two distinct groups, which means that the urine-based PCA results correlates well with the bioluminescence imaging readings about the tumor load (see the insets for example). The PC1 and PC2 components account for 84.1% and 9.0% of the variability (weights), respectively. The eigenvalues were calculated for all four PC scores (Fig. 6.6). The baseline data points (before

the tumor was injected and the sham animal) are all clustered around (-2, 0.2). The data points that correlate with the mice with high bioluminescence intensity readouts ($>1 \times 10^8$) are all distributed in the right half of this two-dimensional plot (i.e., PC1>4). Most importantly, the mice with relatively low bioluminescence intensity readouts can be easily distinguished from the mice with relatively high bioluminescence intensity readouts.

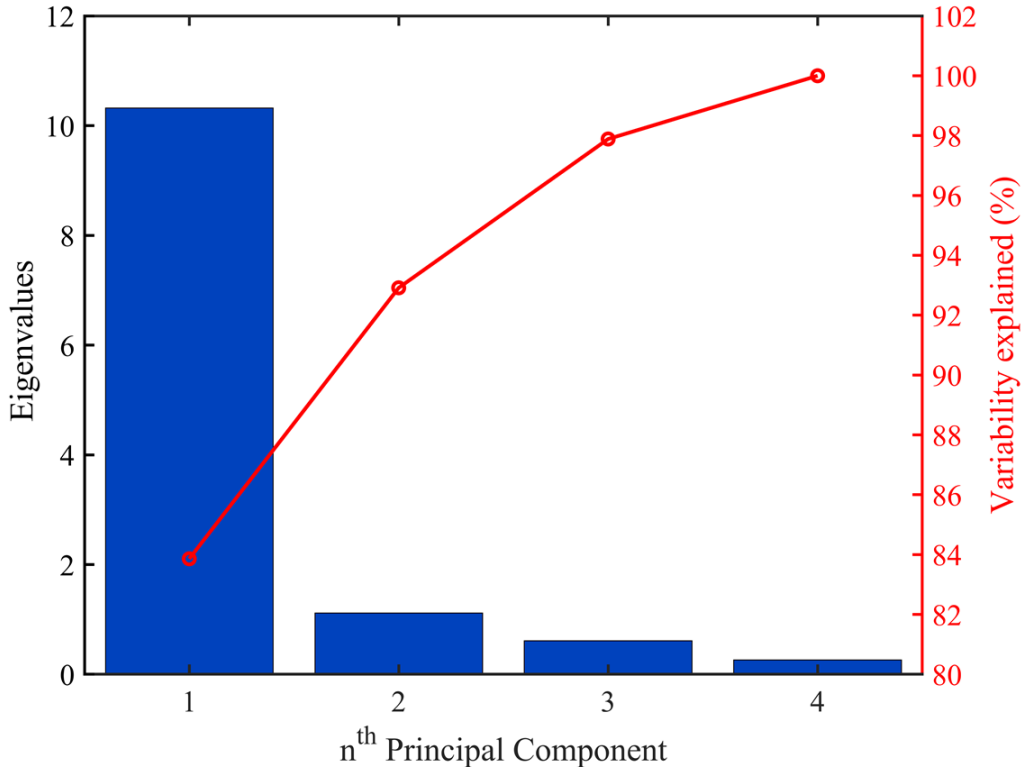

Figure 6.6. The eigenvalues for the four PC scores are 10.32, 1.11, 0.61, and 0.23, respectively. Which means the four PC scores can account for 84.1 %, 9.0%, 5.0%, and 1.9% of the variabilities, respectively. Based on the eigenvalue, 93% variability was accounted for with the first two PCs.

6.4.2. Testing sets

After successfully modeling the training set (*i.e.*, the mice injected with a low number of initial cancer cells) with PCA, we investigated two more groups of mice with a medium number (1 million) and a high number (1.5 million) of UM-UC-5 cancer cells injected into mouse bladders,

which serve as the testing sets. Same as the training set, urine was collected weekly and the urinary biomarker concentrations were quantified via microfluidic chemiluminescent ELISA.

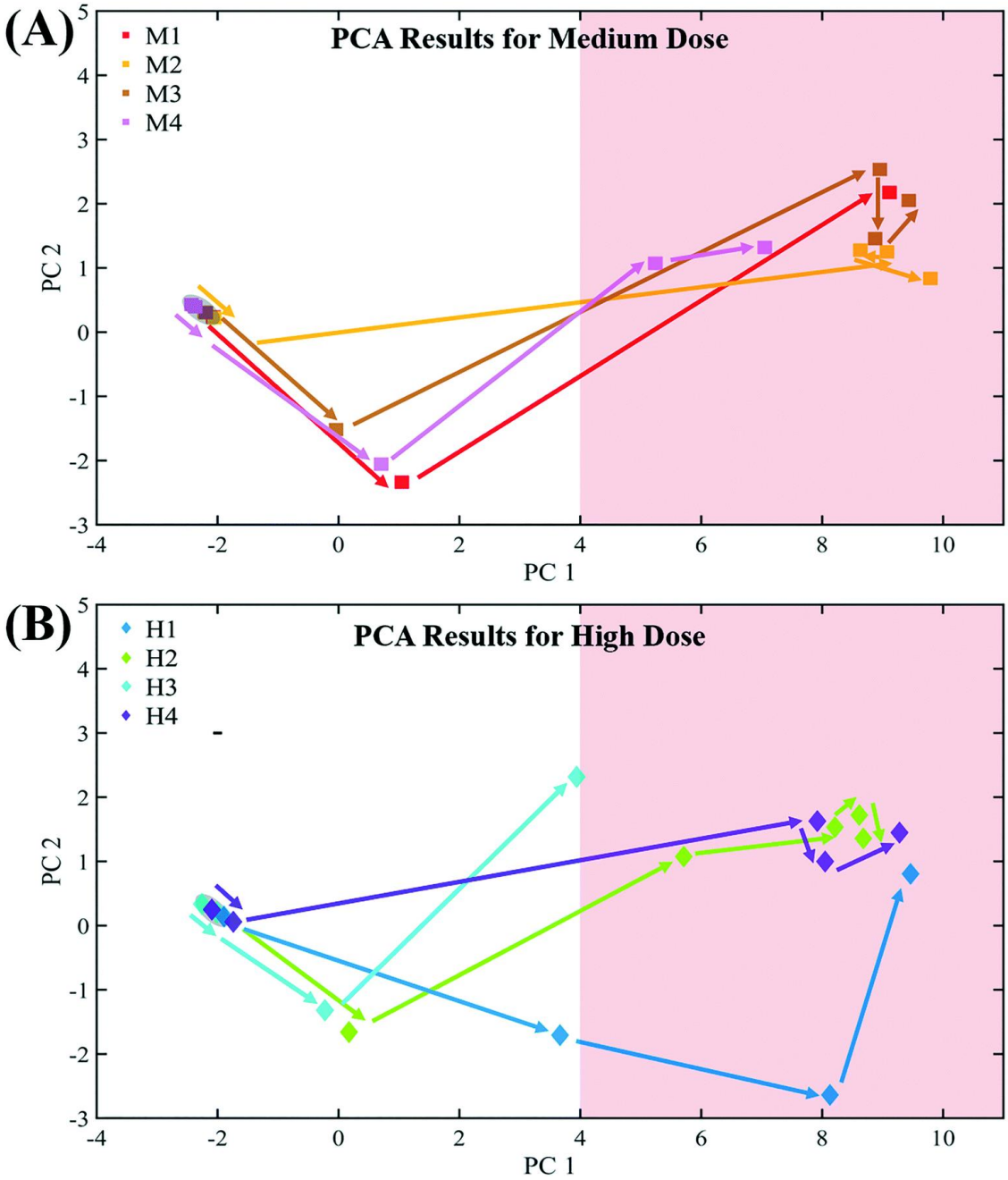

Figure 6.7. Trajectories of the mice on a PCA plots indicated by arrows during the 4-week urine measurements. These mice were injected with a medium number of 1 million UM-UC-5 cells (A) and a high number of 1.5 million UM-UC-5 cells (B) and they serve as the testing sets using the PCA parameters obtained in Fig. 3(E). They all started from the baseline around (-2, 0.2) on the PCA plot and progressed towards the large tumor region denoted by the shaded area. Note that Mouse M1 and H2 were euthanized before the 4 week end point due to tumor burden.

The PCA results from these two groups were generated with the same algorithm and parameters that were used for PCA analysis of the training set. We included trajectories on the PCA plots for individual animals in order to visualize tumor growth (Fig. 6.7). Similar to the training set, the trajectories for the testing sets all started from the baseline region around (-2, 0.2) in the PCA plot and progressed towards the large tumor region denoted by the red shaded area. Note that Mouse M1 and H2 died before the 4-week post-tumor-injection endpoint. The similarities between the PCA results in the training set and the testing sets suggest that this tumor growth model is valid over a range of injected UM-UC-5 cancer cell numbers (0.5-1.5 million).

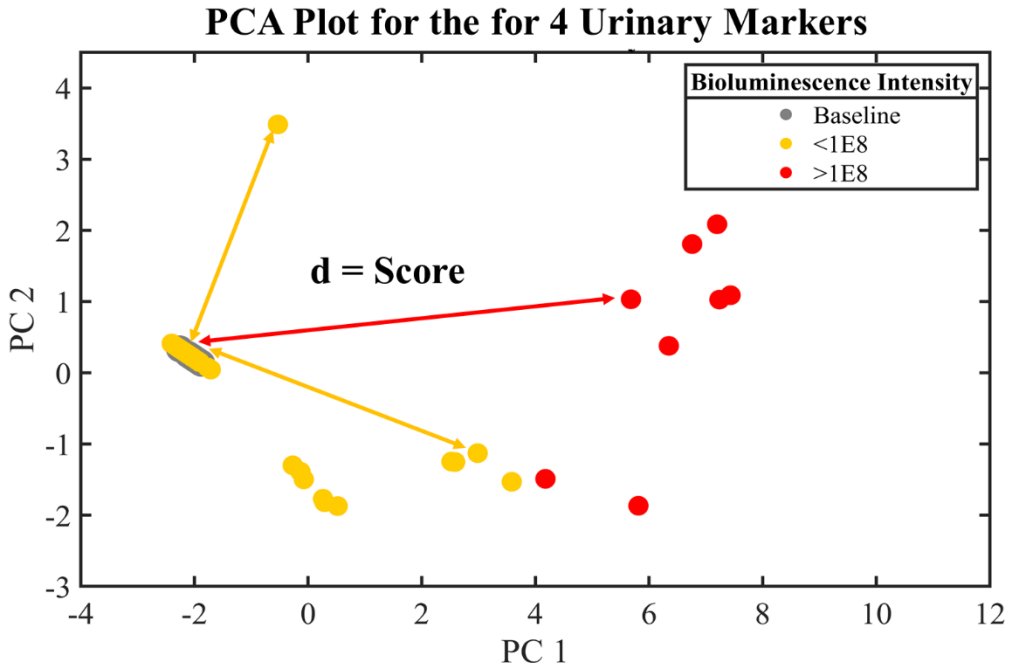

Figure 6.8. The "tumor growth score" is calculated as the distance from the point in the PCA plot and the averaged baseline point centered around (-2, 0.2).

6.4.3. Quantifying tumor growth with a urine-based "tumor growth score"

To provide a direct and quantitative assessment of tumor growth, this two-dimensional PCA model is subsequently transformed into a one-dimensional system -- "tumor growth score", which is calculated as the distance between a particular point in the PCA plot and the averaged

baseline point centered around (-2, 0.2) (Fig. 6.8). The tumor growth scores were calculated for mice with low, medium, and high injected cell quantities at each time point (Figs. 6.9(A)-(C)).

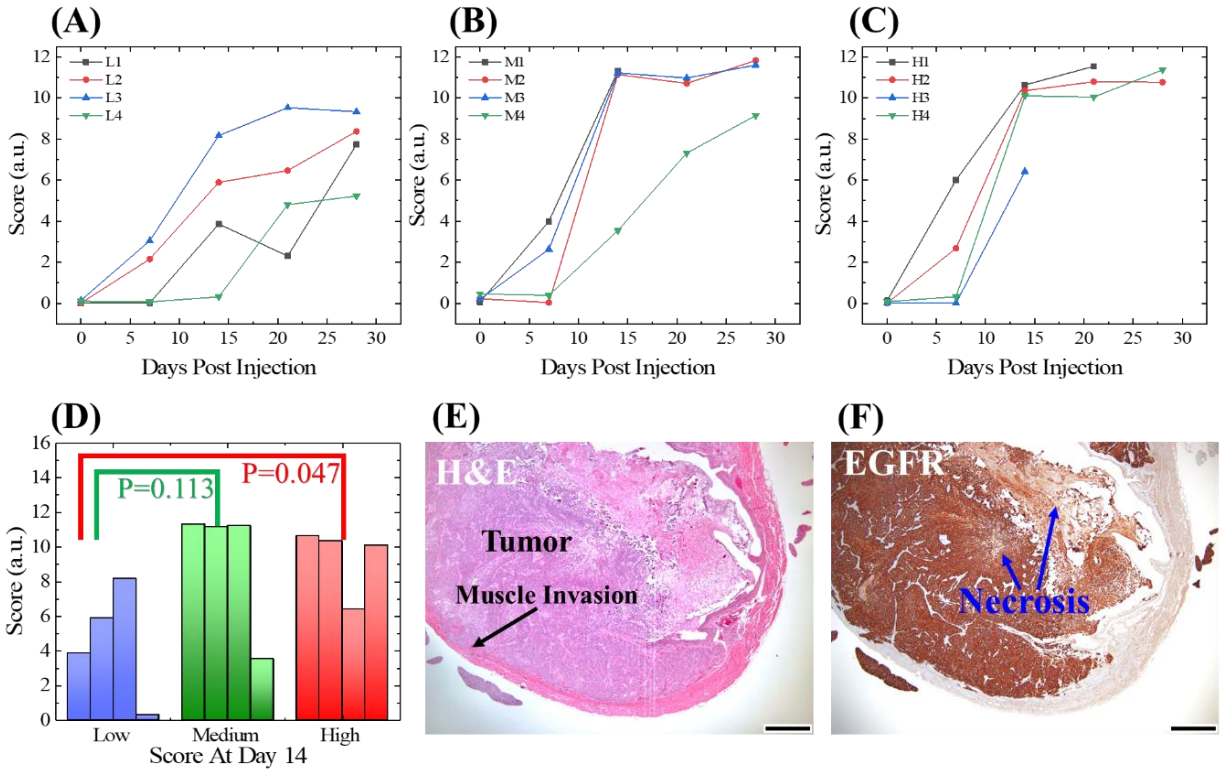

Figure 6.9. Quantifying tumor growth with PCA scores and endpoint histology. (A)-(C) Quantification of tumor growth using the scores obtained on the PCA plot for low, medium, and high numbers of initially injected of UM-UC-5 cells. (D) Comparison of the scores on day 14 for the mice that had received low, medium, and high initial cancer cell numbers. (E)-(F) Endpoint histological slides with H&E staining and EGFR immunohistochemistry staining for a representative "large" orthotopic bladder xenograft. Muscle invasion can be found by the bottom-left corner of the cross-section. Tumors at this stage usually have relatively low surface-to-volume ratios and multiple necrotic centers. The scale bars stand for 0.5 mm.

During the four weeks of tumor growth, the scores from the mice in all three groups show clear increasing trends (increased from around 0 to a range between 5 and 12). The slopes for the "low number" group are the lowest among the three groups. In addition, lower initial cancer cell numbers are beneficial for the mouse's survival with tumor as deaths were observed in both the medium and high number groups before study completion. The increasing trend of the score for the first week may not be very significant for half of the mice (6 out of 12) but the score for the

second week are significantly higher than the baseline points for all mice ($p = 0.037$, 0.003, and 0.00008 for low, medium, and high number groups, respectively). This indicates that although the initially injected UM-UC-5 cell quantities are the same for all mice within each group, the uptake rates for the cancer cells may be significantly different from mouse to mouse. The scores for most of the mice reached "plateaus" after the second week in the medium and high number groups. Therefore, a comparison was performed between the scores for each group at the second week (Fig. 6.9(D)). The scores from the high number group have statistically significant differences from those from the low number group ($p=0.047$). The scores from the medium number group were also higher than the scores for the low number group but the differences do not have statistical significance ($p=0.113$) (due to the outlier M4). The scores from the medium and high number groups appear to be very similar ($p=0.974$). This demonstrates that our "tumor growth score" can quantitatively reflect the orthotopic growth of the inoculated tumors, until they reach a very severe stage.

The "plateau" that appears in the medium and high number groups can be explained by the following conjecture. Once tumors fill the bladder lumen, the surface-to-volume ratio becomes smaller and the tumor may grow outward impairing cellular diffusion within the bladder. After the tumors reach a certain volume, the center of the tumor may become necrotic due to a lack of nutrients. Both of these problems will inhibit the urinary concentration of the biomarkers from increasing. This hypothesis is supported by the endpoint histological slides where one representative mouse presented with a necrotic tumor (Figs. 6.9(E) and (F), collected from mouse L1). Tumors at this stage usually have relatively low surface-to-volume ratios and showed multiple necrotic areas (Fig. 6.10).

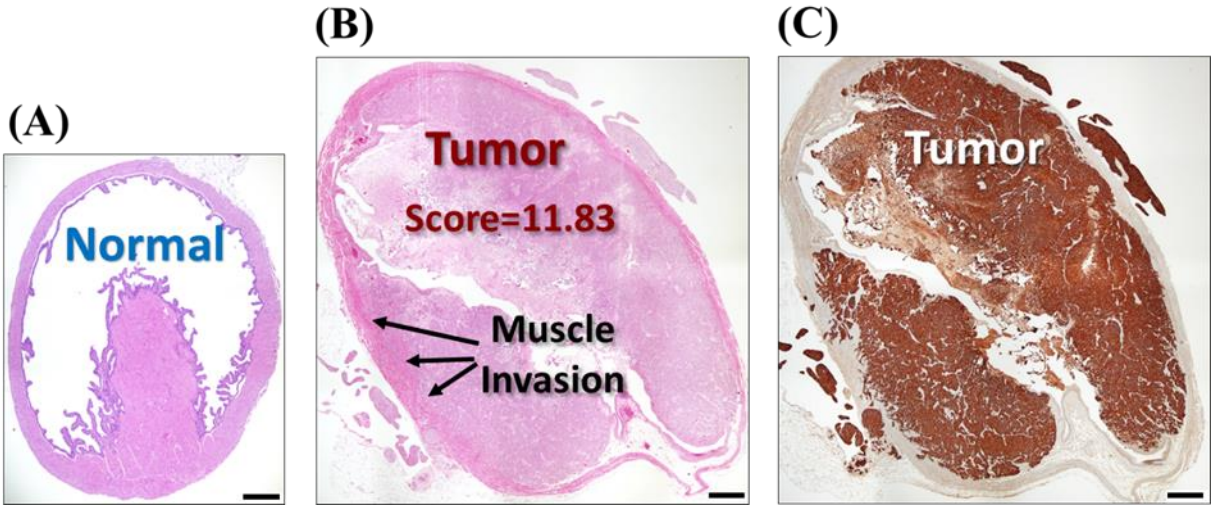

Figure 6.10. Histology slides for a normal mouse bladder and a mouse bladder filled with human tumor (from mouse M2). (A) H&E staining for the cross-section of a normal mouse bladder without tumor. (B) H&E staining for the cross section of mouse M2's bladder. Muscle invasion can be found on the left edge of the cross-section image. The corresponding tumor growth score is 11.83. (C) EGFR immunohistochemistry staining for the cross section of mouse M2's bladder. The bladder lumen was almost filled with tumor and the tumor appeared to be very thick. In addition, the bladder with tumor has significantly larger size than the normal bladder. All scale bars: 0.5 mm.

6.4.4. *In vivo* dacomitinib therapeutic efficacy study

The UM-UC-5 cell line has an increased copy number of EGFR, which is a target of many anti-cancer therapeutics. Dacomitinib, as a second-generation irreversible inhibitor of the EGFR family, was recently approved by US FDA for the therapy of EGFR positive metastatic non-small cell lung cancer [38]. The *in vitro* inhibitory efficacy of dacomitinib for human bladder cancer cell lines was studied and reported by our previous research [21]. UM-UC-5, along with other bladder cancer cell lines, appeared to be sensitive to dacomitinib treatment (IC50 <5 μM) [21]. *In vivo* therapeutic efficacy tests for dacomitinib were also performed with UM-UC-6 and UM-UC-9 cell lines with conventional evaluation methodologies [39]. However, the *in vivo* therapeutic efficacy of dacomitinib in treating UM-UC-5 orthotopic xenografts have not yet been investigated.

With the establishment of this non-invasive and quantitative methodology for the

surveillance of orthotopic tumor growth, we conducted a pilot experiment regarding the *in vivo* therapeutic efficacy of dacomitinib with a group of four animals. Half-a-million UM-UC-5 cells (the same number used in the low number group) were injected into four NSG mice (D1-D4) due to the relatively mild growth rate (Fig. 6.9). Dacomitinib was administered to the mice between the first week (Day 7) and the fourth week (Day 28). Nine doses of dacomitinib by oral gavage at approximately 15 mg/kg every other day during this three-week treatment.

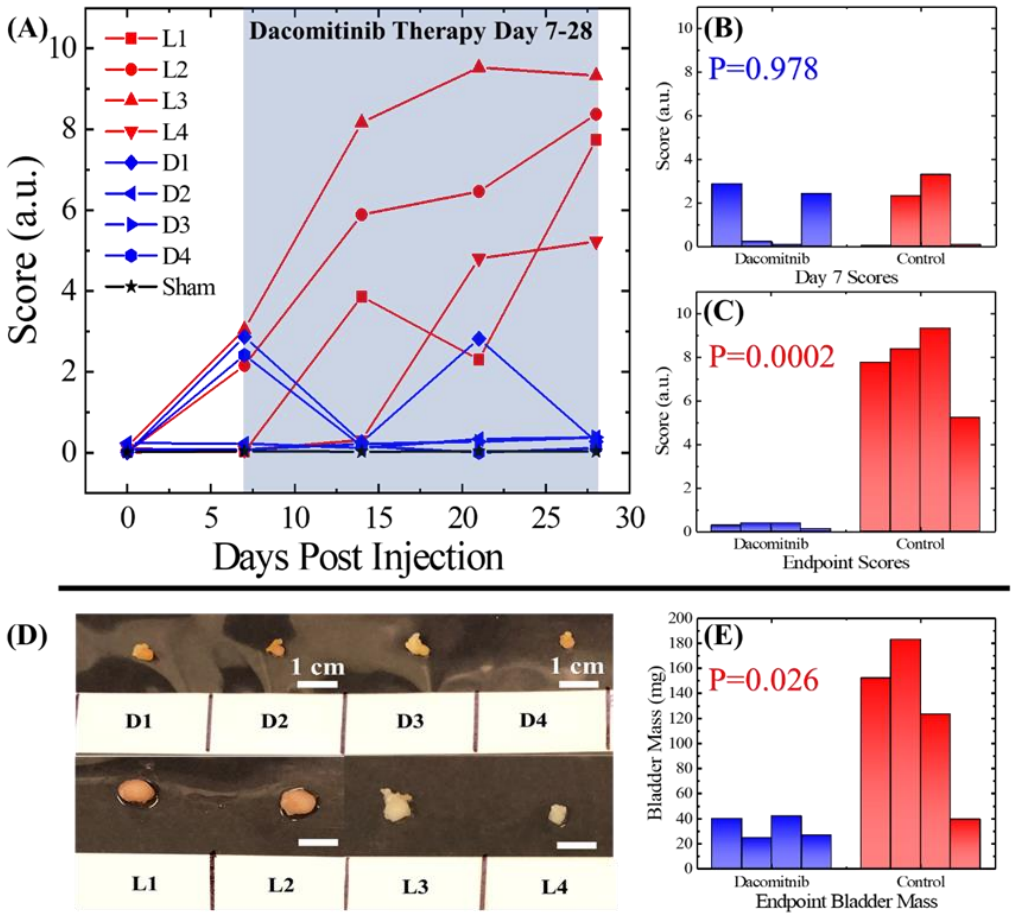

Figure 6.11. Urine-based tumor growth quantification for an in vivo dacomitinib study. (A) Tumor growth scores for animals with (D1-D4) and without (L1-L4) dacomitinib treatment, between day 0 and day 28. Dacomitinib treatment was performed between day 7 and day 28. The scores for the sham mouse are also plotted. (B) Score comparison between the treated and control groups on day 7. No significant difference was observed. (C) Score comparison between treated and control groups on day 28. The scores from the control group were significantly higher than the dacomitinib treated group. (D)-(E) Result evaluation and validation. (D) The photos for the bladders with or without dacomitinib treatment. (E) Endpoint bladder mass comparison for both the dacomitinib treated and control groups.

Weekly urine collection was performed for four weeks. The urinary biomarker concentrations were measured, the PCA model was applied, and the tumor growth scores were calculated for these four mice in the same manner as our earlier sets. The scores for these four animals were plotted together with the scores for the low number group and the sham control mouse. The scores for the mice in the dacomitinib group stopped increasing after Day 7 which is when the treatment began (Fig. 6.11(A)). Although some fluctuation was observed for mouse D1, the scores for all of the mice in this group ended up at very low levels by the end of the experiment (Day 28).

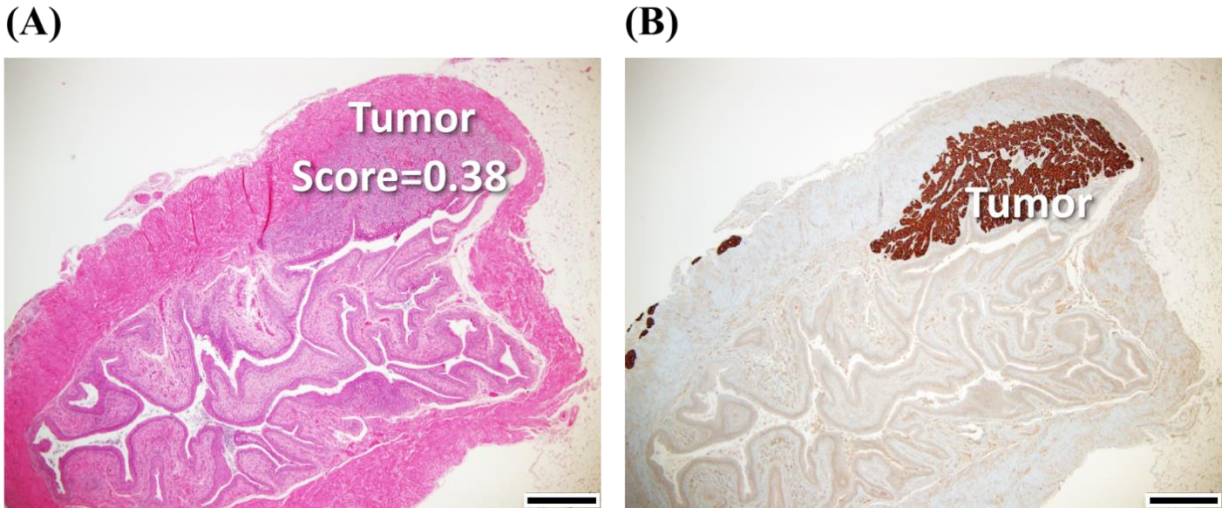

Figure 6.12. Histology slides for a mouse bladder with tumor, after three weeks of Dacomitinib treatment. (A) H&E staining for the cross-section of mouse D2's bladder. The corresponding tumor growth score for this bladder is 0.38. (C) EGFR immunohistochemistry staining for the cross section of mouse D2's bladder. The tumor appeared to be small and loose.

Side-by-side comparisons were performed for the scores on Day 7 (before the dacomitinib treatment started) and Day 28 (endpoint), between the dacomitinib group and the control group (low initial cancer cell number without drug treatment). As presented in Fig. 6.11(B), no significant difference can be observed for the scores on day 7 ($p=0.978$). In contrast, by the end of the experiment the difference between the two groups became very large and significant

(p=0.0002), as shown in Fig. 6.11(C). The results of the urinary measurements indicate that the dacomitinib treatment was effective in this *in vivo* test. We also used traditional examination methods to weigh the bladders and perform IHC. The bladder weights were significantly lower in the dacomitinib treated group (Figs. 6.11(D)-(E)), which corroborates our PCA finding that dacomitinib was efficacious in this model. The mice that received dacomitinib treatment appeared to have smaller and less "dense" tumors when comparing the IHC from each group (Fig. 6.12).

6.5. Discussion and conclusion

In this work, we have successfully developed a non-invasive, multiparameter urine-based biomolecular prognostic technology for bladder cancer orthotopic xenograft mouse model, which provides an alternative tumor surveillance approach for the labs that do not have connections to those *in vivo* imaging facilities (for bioluminescence imaging PET-CT and MRI) and skilled operators (for ultrasound imaging). While developing this method, we quantitatively monitored the growth of orthotopic bladder cancer xenografts that were induced by different initial cancer cell numbers across a four-week period. We also conducted a pilot experiment that utilized this method for real-time surveillance of the *in vivo* therapeutic efficacy of dacomitinib.

Our results indicate that the model, built with multiple biomarkers, will lead to several unique advantages over single-parameter models. First, the background readings (noise) for a single biomarker (caused by cross-reactivity) were greatly reduced or even eliminated. (See Fig. 6.13 for tumor growth scores with EGFR only and EGFR+HER2). Second, the saturation in a single biomarker's measurement will not stop the progression in the model as the increment in the readings of other biomarkers will dominate the progression in the model. Third, the selection of biomarkers with significantly different expression levels makes this modeling methodology

broadly applicable to other human bladder cancer cell lines. Recalibration of the biomarker selection may be necessary depending on the protein expression patterns of the desired cell line, but this is easily performed. However, as a proof-of concept study, we did not aim to include all markers that involved in bladder cancer's progression and invasion. Incorporating additional markers (e.g., FGFR3 and EpCAM for tumor growth and CXCL1 for muscle invasion) may be potentially beneficial for the universality of this model [40-43].

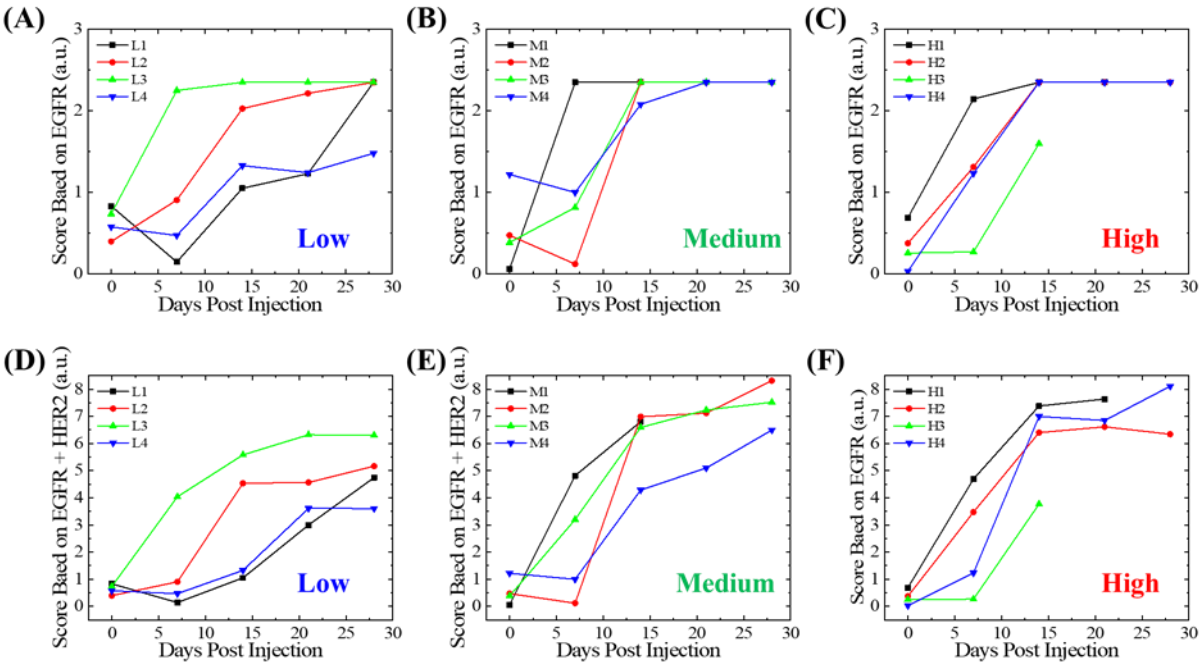

Figure 6.13. Tumor growth scores based on urinary EGFR only ((A)-(C)) and EGFR+HER2 ((D)-(E)). (A)-(C). The tumor growth scores based on urinary EGFR concentrations. Each point represents the absolute distance (values are all positive) between each measurement and the grand averaged background. The background variance at day 0 is very obvious for all groups. (D)-(F). The tumor growth scores based on urinary EGFR and HER2 concentrations. The noises at day 0 are significantly improved but still not as good as the four-marker model.

The development of this methodology also facilitated the optimization of the number of cancer cells for orthotopic injection. As the scores presented in Figs. 6.9 (A)-(C), out of the three initial cancer cell numbers that were tested in this study, the "low number" group appears to have the shallowest increasing trend of tumor growth scores out of the three groups (while having a large endpoint tumor size) which is an essential for an animal model that is expecting to have a

long survival time after tumor inoculation. The variation in tumor growth rates that were caused by different initial numbers of UM-UC-5 cells was observed and reported for the first time because such optimization is difficult to perform without a reliable quantitative tumor surveillance technology.

In addition to the animal model itself, our work also demonstrated strong potential in facilitating *in vivo* drug efficacy modeling in live animals. With our methodology, the necessity of luciferase transfection for patient-derived tumor cell lines can be reduced. This is especially beneficial for researches with patient-derived-xenograft models, as the tumor growth can be monitored through urine measurements. It can ultimately lead to an enhancement in the throughput for and cost performance in personalized precision medicine therapies in clinical settings.

With all the aforementioned features, the same modeling concept can easily be applied to other bladder cancer cell lines and adapted for other types of bladder cancer animal models. Carcinogen-based mouse models, syngeneic models, and PDX models[44,45], could all benefit from a new approach to quantifying tumor burden in mice. Furthermore, this urine-based methodology should be applicable to research with other types of urinary system carcinomas, such as renal cell carcinoma and prostatic carcinoma [46-49].

Although we have demonstrated very promising results for the surveillance of orthotopic tumor growth, there are many avenues for this method to progress. The trends for the urine measurements shortly after the introduction of dacomitinib are still unknown. To find out the exact "bifurcation point" between the treated and control groups, more data points can be added between week one and week two. Such intensified data points are also beneficial for investigating the tumor growth rate during the earlier stages of xenograft development.

As mentioned in the "Result" section, the change in biomarker concentrations was typically higher than two orders of magnitudes, thus the necessity for performing creatinine-based urine concentration normalization was reduced. However, such normalization may still be helpful for the measurements with the urine collected from animals with larger tumors because their urine generally appeared to be more diluted (caused by unknown reasons). Such normalization will likely make the "plateau" levels in the score shift to higher values and appear at later time points.

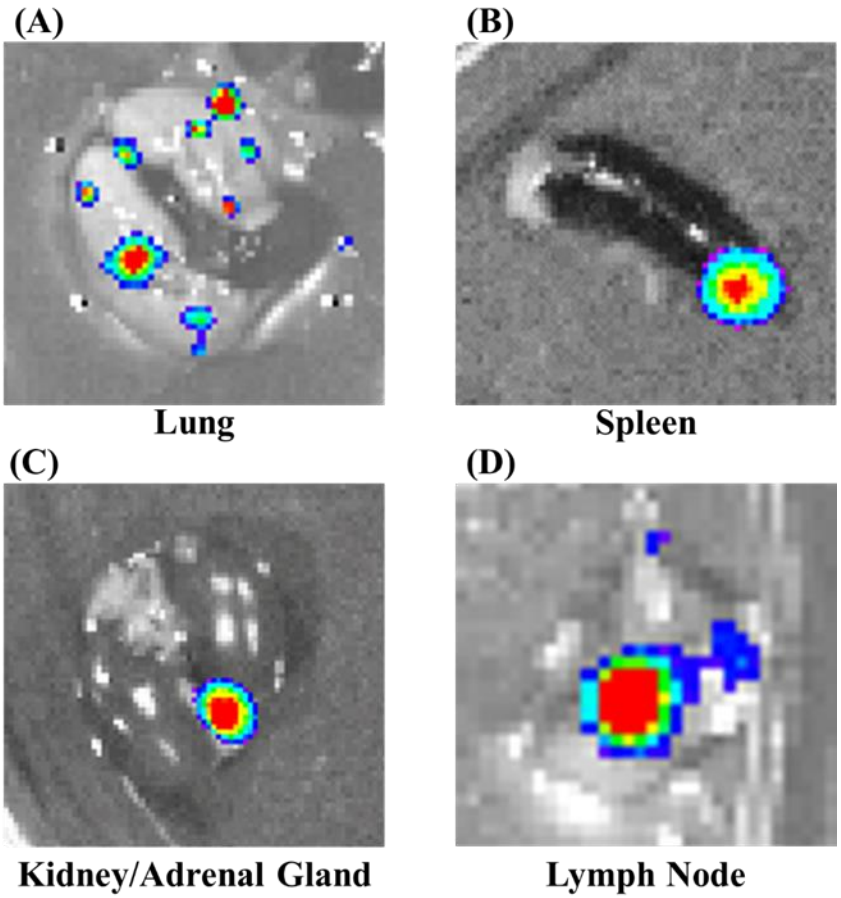

Figure 6.14. Bioluminescence images for metastasis at distant organs. Human bladder cancer cells were observed in lung, spleen, kidney/adrenal gland and lymph nodes. Subfigure (A) was collected from mouse L2's lung; (B) was collected from mouse M3's spleen. (C) was collected from mouse M4's kidney/adrenal gland and (D) was collected from mouse L1's lymph node. The subfigures were not on the same scale.

According to our previous research, local muscle invasion and distant metastasis typically occur by the fourth week and such metastasis was also observed by bioluminescence in these

experiments (Fig. 6.14). However, our current urine-based model is not capable of quantitatively monitoring the tumor invasion or metastasis after the tumors grow over the entire inner surface of the bladder. This limitation may be addressed by introducing more metastasis and invasion-related urinary markers (including protein, exosome and micro-RNA markers) into this model [50-56].

6.6. Materials & Methods

6.6.1. Cell lines

The UM-UC-5, UM-UC-15, and UM-UC-18 cell lines were obtained from their originator, Dr. H. Barton Grossman of the MD Anderson Cancer Center (Houston, TX). Cells were cultured in Dulbecco's Modified Eagle Medium (HyClone) supplemented with 8% fetal bovine serum (HyClone), 1% penicillin-streptomycin-Fungizone (Lonza BioWhittaker), and 2 mM GlutaMAX (Gibco). Cells were grown in a humidified incubation chamber at 5% CO2 and 37°C. Cell line authenticity was verified by analysis of short tandem repeats (IDEXX Bioanalytics) and lines were determined mycoplasma free by PlasmoTest (InvivoGen).

6.6.2. Orthotopic bladder xenografts and dacomitinib treatment

NOD.*Cg-Prkdc*^{scid}*Il2rg*^{tm1Wjl}/SzJ (NSG^{TM}) mice were obtained from the Unit for Laboratory Animal Medicine Breeding Colony at the University of Michigan. Female NSG mice between the age of 3 to 6 months were given orthotopic bladder xenografts as previously described (PMID: 30683938)[6]. One week after xenograft implantation, a group of female mice (N = 4) were given nine doses of dacomitinib by oral gavage at 15 mg/kg approximately every other day for three weeks. To measure bioluminescent signal, mice were given an IP injection of 3 mg D-Luciferin (Regis Technologies) and after 10 minutes, signals were measured using an IVIS 200

Spectrum (Perkin Elmer). Bioluminescent signals coming from the bladder were measured by setting the minimum counts to 600 and using Living Image's "Auto ROI" feature with a 25% threshold. Mice were euthanized after 4 weeks post-xenograft-implantation. All animal studies were approved by the University of Michigan Institutional Animal Care and Use Committee.

6.6.3. Urine collection

Mice were placed in a sterile empty cage without bedding. The cages were checked for urine in 10 minute intervals for a maximum of 30 minutes. Urine was immediately transferred to centrifuge tubes on ice and then stored at 4°C throughout the day (until at least 50 µL of urine was collected). If insufficient urine was collected, the process was repeated approximately 2 hours later.

6.6.4. Pre-ELISA treatment of urine

Urine samples were spun for 30 seconds with 10,000 x g to remove the insoluble fractions in the urine. The supernatant was collected with clean microcentrifuge tubes and the pellets were discarded. The centrifuged urine samples were stored at 4°C before taking ELISA measurements. The storing periods were typically less than three days.

6.6.5. Western blotting

Cells were washed with PBS, harvested by cell scraping, and then pelleted by centrifugation at 4 °C, 9,300 x g for 5 minutes. Cell pellets were frozen at -80°C. These pellets were then lysed in RIPA buffer (PMID: 18434311[57]) for 1 hour on ice with intermittent vortexing. The lysed cells were then centrifuged at 4°C, 13,200 x g for 8 minutes, supernatants were collected and quantified with the Bradford protein assay (Bio-Rad) [57]. Gel electrophoresis was performed

using equal amounts of protein on 4-20% Tris-Glycine gels, WedgeWell format (Novex). A wet transfer was used to move proteins from the gel to an Immobilon-FL PVDF membrane (Millipore), blocked with non-fat dry milk, and then incubated with primary antibody overnight at 4°C followed by 1 hour at room temperature. The primary antibodies were anti-ADAM15 (NovoPro, 101503), anti-EGFR (ThermoFisher Scientific, H9B4), anti-GAPDH (Invitrogen, GA1R), anti-HER2 (Abcam, EP1045Y), and anti-Survivin (R&D Systems, 91630). Fluorescent secondary antibodies included IRDye 680LT goat anti-mouse and IRDye 800CW goat anti-rabbit (LI-COR). Blots were scanned using the Odyssey CLx (LI-COR) and analyzed using Image Studio v3.1.

6.6.6. ELISA reagents

The ELISA kits for human EGFR, HER2, ADAM15, and Survivin were all purchased from R&D systems. The catalog numbers are DY231(EGFR), DY1129B(HER2), DY935(ADAM15) and DYC647-5(Survivin), respectively. Note that the kits for EGFR and ADAM15 recognize the extracellular domains of the respective targeting proteins. The working solutions of the antibodies were prepared at the following concentrations: 4 μg/mL for EGFR capture antibody, 1 μg/mL for EGFR detection antibody, 10 μg/mL for HER2 capture antibody, 0.5 μg/mL for HER2 detection antibody, 20 μg/mL for ADAM15 capture antibody, 0.3 μg/mL for ADAM15 detection antibody, 2 μg/mL for Survivin capture antibody and 0.72 μg/mL for Survivin detection antibody. The working solutions of all capture antibodies were prepared with 1x PBS and the working solutions for all detection antibodies were prepared with 1x reagent diluent.

The ELISA coating buffer (1x PBS, DY006), concentrated wash buffer (WA126), concentrated streptavidin regular-HRP (DY998) and concentrated reagent diluent (10% BSA in 10× PBS, DY995) were purchased from R&D Systems. The working solution of the wash buffer

and reagent diluent were diluted with Milli-Q water (R = 18.2 Ω) to achieve 1x working concentration (based on user's manual). The Superblock PBS buffer (ThermoFisher, 37518), the streptavidin poly-HRP stock solution (ThermoFisher, 21140) and the poly-HRP dilution buffer (1% casein in 1x PBS, ThermoFisher, N500) were purchased from Thermo Fisher. The working solution of the streptavidin regular-HRP was prepared by diluting the stock solution 200 times with the reagent diluent working solution (1% BSA in 1x PBS). The working solution for the streptavidin poly-HRP was prepared by diluting the stock solution 1,250 times with the poly-HRP dilution buffer. The chemiluminescent substrate (SuperSignal ELISA Femto Substrate, ThermoFisher, 37075) was used for detection. The working substrate solution was prepared by equal-volumetric mixing of the Luminol + Enhancer Solution and the Stable Peroxide Solution (all contained in the substrate kit) at room temperature.

6.6.7. PCA analysis procedure

To reduce dimensionality for classification we applied PCA analysis on the EGFR, HER2, ADAM15, and Survivin concentration results. A natural log operation was first applied to all ELISA measurements. Then the measurements results were splinted into a training set (49 samples, including urine measurements from the low number group and a few additional baseline readings) and a testing set (34 samples). PCA was first applied to the 49-by-4 dataset to produce 49-by-4 principal component scores. Based on the eigenvalue, approximately 93% variability was explained with the first two PCs. Hence, we used the primary two principal components for further analysis. With the 4-by-4 PCA coefficients acquired from the training set, the PC scores of the testing set can be calculated by multiplying the PCA coefficients to the testing samples' dataset.

6.7. References

1 Siegel, R. L., Miller, K. D. & Jemal, A. Cancer statistics, 2018. *CA: A Cancer Journal for Clinicians* **68**, 7-30, doi:10.3322/caac.21442 (2018).

2 Siegel, R. L., Miller, K. D. & Jemal, A. Cancer statistics, 2019. *CA: a cancer journal for clinicians* **69**, 7-34 (2019).

3 Cohen, S. M., Ohnishi, T., Arnold, L. L. & Le, X. C. Arsenic-induced bladder cancer in an animal model. *Toxicology and applied pharmacology* **222**, 258-263 (2007).

4 Tian, B. *et al.* Effects of curcumin on bladder cancer cells and development of urothelial tumors in a rat bladder carcinogenesis model. *Cancer letters* **264**, 299-308 (2008).

5 Richmond, A. & Su, Y. (The Company of Biologists Ltd, 2008).

6 Hiles, G. L. *et al.* A surgical orthotopic approach for studying the invasive progression of human bladder cancer. *Nature protocols* **14**, 738 (2019).

7 Ito, R., Takahashi, T., Katano, I. & Ito, M. Current advances in humanized mouse models. *Cellular & molecular immunology* **9**, 208 (2012).

8 Garrison, J. C. *et al.* In vivo evaluation and small-animal PET/CT of a prostate cancer mouse model using 64Cu bombesin analogs: side-by-side comparison of the CB-TE2A and DOTA chelation systems. *Journal of Nuclear Medicine* **48**, 1327-1337 (2007).

9 Deroose, C. M. *et al.* Multimodality imaging of tumor xenografts and metastases in mice with combined small-animal PET, small-animal CT, and bioluminescence imaging. *Journal of Nuclear Medicine* **48**, 295-303 (2007).

10 Chan, E., Patel, A., Heston, W. & Larchian, W. Mouse orthotopic models for bladder cancer research. *BJU Int.* **104**, 1286-1291 (2009).

11 Jäger, W. *et al.* Ultrasound-guided intramural inoculation of orthotopic bladder cancer xenografts: a novel high-precision approach. *PloS one* **8**, e59536 (2013).

12 Kuroda, S. *et al.* Establishment of a non-invasive semi-quantitative bioluminescent imaging method for monitoring of an orthotopic esophageal cancer mouse model. *PloS one* **9**, e114562 (2014).

13 Keyaerts, M., Caveliers, V. & Lahoutte, T. Bioluminescence imaging: looking beyond the light. *Trends in molecular medicine* **18**, 164-172 (2012).

14 Sun, A. *et al.* Firefly Luciferase–Based Dynamic Bioluminescence Imaging: A Noninvasive Technique to Assess Tumor Angiogenesis. *Neurosurgery* **66**, 751-757 (2010).

15 Van Rhijn, B. W., van Der Poel, H. G. & van Der Kwast, T. H. Urine markers for bladder cancer surveillance: a systematic review. *European urology* **47**, 736-748 (2005).

16 Vrooman, O. P. & Witjes, J. A. Urinary markers in bladder cancer. *European urology* **53**, 909-916 (2008).

17 Hanke, M. *et al.* in *Urologic oncology: seminars and original investigations.* 655-661 (Elsevier).

18 Smith, S. D. *et al.* Urine detection of survivin and diagnosis of bladder cancer. *Jama* **285**, 324-328 (2001).

19 Tan, X. *et al.* Glass capillary based microfluidic ELISA for rapid diagnostics. *Analyst* **142**, 2378-2385 (2017).

20 Jolliffe, I. *Principal component analysis*. (Springer, 2011).

21 Tamura, S. *et al.* Molecular correlates of in vitro responses to dacomitinib and afatinib in bladder cancer. *Bladder Cancer* **4**, 77-90 (2018).
22 Nicholson, R., Gee, J. & Harper, M. EGFR and cancer prognosis. *European journal of cancer* **37**, 9-15 (2001).
23 Chow, N.-H. *et al.* Significance of urinary epidermal growth factor and its receptor expression in human bladder cancer. *Anticancer research* **17**, 1293-1296 (1997).
24 Lae, M. *et al.* Assessing HER2 gene amplification as a potential target for therapy in invasive urothelial bladder cancer with a standardized methodology: results in 1005 patients. *Annals of Oncology* **21**, 815-819 (2009).
25 Krüger, S. *et al.* HER2 overexpression in muscle-invasive urothelial carcinoma of the bladder: Prognostic implications. *International journal of cancer* **102**, 514-518 (2002).
26 Lucas, N., Najy, A. J. & Day, M. L. The therapeutic potential of ADAM15. *Current pharmaceutical design* **15**, 2311-2318 (2009).
27 Hiles, G. L. *et al.* ADAM15 is functionally associated with the metastatic progression of human bladder cancer. *PloS one* **11**, e0150138 (2016).
28 Shariat, S. F. *et al.* Urine detection of survivin is a sensitive marker for the noninvasive diagnosis of bladder cancer. *The Journal of urology* **171**, 626-630 (2004).
29 Tan, X. *et al.* Rapid Mouse Follicle Stimulating Hormone Quantification and Estrus Cycle Analysis Using an Automated Microfluidic Chemiluminescent ELISA System. *ACS Sens.* **3**, 2327-2334 (2018).
30 Hovelson, D. H. *et al.* Targeted DNA and RNA sequencing of paired urothelial and squamous bladder cancers reveals discordant genomic and transcriptomic events and unique therapeutic implications. *European urology* **74**, 741-753 (2018).
31 Ojeda, I., Moreno-Guzmán, M., González-Cortés, A., Yáñez-Sedeño, P. & Pingarrón, J. Electrochemical magnetoimmunosensor for the ultrasensitive determination of interleukin-6 in saliva and urine using poly-HRP streptavidin conjugates as labels for signal amplification. *Analytical and bioanalytical chemistry* **406**, 6363-6371 (2014).
32 Wen, Y. *et al.* DNA nanostructure-based ultrasensitive electrochemical microRNA biosensor. *Methods* **64**, 276-282 (2013).
33 Attrée, O., Guglielmo-Viret, V., Gros, V. & Thullier, P. Development and comparison of two immunoassay formats for rapid detection of botulinum neurotoxin type A. *Journal of immunological methods* **325**, 78-87 (2007).
34 Systems, R. *Human EGFR DuoSet ELISA*, <https://www.rndsystems.com/products/human-egfr-duoset-elisa_dy231> (
35 Systems, R. *Human ErbB2/Her2 DuoSet ELISA*, <https://www.rndsystems.com/products/human-erbb2-her2-duoset-elisa_dy1129b> (
36 Systems, R. *Human ADAM15 DuoSet ELISA*, <https://www.rndsystems.com/products/human-adam15-duoset-elisa_dy935> (
37 Systems, R. *Human Total Survivin DuoSet IC ELISA*, <https://www.rndsystems.com/products/human-total-survivin-duoset-ic-elisa_dyc647-2> (
38 Shirley, M. Dacomitinib: first global approval. *Drugs* **78**, 1947-1953 (2018).
39 Grivas, P. D. *et al.* Evaluation of the antitumor activity of dacomitinib in models of human bladder cancer. *Molecular medicine* **19**, 367-376 (2013).
40 Kawanishi, H. *et al.* Secreted CXCL1 is a potential mediator and marker of the tumor invasion of bladder cancer. *Clin. Cancer Res.* **14**, 2579-2587 (2008).

41 Cappellen, D. *et al.* Frequent activating mutations of FGFR3 in human bladder and cervix carcinomas. *Nat. Genet.* **23**, 18 (1999).
42 Bryan, R. T. *et al.* Protein shedding in urothelial bladder cancer: prognostic implications of soluble urinary EGFR and EpCAM. *Br. J. Cancer* **112**, 1052 (2015).
43 Bryan, R. *et al.* Urinary EpCAM in urothelial bladder cancer patients: characterisation and evaluation of biomarker potential. *Br. J. Cancer* **110**, 679 (2014).
44 Pan, C.-x. *et al.* Development and characterization of bladder cancer patient-derived xenografts for molecularly guided targeted therapy. *PloS one* **10**, e0134346 (2015).
45 Lin, T.-Y. *et al.* Novel theranostic nanoporphyrins for photodynamic diagnosis and trimodal therapy for bladder cancer. *Biomaterials* **104**, 339-351 (2016).
46 Morrissey, J. J., London, A. N., Luo, J. & Kharasch, E. D. in *Mayo Clinic Proceedings.* 413-421 (Elsevier).
47 Han, W. K. *et al.* Human kidney injury molecule-1 is a tissue and urinary tumor marker of renal cell carcinoma. *Journal of the American Society of Nephrology* **16**, 1126-1134 (2005).
48 Groskopf, J. *et al.* APTIMA PCA3 molecular urine test: development of a method to aid in the diagnosis of prostate cancer. *Clinical chemistry* **52**, 1089-1095 (2006).
49 Mitchell, P. J. *et al.* Can urinary exosomes act as treatment response markers in prostate cancer? *Journal of translational medicine* **7**, 4 (2009).
50 Gontero, P., Banisadr, S., Frea, B. & Brausi, M. Metastasis markers in bladder cancer: a review of the literature and clinical considerations. *European urology* **46**, 296-311 (2004).
51 Knowles, M. A. & Hurst, C. D. Molecular biology of bladder cancer: new insights into pathogenesis and clinical diversity. *Nature Reviews Cancer* **15**, 25 (2015).
52 Szarvas, T. *et al.* Matrix metalloproteinase-7 as a marker of metastasis and predictor of poor survival in bladder cancer. *Cancer science* **101**, 1300-1308 (2010).
53 Scheffer, A.-R. *et al.* Circulating microRNAs in serum: novel biomarkers for patients with bladder cancer? *World journal of urology* **32**, 353-358 (2014).
54 Wood, S. L., Knowles, M. A., Thompson, D., Selby, P. J. & Banks, R. E. Proteomic studies of urinary biomarkers for prostate, bladder and kidney cancers. *Nat. Rev. Urol.* **10**, 206 (2013).
55 Eissa, S., Habib, H., Ali, E. & Kotb, Y. Evaluation of urinary miRNA-96 as a potential biomarker for bladder cancer diagnosis. *Med. Oncol.* **32**, 413 (2015).
56 Piao, X. M. *et al.* Urinary cell-free microRNA biomarker could discriminate bladder cancer from benign hematuria. *Int. J. Cancer* **144**, 380-388 (2019).
57 Najy, A. J., Day, K. C. & Day, M. L. The ectodomain shedding of E-cadherin by ADAM15 supports ErbB receptor activation. *Journal of Biological Chemistry* **283**, 18393-18401 (2008).

Chapter 7

The Quantification and Membrane Marker Analysis of Exosomes

7.1. Introductory remarks

In this chapter, we will introduce another application of our optofluidic ELISA platform: exosome quantification and membrane protein analysis. The quantification of exosomes was based on the detection of exosome membrane marker CD9. In addition, we developed a multiplexed immunoprofiling technology which can be used to quantitatively evaluate the expression of functional membrane proteins on human epithelial cell-derived exosomes, with unpurified cell culturing mediums.

7.2. Motivations

Exosomes are membrane-encapsulated nanometer-sized vesicles carrying multiple types of molecular "cargos" that can reflect the status of the cell that secreted them[1-2]. Recently, cancer biologists discovered that tumor cell-derived exosomes may participate in diseases progression-related processes, such as cellular growth[3], intercellular communication[4], immune responses[5], and metastasis[1, 6-7]. This indicates that the exosomes may be able to serve as a type of comprehensive marker for indicating the molecular nature of cancers[1, 8-9]. For cancers that developed from epithelial cells (e.g., bladder cancer and certain types of breast cancers), membrane proteins such as EGFR and HER2 are known to have a significant impact on tumor progression[10-11]. Thus, to

better understand the diagnostic significances and biological functions of epithelial cancer cell-derived exosomes, conducting membrane protein-related researches with well-demonstrated epithelial cancer cell lines (particularly human cancer cell lines) are necessary.

However, due to the low production rate, exosome concentration (in cell culturing medium) for a common human cell line under standard cell culture conditions is typically on the scale of 10 ug/mL even after a few days of culture. For this reason, the quantification and molecular analysis of exosomes in dilute samples, such as the cell culturing medium, have always been a challenging job.

Despite the rapidly growing attractions on exosome's biological functions and clinical significances, researchers are still suffering from lacking "gold-standard" technology for the quantification and functional analysis of exosomes. Approaches that based on physical properties of exosomes (e.g., dynamic light scattering) can non-specifically quantify nanoparticles in liquid samples, but they are still unable to retrieve any molecular information from exosomes[12].

On the other hand, traditional biomolecular analysis technologies such as Western blot, are widely used for analyzing the protein contents of the exosome[13-14]. However, due to the limitations in required input protein quantity (>5 ug/lane), Western blot cannot be used to analyze dilute samples such as cell culturing mediums directly[15]; Exosome isolation/purification with complicated procedures must be performed beforehand[16-18]. Moreover, the lysing of exosomal membranes (required before protein electrophoresis) will make this assay impossible for differentiating membrane proteins and plasmic proteins.

Recently, ELISA-style immunoassays have also been used for exosome quantification. As a test that specifically detects the membrane proteins (typically based on CD9, CD63, or CD81)

on native exosomes, ELISA-style assays have better applicability for quantifying exosomes in liquid samples (e.g., serum, cell culturing mediums). However, conventional plate-based exosome ELISA has several well-known problems such as limited sensitivity, large sample consumptions, and long assay durations. In addition, the calibration standards provided by the ELISA kits are generalized for all cell lines. This may be good enough for quantifying soluble protein, but for exosomes that have cell type-dependent expression profiles, having only a generalized calibration curve is highly likely insufficient.

Based on a previously-described microfluidic chemiluminescent ELISA platform[19-20], we now established a multifunctional exosome analysis technology, using the general exosomal marker CD9 as the principle detection target. Our results indicate that we were able to perform rapid exosome quantification (<1 hour) with relatively small sample volume (~8 μL), high sensitivity (optimal LOD = 8.7×10^7 exosome/mL), and high species specificity. To enhance the measurement accuracies, we established individualized calibration curves for multiple cell lines and evaluated the expression levels of CD9 across all of them. With this exosome ELISA system and the individualized calibration curves, we performed exosome secretion assay with four representative human bladder cancer cell lines at multiple time spots.

In addition to the quantification of exosomes, we also proved that we could quantitatively evaluate the expression level for a penal of four cancer-related exosomal membrane proteins (EGFR[11], HER2[10], MHC-I, and EpCAM[21-22]), using an immunoprofiling assay that combines immunoprecipitation and sandwich ELISA. The exosome sample does not need to be pre-isolated and the assay requires a tiny amount of total input protein (<40 ng/marker). The practicability of this immunoprofiling technology was evaluated with the exosomes that were secreted by multiple cell lines.

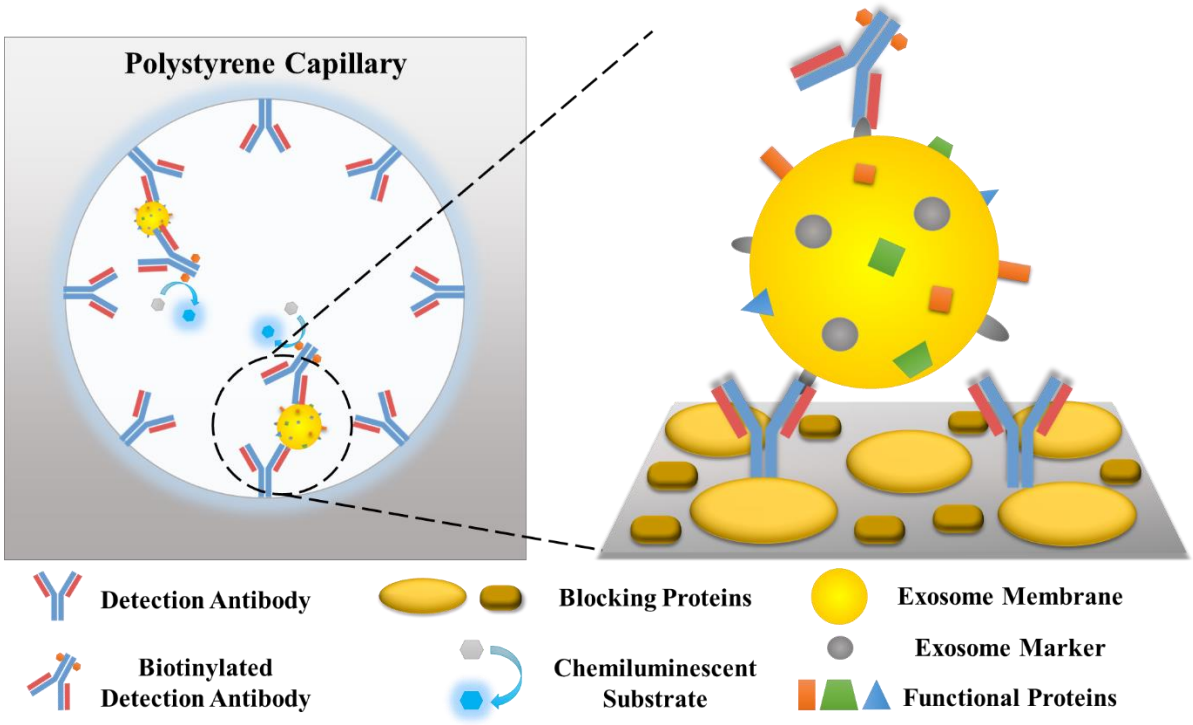

Figure 7.1. Immunoassay protocol. For exosome quantification, the capture and detection antibodies can be the same type of antibody

7.3. Results

7.3.1. Exosome quantification based on CD9 expression

As previous researches indicate, the transmembrane proteins CD9, CD63 and CD81 are generally considered as the membrane markers for exosomes. For this reason, we decided to use these membrane markers (CD9 in our case) as the detection targets of our exosome ELISA. The principle of this assay is schematically illustrated in Fig. 7.1. To ensure the detection specificity, we decided to use sandwich ELISA for exosome quantification.

A sandwich ELISA kit for protein detection typically employs a pair of antibodies that recognize different epitopes on a protein molecule. But for exosomes, the extracellular domain of

the membrane markers has very limited room for antibody binding (simultaneous binding of two antibody molecules is unpractical). In contrast, as a complex particle, an exosome naturally contains several identical membrane marker molecules that can serve as the recognition epitopes. This means that using a single type of antibody for both capture and detection is more appropriate than finding an antibody pair.

In this study, we chose human CD9 as the target molecule for exosome quantification in the concept demonstration experiments. The antibody we chose (clone: MEM-61) was designed to specifically bind with the extracellular domain of the human CD9 molecule[23], thus it should not cross-react with the exosome that secreted by other species. In order to achieve sufficient capture efficiency, excessive amount of capture antibody was immobilized on the reactor's surface (20 μg/mL for antibody coating). Since there is no "standard sample" can be found, we designed a group of experiments to evaluate the quantification performance and species specificity of our exosome ELISA.

Since the CD9 expression in different cell lines varies significantly across different types of human cell lines, we decided to establish an individual calibration curve for each cell line. As illustrated in Fig. 2(A), CD9-based exosome calibrations were performed with 10 selected cell lines. Our test subjects include four human bladder cancer cell line, one immortalized human bladder epithelial cell line, two human breast cancer cell line and one human foreskin fibroblast cell line. A mouse bladder cancer cell line and a mouse fibroblast cell line were used as the negative controls. All cell lines were cultured with exosome-depleted FBS. To ensure a fair comparison, the exosome was first isolated from the culturing medium (with ExoQuick plus isolation kit) after 2-4 days of culturing[16, 24]. Then, we normalized the total protein concentration of the isolated exosome samples to 15 μg/mL.

As presented in Fig. 7.2(B) and (C), the chemiluminescent intensities were measured at 6 different exosome concentrations that were prepared with serial dilutions (15, 5, 1.67, 0.55, 0.18 and 0 μg/mL, respectively). There was no signal observed with the blank control for all measurements so there's no need for background subtraction. The calibration curves for the bladder cancer cell lines were close to each other. However, the calibration curves for the remaining four human cell lines differ significantly from each other, showing that our strategy for generating individualized calibration curves is necessary. The lower limit of detection (LLOD) for most of the human cell lines are below or equals to 0.18 μg/mL (1.4 ng/capillary). However, due to low CD9 expression, the LLOD for human foreskin fibroblast was 1.66 μg/mL. No signal was observed with mouse cell line-derived exosomes (marked as 0.1 on Fig. 3(B)), indicating our exosome ELISA has an excellent species specificity.

We also explored the LLOD for exosomes that have the highest CD9 expression, which were derived from UM-UC-9 cell line, the data can be found in Fig. 2(C). The LLOD was 9.8 ng/mL (0.08 ng/capillary) for the exosomes derived from UM-UC-9 cells. Based on dynamic light scattering (DLS) measurements, this concentration equals to 8.7×10^7 particles/ml (7×10^5). The means the detection limit of our exosome ELISA is 300 times more sensitive than conventional plate-based ELISA (also targeting CD9 on exosome membrane). Benefitted from the employment of high surface-to-volume ratio microfluidic reactors, we were able to complete the entire assay within one hour, which was significantly shorter than conventional plate-based ELISA (at least 5 hours).

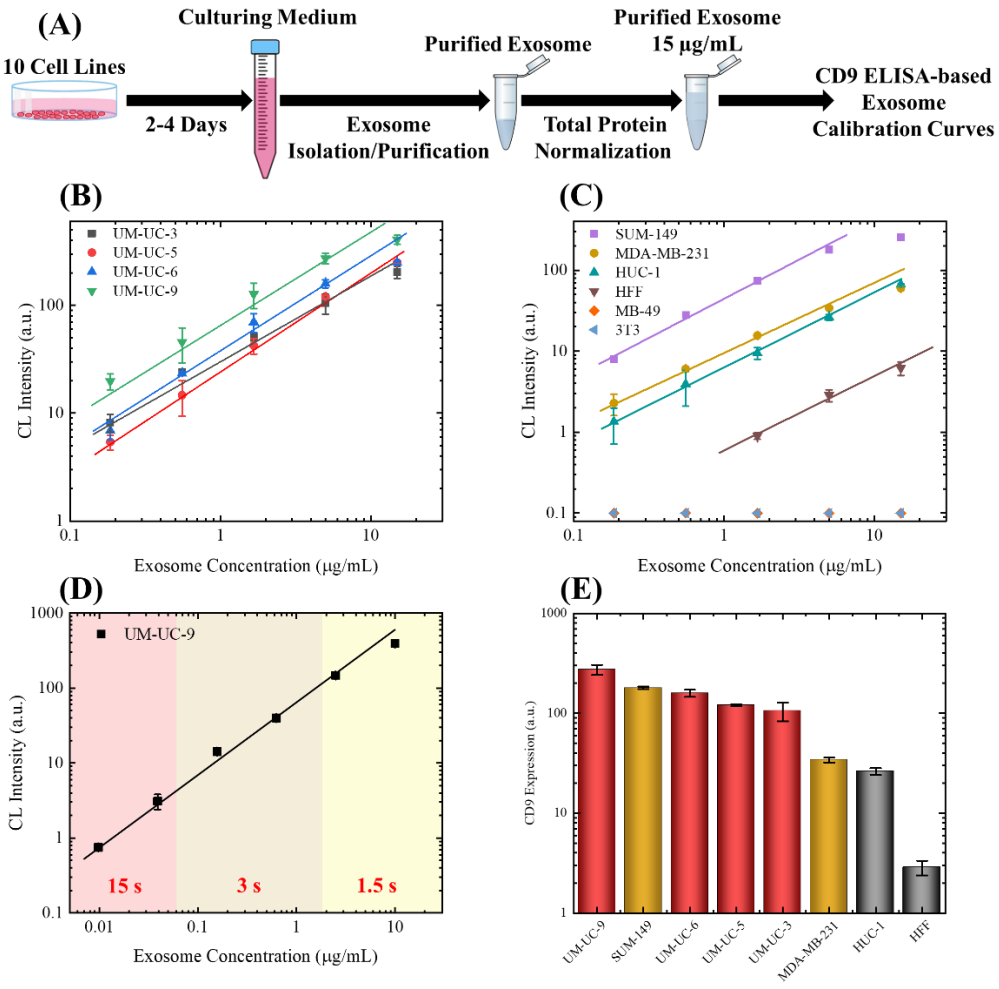

Figure 7.2. Exosome calibrations. (A). The illustration of the process for generating exosome calibration curves. (B). Exosome calibration curves with bladder cancer cell-derived exosomes. (C). Exosome calibration curves with breast cancer cell (SUM-149, MDA-MB-231), bladder epithelial cell (HUC-1), human foreskin fibroblast (HFF), mouse bladder cancer (MB-49) and mouse fibroblast (3T3)-derived exosomes. (D). The entire dynamic range of UM-UC-9 derived exosomes. The calibration curve was assembled with measurements that were obtained from multiple exposure times. (E). CD9 expressions for human cell line-derived exosomes.

To better visualize the differences in exosomal CD9 expressions across the 8 human cell lines, we extracted the chemiluminescent intensities at 5 µg/mL (40 ng/mL per capillary) of input protein concentration (plotted in descending order in Fig. 7.2(D)). At this concentration, the calibration curves for all cell lines are still in their linear ranges and all chemiluminescent

intensities are easily measurable (not too high or too low). The data from the bladder cancer cell lines were labeled with red, the data from breast cancer cell lines were labeled with yellow and the data from non-cancer cell lines were labeled with grey. As it indicated in the figure, the exosomal expression levels of CD9 for the first 7 cell lines is within one order of magnitude. All of them are significantly higher than the CD9 expression in human foreskin fibroblast-derived exosomes (by 1-2 orders of magnitude). For ensuring a similar exosome capture affinity, the human foreskin fibroblast will be excluded in the following experiments.

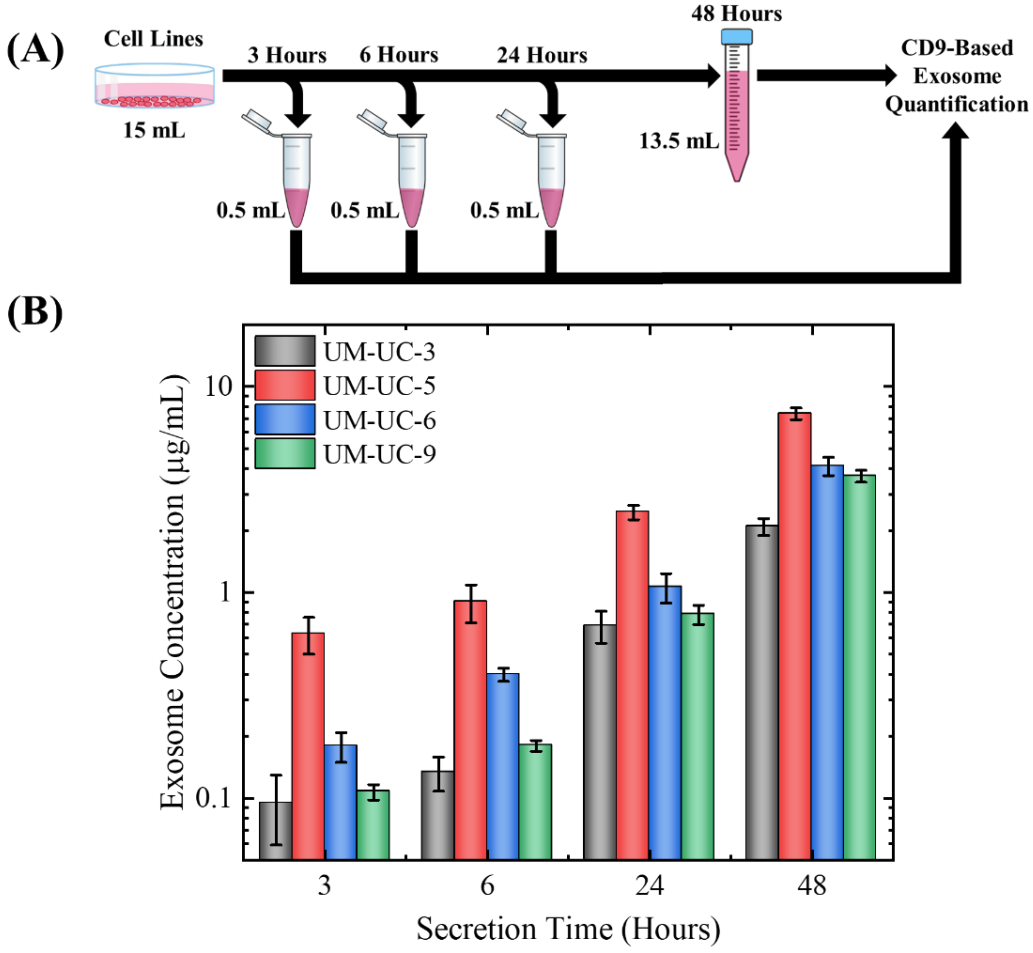

Figure 7.3. Exosome secretion assay with four bladder cancer cell lines. (A). Illustration of the experiment procedure. (B). Exosome concentration in the culturing medium at four different time points. The error bars were generated from triplicated measurements.

7.3.2. Exosome secretion surveillance

To examine the quantification sensitivity in real-world applications, we conducted an exosome-secretion assay with the four bladder cancer cell lines. Fig.7.3(A) is a brief illustration of the experimental design. For each cell line, two million cells were first plated on a 15-cm cell culturing plate (with 15 mL of exosome-free culturing medium). Then, 0.5 mL of sample was collected at 3 hours, 6 hours and 24 hours. All culturing medium were collected at the 48^{th} hour. The exosome concentrations in the culturing medium at all four time points were then quantified with our CD9-based exosome ELISA and the individualized calibration curves.

As the results presented in Fig.7.3(B), we were able to detect and quantify exosomes even at the earliest sampling time point (3 hr). The exosome concentrations for all four cell lines show obvious increasing trends during the 48-hours surveillance period. From the data at 3 hr and 6 hr (before the start of cell proliferation), UM-UC-5 has the highest exosome secretion rate and UM-UC-3 has the lowest secretion rate.

7.3.3. The immunoprofiling of exosomes

Based on the exosome ELISA described in the previous sections, we developed a quantitative immunoprofiling technology for examining the expressions of functional proteins on exosome membranes. The procedure and the concept of this assay was described in Fig. 7.4 (A) and (B). The concept of this immunoprofiling assay is similar to co-immunoprecipitation, CD9-targeting capture antibody was first used for pulling down exosomes from liquid samples. Antibodies of functional membrane proteins were then subsequentially applied to the immobilized exosome (serving as detection antibodies). The expression of the functional membrane proteins can then be analyzed by measuring the chemiluminescent intensity. Note that each membrane marker needed to be measured in separate microfluidic ELISA reactor.

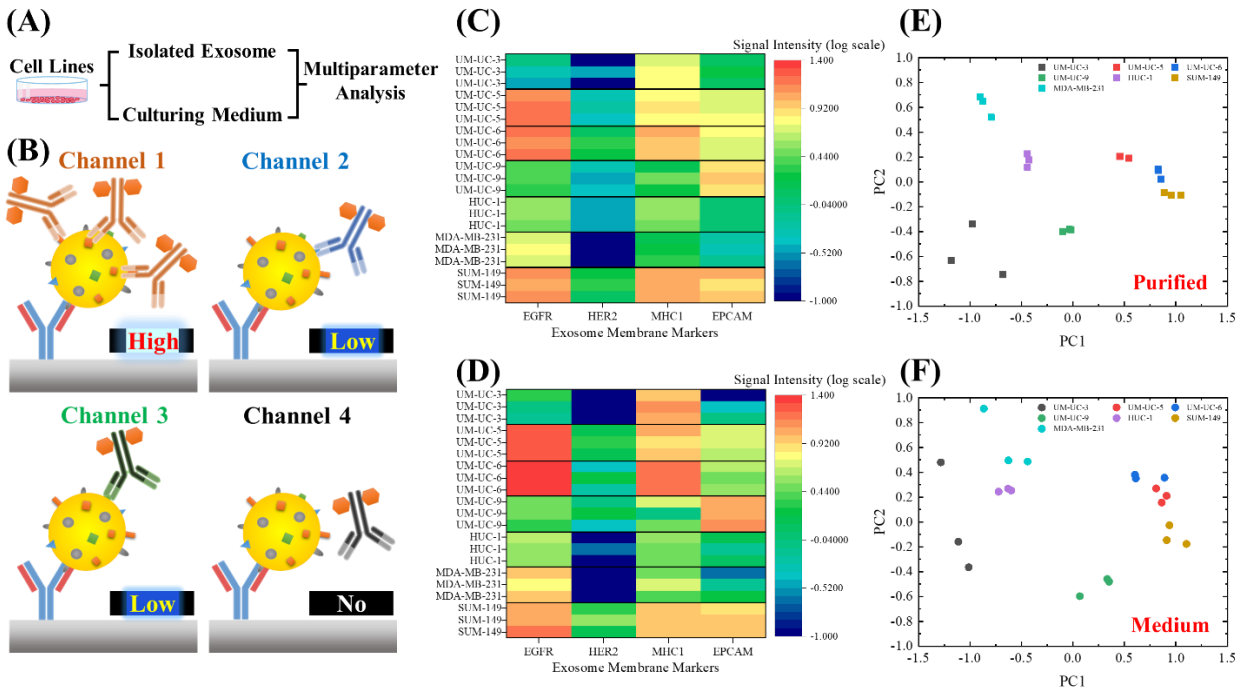

Figure 7.4. Multiparameter analysis of four exosome membrane proteins. (A). A brief procedure for the side-by-side study. (B). Concept illustration for of the multiparameter analysis. A common CD9 capture antibody was used for exosome immobilization. Different detection antibodies were used for analyzing protein expressions. (C). Heatmap for the exosomal expression of the four selected proteins (EGFR, HER2, MHC1 and EpCAM) with purified exosome samples. (D). Heatmap for the exosomal expression of the four selected proteins with cell culturing medium. (E). PCA plot for the purified exosome samples. (F). PCA plot for the culturing medium samples.

In this demonstration of concept study, we chose four proteins that were believed to have high diagnostic and therapeutic value for epithelial cancers (including bladder cancer and breast cancer). They are EGFR, HER2, MHC1 and EpCAM. We also designed a side-by-side study to validate the reliability of our technology (see Fig. 7.4(A) for procedure illustration). One group of experiments were performed with the purified exosome samples (normalized to 5 μg/mL with Bradford assay), the other group of experiments were performed with cell culturing medium (after 30 mins of 10000 g centrifugation for removing cell debris). The concentration of the exosome samples in both groups were first quantified via CD9 exosome ELISA. Then, the

chemiluminescent intensities for the functional markers were recorded at a fixed exposure time (6 s). The background level for each individual marker are also recorded and subtracted from the measurement results. All measurement results that were lower than the background was marked as 0. For both groups, the signal intensities from all functional proteins were subsequentially normalized to 1 μg/mL of total exosome protein (based on CD9 exosome ELISA results).

As the heatmaps (Fig. 7.4(C)-(D)) present, the expression level of the functional proteins varies significantly across the seven cell lines. As an example, UM-UC-5 and UM-UC-6 have high EGFR expression, but UM-UC-3 has very low level of EGFR. Some of the cell lines do not even express certain markers (e.g., HER2 was not observed on MDA-MB-23-derived exosomes). Interestingly, the expression level of exosomal membrane proteins do not strictly correlates with the expression pattern of the cells. For example, the cell lysate of UM-UC-6 have a moderate expression level of EGFR but UM-UM-6-derived exosomes have very high EGFR expression. For both the purified group and the culturing medium group, high similarities were observed from the triplicated results within each group. This indicate the expression patterns of exosomal proteins may be able to serve as "molecular fingerprints" for differentiating or phenotyping different cell lines.

To better visualize the similarities and differences between the exosomes derived from the 7 cell lines, we performed a PCA analysis for both groups. As Fig. 4(E)-(F) present, the data points from the same cell line generally clustered together and the 7 cell lines can easily differentiate from each other. The results from the two groups have high similarity in the distribution of the data points. But apparently the results generated with purified exosomes have slightly better consistency as the pointed clustered closer in the PCA plot. The results also indicate that use

unpurified culturing medium directly as the input sample for exosome membrane protein immunoprofiling.

7.4. Discussion and conclusion:

In this project, we have successfully developed an exosome quantification technology based on CD9 chemiluminescent ELISA. Benefitted from the employment of microfluidic ELISA reactors, we were able to complete the entire assay within one hour, with 8 μL of input sample. With adjustable exposure times, we were able to generate calibration curves with the exosomes that were purified from multiple human cell lines. For the cell lines with appropriate CD9 expressions, the LLOD can be as low as 8.7×10^7 particles/ml (7×10^5), which is a few hundred times more sensitive than conventional plate-based exosome ELISAs.

Based on this exosome ELISA technology, we also successfully developed an immunoprofiling technology to quantitatively evaluate the expression of several exosomal membrane proteins. The assay requires a very small amount of total input protein (<5 μg/mL, 40 ng/capillary), which is at least 125 times less than the required protein quantity for Western blot (>5 μg/lane).

Our results indicate that the exosomal expression level of the protein markers are correlated to but not solely dependent on the cellular protein expression level. We also discovered that each cell line has a unique "molecular fingerprint" that can be retrieved from the expression profiles of the exosomal membrane proteins. The technology demonstrated in this paper provides a cost-effective, sensitive, convenient and useful tool for exosome-related cellular biology researches. It also has the potential to be used in the fields of cancer diagnosis and personalized medicine.

However, this technology still has several limitations, including the relatively low throughput and non-negligible background when performing immunoprofiling. These problems can be potentially resolved by designing a new microfluidic immunoassay reactor that has multiplexing capability and employing antibodies that have better specificity.

7.5. References

1. Kumar, D.; Gupta, D.; Shankar, S.; Srivastava, R. K., Biomolecular characterization of exosomes released from cancer stem cells: possible implications for biomarker and treatment of cancer. *Oncotarget* **2015,** *6* (5), 3280.
2. Mathivanan, S.; Ji, H.; Simpson, R. J., Exosomes: extracellular organelles important in intercellular communication. *J. Proteomics* **2010,** *73* (10), 1907-1920.
3. Théry, C.; Zitvogel, L.; Amigorena, S., Exosomes: composition, biogenesis and function. *Nat. Rev. Immunol.* **2002,** *2* (8), 569-579.
4. Simons, M.; Raposo, G., Exosomes–vesicular carriers for intercellular communication. *Curr. Opin. Cell. Biol.* **2009,** *21* (4), 575-581.
5. Greening, D. W.; Gopal, S. K.; Xu, R.; Simpson, R. J.; Chen, W. In *Exosomes and their roles in immune regulation and cancer*, Seminars in cell & developmental biology, Elsevier: 2015; pp 72-81.
6. Mizutani, K.; Terazawa, R.; Kameyama, K.; Kato, T.; Horie, K.; Tsuchiya, T.; Seike, K.; Ehara, H.; Fujita, Y.; Kawakami, K., Isolation of prostate cancer-related exosomes. *Anticancer Res.* **2014,** *34* (7), 3419-3423.
7. Mukherjee, D.; Gao, M.; O'Connor, J. P.; Raijmakers, R.; Pruijn, G.; Lutz, C. S.; Wilusz, J., The mammalian exosome mediates the efficient degradation of mRNAs that contain AU-rich elements. *EMBO J.* **2002,** *21* (1-2), 165-174.
8. Koga, K.; Matsumoto, K.; Akiyoshi, T.; Kubo, M.; Yamanaka, N.; Tasaki, A.; Nakashima, H.; Nakamura, M.; Kuroki, S.; Tanaka, M., Purification, characterization and biological significance of tumor-derived exosomes. *Anticancer Res.* **2005,** *25* (6A), 3703-3707.
9. Lin, J.; Li, J.; Huang, B.; Liu, J.; Chen, X.; Chen, X.-M.; Xu, Y.-M.; Huang, L.-F.; Wang, X.-Z., Exosomes: novel biomarkers for clinical diagnosis. *Sci. World J.* **2015,** *2015*.
10. Ciravolo, V.; Huber, V.; Ghedini, G. C.; Venturelli, E.; Bianchi, F.; Campiglio, M.; Morelli, D.; Villa, A.; Mina, P. D.; Menard, S., Potential role of HER2-overexpressing exosomes in countering trastuzumab-based therapy. *J. Cell. Physiol.* **2012,** *227* (2), 658-667.
11. Yamashita, T.; Kamada, H.; Kanasaki, S.; Maeda, Y.; Nagano, K.; Abe, Y.; Inoue, M.; Yoshioka, Y.; Tsutsumi, Y.; Katayama, S., Epidermal growth factor receptor localized to exosome membranes as a possible biomarker for lung cancer diagnosis. *Pharmazie* **2013,** *68* (12), 969-973.
12. Sokolova, V.; Ludwig, A.-K.; Hornung, S.; Rotan, O.; Horn, P. A.; Epple, M.; Giebel, B., Characterisation of exosomes derived from human cells by nanoparticle tracking analysis and scanning electron microscopy. *Colloids Surf. B Biointerfaces* **2011,** *87* (1), 146-150.
13. Henderson, M. C.; Azorsa, D. O., The genomic and proteomic content of cancer cell-derived exosomes. *Front. Oncol.* **2012,** *2*, 38.
14. Welton, J. L.; Khanna, S.; Giles, P. J.; Brennan, P.; Brewis, I. A.; Staffurth, J.; Mason, M. D.; Clayton, A., Proteomics analysis of bladder cancer exosomes. *Mol. Cell. Proteomics* **2010,** *9* (6), 1324-1338.
15. Ekström, E. J.; Bergenfelz, C.; von Bülow, V.; Serifler, F.; Carlemalm, E.; Jönsson, G.; Andersson, T.; Leandersson, K., WNT5A induces release of exosomes containing pro-angiogenic and immunosuppressive factors from malignant melanoma cells. *Mol. Cancer* **2014,** *13* (1), 88.

16. Caradec, J.; Kharmate, G.; Hosseini-Beheshti, E.; Adomat, H.; Gleave, M.; Guns, E., Reproducibility and efficiency of serum-derived exosome extraction methods. *Clin. Biochem.* **2014,** *47* (13-14), 1286-1292.
17. Hong, C. S.; Muller, L.; Boyiadzis, M.; Whiteside, T. L., Isolation and characterization of CD34+ blast-derived exosomes in acute myeloid leukemia. *PloS one* **2014,** *9* (8).
18. Street, J. M.; Barran, P. E.; Mackay, C. L.; Weidt, S.; Balmforth, C.; Walsh, T. S.; Chalmers, R. T.; Webb, D. J.; Dear, J. W., Identification and proteomic profiling of exosomes in human cerebrospinal fluid. *J. Transl. Med.* **2012,** *10* (1), 5.
19. Tan, X.; Broses, L. J.; Zhou, M.; Day, K. C.; Liu, W.; Li, Z.; Weizer, A.; Munson, K. A.; Oo, M. K. K.; Day, M., Multiparameter Urine Analysis for Quantitative Bladder Cancer Surveillance of Orthotopic Xenografted Mice. *Lab Chip* **2020**.
20. Tan, X.; David, A.; Day, J.; Tang, H.; Dixon, E. R.; Zhu, H.; Chen, Y.-C.; Khaing Oo, M. K.; Shikanov, A.; Fan, X., Rapid mouse follicle stimulating hormone quantification and estrus cycle analysis using an automated microfluidic chemiluminescent ELISA system. *ACS sens.* **2018,** *3* (11), 2327-2334.
21. Marhaba, R.; Klingbeil, P.; Nuebel, T.; Nazarenko, I.; Buechler, M. W.; Zoeller, M., CD44 and EpCAM: cancer-initiating cell markers. *Curr. Mol. Med.* **2008,** *8* (8), 784-804.
22. Runz, S.; Keller, S.; Rupp, C.; Stoeck, A.; Issa, Y.; Koensgen, D.; Mustea, A.; Sehouli, J.; Kristiansen, G.; Altevogt, P., Malignant ascites-derived exosomes of ovarian carcinoma patients contain CD24 and EpCAM. *Gynecol. Oncol.* **2007,** *107* (3), 563-571.
23. Ng, Y. H.; Rome, S.; Jalabert, A.; Forterre, A.; Singh, H.; Hincks, C. L.; Salamonsen, L. A., Endometrial exosomes/microvesicles in the uterine microenvironment: a new paradigm for embryo-endometrial cross talk at implantation. *PloS one* **2013,** *8* (3).
24. Tauro, B. J.; Greening, D. W.; Mathias, R. A.; Ji, H.; Mathivanan, S.; Scott, A. M.; Simpson, R. J., Comparison of ultracentrifugation, density gradient separation, and immunoaffinity capture methods for isolating human colon cancer cell line LIM1863-derived exosomes. *Methods* **2012,** *56* (2), 293-304.

Chapter 8

Summary and Outlook

In this dissertation, we introduced the successful development of a multifunctional and automated optofluidic biosensing platform based on microfluidic ELISA. Furthermore, we demonstrated that this optofluidic biosensing platform can be applied to the detection, quantification, and functional analysis of a variety of targets, including both common ELISA analytes such as proteins and hormones, and new types of analytes such as exosomes.

In contrast to conventional plate-based ELISA, our optofluidic ELISA platform utilizes mass-producible, high surface-to-volume ratio polystyrene microfluidic channels as the immunoassay reactors, which greatly shortens total assay times. We also developed a low-noise signal amplification protocol (poly-HRP + multiple blockings) and an optical signal quantification system (chemiluminescent imaging + tunable exposure time) optimized for the optofluidic ELISA platform[1-2].

Our optofluidic ELISA platform provides several attractive features such as small sample/reagent consumption (<8 μL), short total assay time (30-45 min), high sensitivity (<1 pg/mL for cytokines such as IL-6), and broad dynamic ranges (3-4 orders of magnitude)[3]. These features allowed us to successfully quantify mouse FSH (follicle stimulating hormone) concentration with a single drop (~20 μL) of tail vein serum[2]. We also successfully monitored bladder cancer progression in orthotopic xenografted mice with only <50 μL of mouse urine[1].

More excitingly, we achieved highly sensitive exosome quantification and multiplexed immuno-profiling with <40 ng/mL of total input protein (per assay). These remarkable measurements could not be achieved with conventional plate-based ELISA but were enabled by our unique optofluidic ELISA.

In addition to the aforementioned advantages over conventional plate-based ELISA, our optofluidic ELISA platform also demonstrates several advantages when compared with cutting-edge, next-generation immunoassay technologies such as digital ELISA (e.g., Simoa) and electro-chemiluminescent ELISA (e.g., MSD)[4-5]. For example, compared to digital ELISA, our optofluidic ELISA has a significantly broader dynamic range, while exhibiting remarkably high sensitivity (comparable with digital ELISA)[5]. Furthermore, our optofluidic ELISA platform also can tolerate much smaller sample/reagent consumption (8 µL vs 100 µL) and operates with much shorter total assay times (15-40 mins vs 90-180 mins) compared to the two aforementioned novel immunoassays[4-6].

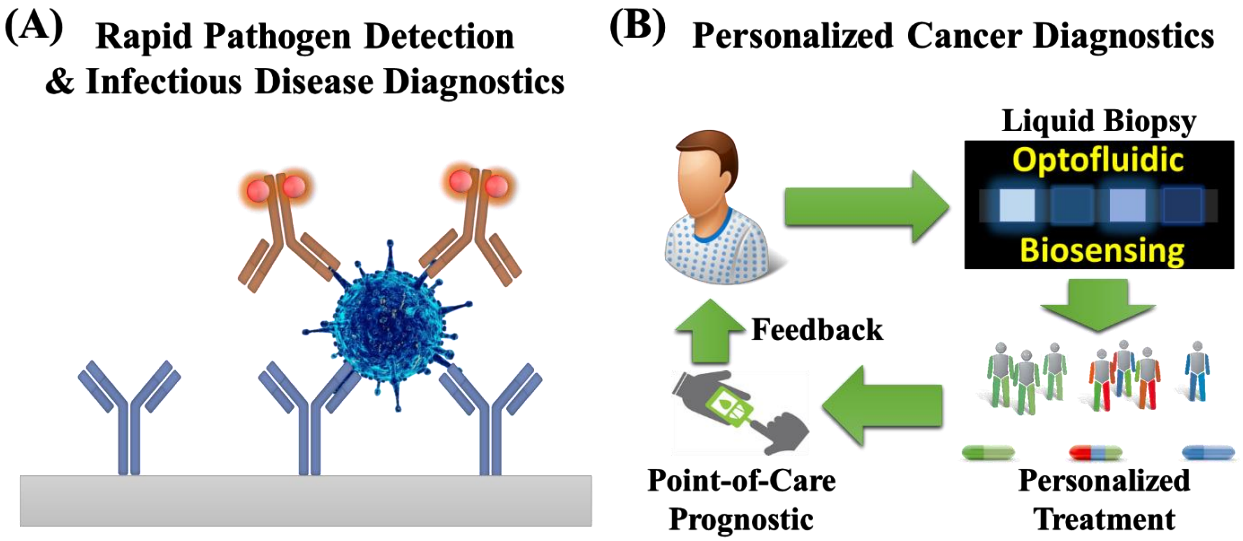

Figure 8.1. Potential clinical applications with optofluidic biosensing platforms. (A) Rapid point-of-care diagnostics for infectious diseases. (B). Personalized cancer diagnosis and prognosis.

As an emerging technology in the biomolecular sensor family, our optofluidic ELISA platform provides a high-performance and cost-effective tool which can be applied across multiple disciplines including endocrinology, oncology, developmental biology, and even forensic science research by targeting different types of markers[7-12]. As depicted in Fig. 8.1 , future work can also adopt this technology platform for clinical applications such as rapid point-of-care diagnostics of infectious diseases[13-14], pathogen phenotyping, personalized diagnostics of auto-immune diseases[15-16], and personalized cancer diagnosis/prognosis[9].

Despite these advantages, several limitations must still be overcome before we can apply our optofluidic ELISA to certain types of applications. First, for fundamental biology research and certain clinical diagnostic applications (e.g., cancer phenotyping and autoimmune disease research, Fig. 8.2 (A)-(B)), a technology with no multiplexing capability presents a tremendous limitation. This is especially true for cellular secretion/expression related research that typically requires simultaneous evaluation of multiple markers (e.g., B-lymphocytes can secrete multiple types of cytokines including IL-6, IL-10, IL-12, IL-15 and TGF-β)[17]. As illustrated in Fig. 8.2 (B), this problem could be potentially resolved by designing a sensor with specially separated sensing areas for different target molecules. Further work can also evaluate the feasibility of integrating the multiplexed biomarker sensor with microscale cell-culturing devices for *in-situ* biosensing. In addition to protein biomarkers, detection/quantification of nucleic acid biomarkers (e.g., miRNA, cfDNA, Fig. 8.2 (D)) should also be explored[10].

Second, for forensic science or criminal investigation applications (e.g., identification of controlled substances, Fig. 8.2 (C)), the bulkiness of our current optofluidic ELISA system is not suitable for field investigations. Our optofluidic ELISA system should be miniaturized into a

portable device to enable facile or on site analysis. Additionally, system miniaturization requires development or modification of sample collecting devices and pre-prepared/pre-packed reagents[18].

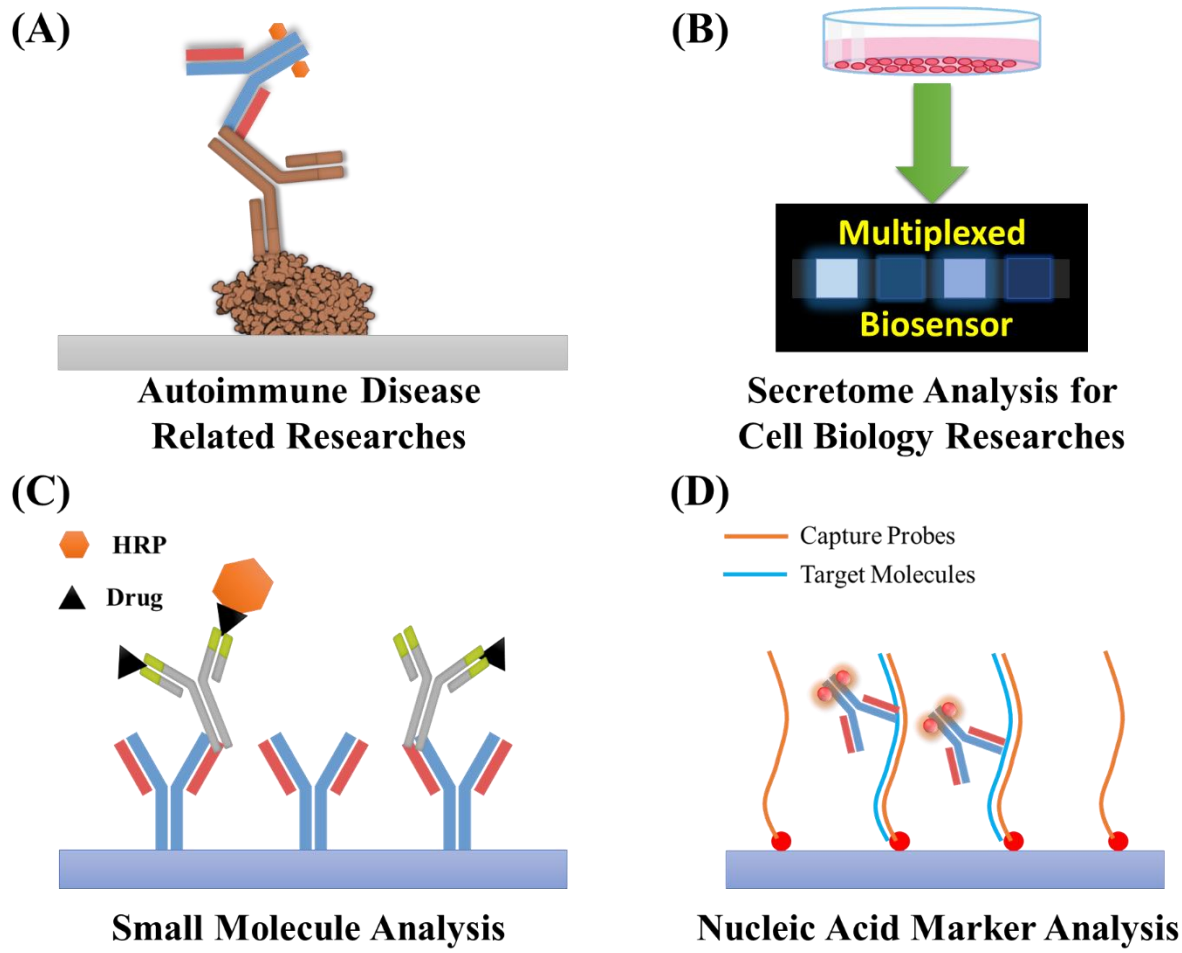

Figure 8.2. Potential research applications with our optofluidic biosensing platform. (A). Autoimmune disease related research. (B). Cellular secretome analysis with a multiplexed sensor. (C). Small molecule drug detection for forensic science research and criminal investigations. (D). Nucleic acid biomarker detection.

Third, for clinical diagnostic/prognostic applications, the throughput of our current optofluidic ELISA system is insufficient. A sensor with only 12 channels may be enough for performing biomolecular analysis in a research laboratory setting, but the number of channels is far too few for analyzing clinical samples, which are typically analyzed in batches. To solve this

problem, a system with higher throughput (higher or at least comparable with a 96-well plate) needs to be designed. Furthermore, an additional microfluidic device for separating serum from whole blood is also desirable.

Finally, we envision that the concepts (especially the reactor design and signal amplification) presented in this dissertation will provide inspiration to the development of other types of biosensors (e.g., lateral flow test-strips, bead-based biosensors, electrochemical biosensors and single-molecule fluorescent biosensors)[19-21]. Given the outstanding performances, attractive features and novel concepts presented in this dissertation, our optofluidic biosensing platform shall have a bright future.

8.1. References

1. Tan, X.; Broses, L. J.; Zhou, M.; Day, K. C.; Liu, W.; Li, Z.; Weizer, A.; Munson, K. A.; Oo, M. K. K.; Day, M., Multiparameter Urine Analysis for Quantitative Bladder Cancer Surveillance of Orthotopic Xenografted Mice. *Lab Chip* **2020**.
2. Tan, X.; David, A.; Day, J.; Tang, H.; Dixon, E. R.; Zhu, H.; Chen, Y.-C.; Khaing Oo, M. K.; Shikanov, A.; Fan, X., Rapid mouse follicle stimulating hormone quantification and estrus cycle analysis using an automated microfluidic chemiluminescent ELISA system. *ACS sens.* **2018,** *3* (11), 2327-2334.
3. Tan, X.; Oo, M. K. K.; Gong, Y.; Li, Y.; Zhu, H.; Fan, X., Glass capillary based microfluidic ELISA for rapid diagnostics. *Analyst* **2017,** *142* (13), 2378-2385.
4. Pavkovic, M.; Riefke, B.; Gutberlet, K.; Raschke, M.; Ellinger-Ziegelbauer, H., Comparison of the MesoScale Discovery and Luminex multiplex platforms for measurement of urinary biomarkers in a cisplatin rat kidney injury model. *J. Pharmacol. Toxicol. Methods* **2014,** *69* (2), 196-204.
5. Rissin, D. M.; Kan, C. W.; Campbell, T. G.; Howes, S. C.; Fournier, D. R.; Song, L.; Piech, T.; Patel, P. P.; Chang, L.; Rivnak, A. J., Single-molecule enzyme-linked immunosorbent assay detects serum proteins at subfemtomolar concentrations. *Nat. Biotechnol.* **2010,** *28* (6), 595.
6. Rissin, D. M.; Walt, D. R., Digital readout of target binding with attomole detection limits via enzyme amplification in femtoliter arrays. *J. Am. Chem. Soc.* **2006,** *128* (19), 6286-6287.
7. Pappa, A.; Seferiadis, K.; Marselos, M.; Tsolas, O.; Messinis, I., Development and application of competitive ELISA assays for rat LH and FSH. *Theriogenology* **1999,** *51* (5), 911-926.
8. Wang, J.; Zhang, S.; Ni, W.; Zhai, X.; Xie, F.; Yuan, H.; Gao, S.; Tai, G., Development and application of a double-antibody sandwich ELISA kit for the detection of serum MUC1 in lung cancer patients. *Cancer Biomark.* **2016,** *17* (4), 369-376.
9. Li, L.; Chen, L.; Zhang, W.; Liao, Y.; Chen, J.; Shi, Y.; Luo, S., Serum cytokine profile in patients with breast cancer. *Cytokine* **2017,** *89*, 173-178.
10. Miyoshi, J.; Toden, S.; Yoshida, K.; Toiyama, Y.; Alberts, S. R.; Kusunoki, M.; Sinicrope, F. A.; Goel, A., MiR-139-5p as a novel serum biomarker for recurrence and metastasis in colorectal cancer. *Sci. Rep.* **2017,** *7* (1), 1-13.
11. Wang, X.; Cohen, L.; Wang, J.; Walt, D. R., Competitive immunoassays for the detection of small molecules using single molecule arrays. *J. Am. Chem. Soc.* **2018,** *140* (51), 18132-18139.
12. Xue, W.; Tan, X.; Oo, M. K. K.; Kulkarni, G.; Ilgen, M. A.; Fan, X., Rapid and sensitive detection of drugs of abuse in sweat by multiplexed capillary based immuno-biosensors. *Analyst* **2020**.
13. Huang, L. R.; Chiu, C. M.; Yeh, S. H.; Huang, W. H.; Hsueh, P. R.; Yang, W. Z.; Yang, J. Y.; Su, I. J.; Chang, S. C.; Chen, P. J., Evaluation of antibody responses against SARS coronaviral nucleocapsid or spike proteins by immunoblotting or ELISA. *J Med Virol.* **2004,** *73* (3), 338-346.
14. He, Q.; Du, Q.; Lau, S.; Manopo, I.; Lu, L.; Chan, S.-W.; Fenner, B. J.; Kwang, J., Characterization of monoclonal antibody against SARS coronavirus nucleocapsid antigen and development of an antigen capture ELISA. *J. Virol. Methods* **2005,** *127* (1), 46-53.

15. Tampoia, M.; Giavarina, D.; Di Giorgio, C.; Bizzaro, N., Diagnostic accuracy of enzyme-linked immunosorbent assays (ELISA) to detect anti-skin autoantibodies in autoimmune blistering skin diseases: a systematic review and meta-analysis. *Autoimmun. Rev.* **2012,** *12* (2), 121-126.
16. Weng, X.; Gaur, G.; Neethirajan, S., Rapid detection of food allergens by microfluidics ELISA-based optical sensor. *Biosensors* **2016,** *6* (2), 24.
17. Duddy, M. E.; Alter, A.; Bar-Or, A., Distinct profiles of human B cell effector cytokines: a role in immune regulation? *J. Immunol.* **2004,** *172* (6), 3422-3427.
18. Kim, S. B.; Koo, J.; Yoon, J.; Hourlier-Fargette, A.; Lee, B.; Chen, S.; Jo, S.; Choi, J.; Oh, Y. S.; Lee, G., Soft, skin-interfaced microfluidic systems with integrated enzymatic assays for measuring the concentration of ammonia and ethanol in sweat. *Lab Chip* **2020,** *20* (1), 84-92.
19. Saka, S. K.; Wang, Y.; Kishi, J. Y.; Zhu, A.; Zeng, Y.; Xie, W.; Kirli, K.; Yapp, C.; Cicconet, M.; Beliveau, B. J., Immuno-SABER enables highly multiplexed and amplified protein imaging in tissues. *Nat. Biotechnol.* **2019,** *37* (9), 1080-1090.
20. Poudineh, M.; Maikawa, C. L.; Ma, E. Y.; Pan, J.; Mamerow, D.; Han, Y.; w Baker, S.; Beirami, A.; Eisenstein, M.; Kim, S., Continuous detection of glucose and insulin in live animals. *bioRxiv* **2020**.
21. Cai, X.; Chen, J.; Hu, J.; Long, Q.; Deng, H.; Fan, K.; Liao, P.; Liu, B.; Wu, G.; Chen, Y., A Peptide-based Magnetic Chemiluminescence Enzyme Immunoassay for Serological Diagnosis of Corona Virus Disease 2019 (COVID-19). *medRxiv* **2020**.